Bifurcations in Impact Oscillators: Theoretical and Experimental Studies

Stephen Foale

Thesis submitted for the degree of
Doctor of Philosophy

Centre for Nonlinear Dynamics
University College London
June 1993

Acknowledgements

Firstly I would like to thank my parents for all of the support and encouragement they have given me over the years.

I would also like to thank all of the members of the Centre for Nonlinear Dynamics at University College for many useful discussions about my work.

Abstract

One of the most important features of nonlinear dynamical systems is that, as system parameters are varied, qualitative changes in the overall behaviour of the system can occur at a *bifurcation*. For smooth systems, the local bifurcations which occur under the change of one parameter are well understood. Non-smooth dynamical systems, which frequently arise due to the way certain physical processes are modelled, undergo bifurcations which have not been widely studied. We examine a particular type of bifurcation arising in a commonly occurring class of non-smooth dynamical system, combining theoretical and experimental results.

In this thesis we are concerned with the study of the important class of dynamical system we call *impact oscillators*, which undergo oscillations under the influence of some forcing, and additionally can undergo impacts at rigid stops. Such systems are of interest because a large number of physical and engineering systems display behaviour which can be classified as impacting, where it is important to use a dynamical analysis to identify and thus avoid the noise, wear or failure which could be caused by repeated impacts producing unacceptably large loads. Recent interest in such systems has concentrated on the unusual bifurcational behaviour which occurs when part of an orbit begins to undergo low velocity impacts. Using analytical methods to locate particular simple steady state solutions of an impact oscillator these *grazing bifurcations* are investigated. Comparisons are made between the behaviour of these special bifurcations, which arise because of the instantaneous reversal of velocity in the mathematical model of the impact process, and the standard bifurcations of smooth dynamical systems.

An experimental study of an electromagnetically forced metal beam impacting against a stop is used to show that the overall qualitative behaviour displayed by a simple theoretical model is also displayed in a physical impact oscillator. Finally the theoretical studies are related to a particular problem of offshore engineering and it is shown how a very simple model can be used to explain some unusual observed behaviour.

Contents

1. **Preliminaries**

2. **Numerical methods**

Page

3. Impact Oscillators

4. Bifurcations in impact oscillators

5. Impacting offshore systems

6. Experimental studies of an impact oscillator

List of figures

Page

Figure 5.1, page 129, is between pages 144 and 145.

1. Preliminaries

1.1 Introduction to Impact Oscillators

Physical applications which undergo impacts against some kind of stop to limit the motion of a system are very common and arise in many different areas of engineering. The very fact that the impact process exists and is very different from the "free" motions away from impact make such impacting systems nonlinear, and if there is an external driving function then these impacting systems form an important class of forced dynamical system. We shall call this class *impact oscillators*. We now give a brief survey of the literature which exists concerning systems in this general class : first, some of the theoretical studies, then some practical applications and finally some experimental studies.

1.1.1 Theoretical studies

Early work by Shaw and co-workers concentrated on one sided impact oscillators modelled by sinusoidally forced, second order ordinary differential equations with either a piecewise linear stiffness function or a linear stiffness function and a coefficient of restitution (COR) rule. For both of these cases some particular analytical solutions can be located for the model of an impact oscillator [Shaw & Holmes, 1983c]. The stability of these analytical solutions can also be found allowing loci of saddle-node and flip bifurcations to be located. The discontinuous nature of maps obtained from impact oscillators was noted in this work. A similar analysis was performed by Whiston [1979]. Further studies by the same authors [Shaw & Holmes, 1983a, 1983b] analysed the special case of a linear oscillator with a COR rule where the coefficient is small (zero or near zero). In the case of zero coefficient of restitution, the whole system can be reduced to a one dimensional map (on a circle) which is discontinuous and regions of stable orbits of low period are shown, and also transient nonperiodic motions. The same technique as used by Shaw & Holmes for obtaining analytical solutions of the COR rule impact oscillator was also used by Hindmarsh & Jefferies [1984]. Using both analytical calculations and numerical simulations, this work identified regions of stability for low period solutions and also identified apparently chaotic solutions. The discontinuities and discontinuities in gradient inherent in the system were identified as being of interest. Shaw [1985a, 1985b] again studied the simple COR rule model, this time with two stops, and showed local and global bifurcations.

Whiston [1987a] studied local bifurcations in an impact oscillator with COR rule and preload (i.e. the equilibrium position with no forcing is at a stop), again using the same kinds of analytical techniques as many previous authors described above, whereas Whiston [1987b] studied in some detail the global dynamics of the same system. Again, it was noted that the discontinuities in the dynamics could lead to "non-differentiable" bifurcations which merited further study. Shaw & Rand [1989] find analytical solutions for the system consisting of an inverted pendulum with a COR rule applied at two stops, and again find local and global bifurcations, and the same ideas are extended to a two degree of freedom COR impact oscillator [Shaw & Shaw, 1989]. The analysis for the single degree of freedom, two sided COR rule impact oscillator system is generalised by Natsiavas [1990] to general n-periodic steady state solutions with arbitrary numbers of impacts.

Nordmark [1991] developed further some of the observations made in the work discussed above that discontinuities and discontinuities in gradient exist in impact oscillators which use an instantaneous impact rule (such as the COR rule). Orbits which just "graze" a stop (i.e. start to impact with zero velocity) were shown in this paper to cause a loss of stability at a *grazing bifurcation*. These bifurcations due to low velocity impacts have been the subject of much interest from several authors in recent years. Chillingworth [1989] has studied the geometry of the sets in phase and parameter space which lead to orbits which graze the stop, and this work is continued by Whiston [1992] in which homoclinic bifurcations due to the non-differentiable nature of impact oscillators are studied in some depth. Nordmark [1992a & 1992b] investigates these grazing phenomena further. One interesting development by Nordmark is the approximation of the instantaneous impact rule by a continuous function (with nonlinear stiffness which rises rapidly after impact). Here, a chaotic attractor with a typical "fingered" shape for COR impact oscillators, is more and more closely approached as the stiffness at impact in the equivalent continuous model rises more steeply. Budd *et al* [1993] also investigate grazing bifurcations for a one sided COR impact oscillator as the position of the stop is varied.

1.1.2 Physical and Engineering Systems with Impacts

As well as the theoretical developments discussed above, many studies have highlighted the practical physical and engineering problems which can be studied as impact oscillators. Mechanical engineering provides many examples of systems with impacts such as rattling gears [Karagiannis & Pfeiffer, 1991, Kahraman and Singh, 1990, Pfeiffer & Kunert, 1990, Reithmeier, 1990], vibration absorbers [Sharif-Bakhtiar & Shaw, 1988], car suspensions [Stennson *et al* 1992] and impact print hammers [Tung & Shaw, 1988a, 1988b]. In these mechanical engineering examples of impact oscillators, the primary problems caused by the successive impacts are noise and wear. Another rich source of impact oscillator problems is the offshore engineering environment. Work by Thompson and co-workers on the problem of a ship moored to an articulated mooring tower, essentially an inverted pendulum with buoyancy, undergoing wave driven oscillations was extensively studied [Thompson, 1983, Thompson & Ghaffari, 1983, Thompson & Elvey, 1984, Thompson, Bokaian & Ghaffari, 1984]. A similar problem, that of a ship moored against a fender, was studied by Lean [1971], and more recently by Sterndorff *et al* [1992]. Other offshore impacting problems arise in the installation of a structure over a guiding "indexing" system, discussed in more detail in chapter 5. Indexing systems can comprise of bumper piles, which guide the structure into position [Nelson *et al*, 1983, Stahl *et al*, 1983] or pile/sleeve arrangements [Robinson & Ramzan, 1988]. The effect of earthquakes on various structures has motivated other studies of dynamical impact type problems, for example, the responses of a slender block which rocks under external excitation [Hogan, 1989, 1992a & 1992b, Tso & Wong, 1989]. Hogan uses similar ideas to those of Shaw and others to obtain analytical solutions for an idealized piecewise linear model of a slender rocking block, along with the stability of these solutions, and extends these ideas in order to obtain expressions for the invariant manifolds of unstable solutions in order to find heteroclinic bifurcations. The "pounding" (i.e. collision) of nearby buildings under earthquake excitation is another example [Jing & Young, 1990, 1991]. The electricity generating industry has also produced impact oscillator problems, such as the cross flow induced impacting of heat exchanger tubes [Paidoussis & Li, 1992].

1.1.3 Experimental impact oscillators

Several experimental studies of impact oscillators have been undertaken, designed to show different aspects of the response of these systems. Again, Shaw and co-workers have been active in this area [Moon & Shaw, 1983, Shaw, 1985, Moore & Shaw, 1990] using a vibrating beam in the first two papers and a normal and inverted pendulum for the third. In each case particular bifurcations were matched between theory and experiment. Bayly and Virgin [1992] also found good agreement between experimental results using a "rollercoaster" arrangement with a collision at a stop and a piecewise linear impact oscillator model. Nordmark & Stennson [1992] used a sinusoidally shaken mass/spring system with one sided impact and compared the results to a simple linear COR model with very good agreement. Even experimentally obtained apparently chaotic Poincaré maps were closely matched to numerical simulations of the theoretical model in this study.

1.1.4 Outline of the thesis

It is apparent from the brief review of the literature concerning impact oscillators given above that one of the interesting features of these systems is that they can undergo "unusual" bifurcations. These grazing bifurcations cannot be understood using the conventional theory of smooth bifurcations. The problem arises due to the idealised rule which is often used to model the impact process, namely the coefficient of restitution rule $v \mapsto -rv$ where v is the velocity at impact. The instantaneous nature of the reversal of velocity leads to discontinuities and discontinuities in gradient in mappings arising from the dynamical system.

This thesis is largely concerned with the study of these grazing bifurcations. Other work in similar subject areas has been taking place independently by Budd and co-workers [Budd *et al*, 1993], Nordmark [1991] and Whiston [1992]. The analytical solutions which are developed in chapter 3 for simple orbits of an impact (i.e. those orbits with low numbers of impacts) can be used to examine in detail grazing bifurcation events. Both stable and unstable paths of steady state solutions can be located analytically. We find that there can be two distinct types of "first grazing" bifurcation, and there is a simple criterion for distinguishing between them. These first grazing bifurcations in impact oscillators using the coefficient of restitution rule are compared to the conventional bifurcations undergone by an impact oscillator where the impact process is modelled with a continuous and differentiable function.

A particular problem of marine engineering which involves impacts in the installation of a jacket structure over pre-installed piles is examined in chapter 5 in the light of the ideas developed in earlier chapters concerning grazing bifurcations. It is found that these bifurcations play an important part in the overall behaviour of the simple model of the physical system. Experimental verification of grazing bifurcation events is obtained in chapter 6. The experimental apparatus consists of an electromagnetically forced steel beam with a one sided amplitude constraint imposed by a metal stop.

1.2 Smooth dynamical systems

1.2.1 The Poincaré Section

Continuous time dynamical systems commonly arise from models of physical systems, for example as the time evolution of a set of ordinary differential equations. The simplest kind of limit set for this class of dynamical system is a fixed point, i.e. if we start with initial conditions at a fixed point we will stay there for all time. In later chapters we concentrate on forced dynamical systems, in which the time variable is explicitly included in the right hand side of the set of differential equations which define the dynamical system. In this case, we always have an equation, "$\dot{t}=1$", which immediately excludes the possibility of a fixed point (since one of the variables is always increasing), and so other types of limit sets exist, for example a periodic orbit. This is a solution which repeats exactly after some time T, the period of the limit cycle. It is often convenient to reduce the continuous time problem to one of discrete time, and also to reduce the dimension of the problem by one, using the method of Poincaré sections.

Given a continuous time dynamical system $\dot{x}=f(x)$, $x \in \mathbf{R}^n$, we define a Poincaré section $\Sigma \in \mathbf{R}^n$ as a local $n-1$ dimensional surface which is everywhere transverse to the flow. Figure 1.1 shows such a surface in a three dimensional space. The heavy line in this figure represents a periodic orbit of the flow, which intersects the surface Σ at x^*. The other, thinner line represents a transient orbit which first intersects Σ at x_1 and then at x_2. It is clear that the device of a Poincaré section has given a mapping from Σ to Σ, P say. So we have that $P(x^*)=x^*$ and $P(x_1)=x_2$. We can see that any closed orbit of the flow arising from the original set of differential equations will be a fixed point of some degree of the map. It is also straightforward to show that there is a simple relationship between the characteristic exponents of the closed orbit and the eigenvalues of the fixed point of the map. The eigenvalues of the map are just the exponentials of the characteristic exponents.

We exclude here the zero characterstic exponent in the flow direction.

A frequently encountered class of continuous time dynamical system which can always be reduced to a discrete time system with a "natural" Poincaré section is the periodically forced oscillator. This is a set of differential equations of the form $\dot{x}=f(x,t)$, where $f(x,t)=f(x,t+T)$ for all x, and T is the period of the forcing. We can see that a Poincaré section defined by $\{(x,y,\theta) : \theta=t_0\}$ where $\theta=t \bmod T$ and $t_0\in[0,T]$ will always be transverse to the flow (since $\dot{t}=1$). The map which takes points on the section $\theta=t_0$ back on to this section is often called the stroboscopic Poincaré map since it is using a time periodic sampling of the state of the dynamical system. In later chapters we will always use this stroboscopic map in preference to other candidates. The reason for this is that it is guaranteed to be transverse to the flow everywhere. Other "natural" choices are often not everywhere transverse, and this can lead to some confusing results. For example, Kleckza *et al* [1992] analyse an oscillator with a piecewise linear stiffness function and choose a section along one of the "switching planes", i.e. at the displacement where one of the changes in stiffness occurs. They observe a "period 3 to period 4" bifurcation in the switching plane map. There is no corresponding bifurcation in the flow : the apparent bifurcation is due only to the "bad" section (not everywhere transverse to the flow).

1.2.2 Structural stability and co-dimension one bifurcations

Typically a dynamical system will have parameters which, when varied, can change the overall dynamical behaviour of that system. At certain values of these parameters, changes in the qualitative structure of the solutions can change, and these changes are called *bifurcations*. The definition of a bifurcation value (see for example Guckenheimer & Holmes [1990]) is a parameter value μ_0 at which the dynamical system is not structurally stable (this can apply both to maps and flows). A precise definition of structural stability can be found in Guckenheimer and Holmes section 1.7.4, but essentially a structurally stable system is one that retains its qualitative properties under small perturbations. Restricting this definition to smooth maps, we can see that a fixed point of a map will undergo a bifurcation when there is a direction just poised between contraction and expansion, i.e. when one of the eigenvalues of the map linearised around the fixed point is of unit modulus. An arbitrary perturbation to the map will then have two possible outcomes. Examples of this in one dimensional maps are shown in figures 1.2 and 1.3. The line $x_n=x_{n+1}$ (where $x_{n+1}\equiv f(x_n)$) is shown dotted in both cases along with three slightly different curves which represent the mapping from x_n to x_{n+1}, with the parameters $\mu<0$, $\mu=0$ and $\mu>0$. The middle line in these diagrams, with $\mu=0$ represents a bifurcating curve, i.e. one which has a fixed point at which the slope of the curve has modulus one.

In figure 1.2 the slope of the bifurcating curve at the fixed point B is +1. The other two curves represent perturbations of this bifurcating one, and it is seen that, depending on the particular type of perturbation there are two distinct qualitative structures. The lower curve has two more intersections with the line $x_n=x_{n+1}$ than the higher curve, i.e. the mapping represented by the higher curve has two more fixed points (the lower one stable, with slope less than the $x_n=x_{n+1}$ line, and the upper one unstable, with slope greater than this line) than the mapping represented by the lower curve.

In figure 1.3a the slope of the bifurcating curve at the fixed point is -1. Again, the other two curves represent perturbations of this bifurcating one and here it is seen that, although the number of intersections with the line $x_n=x_{n+1}$ is the same for all three curves. In fact there is only one intersection which is forced to be at the same point in each case. The fixed point in the higher curve ($\mu > 0$) is unstable (the slope of the curve at the fixed point is greater than one in modulus) and the fixed point in the lower curve ($\mu < 0$) is stable (the slope of the curve at the fixed point is less than one in modulus). Figure 1.3b shows the second iterate of the same map $f^2(x_n)$ against x_n, again for the three cases $\mu < 0$, $\mu = 0$ and $\mu > 0$. In this case we can see that there is only one (stable) fixed point for $\mu < 0$, but there are three fixed points of f^2 for $\mu > 0$, two stable and one unstable. These two bifurcations are the saddle node or fold bifurcation and flip bifurcation which we will go on to discuss in a following section.

In later chapters we will be concentrating on "unusual" bifurcations of maps derived by taking Poincaré sections through the vector field of a sinusoidally forced impact oscillator. The essential feature which is the cause of the unusual bifurcational behaviour of these maps is that they are non-smooth. Not only are there lines of discontinuity of gradient, but along these lines there is a square root type singularity in the derivative of the map (see section 3.6). From the definition given above, a bifurcation can occur at parameter values at which a fixed point lies on a line of discontinuity of gradient since the map can be structurally unstable along this line.

Before discussing the unusual bifurcations which occur in continuous but non-differentiable mappings, we briefly discuss the generic bifurcations a one dimensional mapping under the change of one parameter. We consider the smooth, one parameter family of diffeomorphisms $f(\mu,x)$ $(\mu,x \in \mathbb{R})$ for which $f(0,x)=0$ has a non-hyperbolic fixed point at the origin, i.e. $f(0,0)=0$, $|Dxf(0,0)|=1$ (a linear mapping is said to be hyperbolic if it has no eigenvalues with modulus equal to unity). Taylor expanding about $(\mu,x)=(0,0)$

$$
\begin{aligned}
f(\mu,x) &= D_x f(0,0)x + D_\mu f(0,0)\mu + \\
&\frac{1}{2}[D_{xx}f(0,0)x^2 + 2D_{\mu x}f(0,0)\mu x + D_{\mu\mu}f(0,0)\mu^2] + O([\mu,x]^3)
\end{aligned}
\tag{1.1}
$$

This can be written as a series expansion in x

$$
\begin{aligned}
f(\mu,x) &= a_0 + a_1 x + a_2 x^2 + a_3 x^3 + \dots \\
&+ \mu(b_0 + b_1 x + b_2 x^2 + \dots) \\
&+ \mu^2(c_0 + c_1 x + \dots) + \dots
\end{aligned}
\tag{1.2}
$$

where

$$
\begin{aligned}
&a_0 = f(0,0) \ , \ a_1 = D_x f(0,0) \ , \ a_2 = \frac{1}{2}D_{xx}f(0,0) \ , \ \dots \\
&b_0 = D_\mu f(0,0) \ , \ b_1 = D_{\mu x} f(0,0) \\
&c_0 = \frac{1}{2}D_{\mu\mu}f(0,0) \ , \ \dots
\end{aligned}
\tag{1.3}
$$

In order to find fixed points of $f(\mu,x)$ we can look for $g(\mu,x)=f(\mu,x)-x=0$. There are two ways in which the mapping f can satisfy the condition that it be non-hyperbolic at the origin, either by having an eigenvalue of +1 or -1. A higher dimensional map can also lose hyperbolicity with a pair of complex conjugate eigenvalues with modulus one, but we will not consider this case here.

1.2.3 The Saddle Node Bifurcation

Taking the first case, in which the eigenvalue $D_x f(0,0)=+1$, we have the case shown in figure 1.1 of a fold or saddle node bifurcation. The condition for a fixed point is $g(\mu,x)=0$, which gives

$$
\begin{aligned}
g(\mu,x) &= a_0 + \mu b_0 + \mu^2 c_0 + \dots + \\
&(a_1 + \mu b_1 + \dots - 1)x + (a_2 + \mu b_2 + \dots)x^2 + \dots = 0
\end{aligned}
\tag{1.4}
$$

Since we have that $f(0,0)=0$ and assuming that $D_\mu f(0,0)\neq 0$ then the Implicit Function

Theorem implies the existence of a function $\mu(x)$ such that

$$g(\mu(x),x) = 0 \tag{1.5}$$

over an interval $x \in (-\epsilon,\epsilon)$, $\epsilon > 0$. Differentiating 1.5 with respect to x gives

$$D_x\mu(0) = \frac{D_x g(0,0)}{D_\mu g(0,0)} = 0 \tag{1.6}$$

and differentiating with respect to x a second time gives

$$D_{xx}\mu(0) = -\frac{D_{xx}g(0,0)}{D_\mu g(0,0)} = -\frac{D_{xx}f(0,0)}{D_\mu f(0,0)} \tag{1.7}$$

Further assuming that

$$D_\mu f(0,0) > 0 \quad , \quad D_{xx}f(0,0) > 0 \tag{1.8}$$

then equation 1.6 gives that the function $\mu(x)$ has a turning point at $x=0$, and 1.7 with 1.8 gives the further information that this turning point is a maximum. The function $f(\mu,x)$ therefore has two fixed points for $\mu<0$, one with $x>0$ and one with $x<0$. Taylor expanding again

$$\begin{aligned} D_x f(x,\mu) &= D_x f(0,0) + xD_{xx}f(0,0) + \mu D_{\mu x}f(0,0) + \dots \\ &= 1 + xD_{xx}f(0,0) + \dots \end{aligned} \tag{1.9}$$

using the fact that $\mu = O(x^2)$ for $-\epsilon < x < \epsilon$. The fixed points with $x>0$ are therefore unstable and those with $x<0$ are stable, using 1.8, as illustrated in figure 1.1.

1.2.4 The Flip Bifurcation

The other way in which the map f can become non-hyperbolic is for the eigenvalue of the fixed point at the origin $D_x f(0,0)=-1$. In this case we simplify the analysis of the bifurcation by assuming that a further transformation has been performed so that the fixed point is always at zero, i.e. $f(\mu,0)=0$ for all μ. So we again have the Taylor series expansion equation 1.2 where the terms $a_0=b_0=c_0=\dots=0$. We consider the case where the change of stability of the period one path $f(\mu,0)=0$ at $\mu=0$ is from stable with $\mu<0$ to unstable with $\mu>0$. This means that $b_1<0$. Since, with $\mu>0$, the period one path is unstable, we look for further solutions in the mapping $f^2(\mu,x)$. The leading terms of the Taylor expansion for f^2 are

$$f^2(\mu,x) = x(1 - 2\mu b_1) - 2(a_2 + a_3)x^3 + \dots \qquad 1.10$$

and so the condition for a period two fixed point is that the function $h(\mu,x)=f^2(\mu,x)-x=0$. That is,

$$x[-2\mu b_1 - 2(a_2^2 + a_3)x^2] = 0 \qquad 1.11$$

So we see that we recover the path $x=0$ (which we already know to be an unstable period one fixed point of f, and is therefore also a fixed point of f^2), and another two solutions

$$x^2 = -\frac{\mu b_1}{a_2^2 + a_3} \qquad 1.12$$

Since we have already assumed that $b_1<0$, the sign of $a_2^2+a_3$ controls the type of bifurcation at $\mu=0$. If $a_2^2+a_3>0$ then there are two fixed points of f^2 for $\mu>0$, and if $a_2^2+a_3<0$ there are two fixed points of f^2 for $\mu<0$. These are the *supercritical* and *subcritical* flip bifurcations respectively. Examining the stability of the period two solutions arising from these two types of flip bifurcation we see that the first differential with respect to x of the Taylor series expansion of f^2 is given by $D_x f^2(\mu,x)=1+4\mu b_1$. The supercritical bifurcation gives rise to a period two solution for $\mu>0$, and so this solution is stable. The subcritical bifurcation gives rise to a period two solution for $\mu<0$, and so this is unstable.

1.3.1 Non-smooth dynamical systems

Although some of the "classical" chaotic mappings which have been studied are non-differentiable, for example the tent map and the Lozi map, the bifurcations which occur in these maps have not been widely studied. Nusse & Yorke [1992] did investigate some of the types of bifurcation which can arise in piecewise smooth maps, and called them *border collision* bifurcations. In order to demonstrate the kinds of unusual bifurcational behaviour which can occur when a mapping is continuous but not differentiable some examples from Nusse & Yorke are given below. The general form of the mapping studied is

$$\left.\begin{aligned} x_{n+1} &= ax_n + by_n + \mu \\ y_{n+1} &= cx_n \end{aligned}\right\} x_n<0$$
$$\left.\begin{aligned} x_{n+1} &= dx_n + by_n + \mu \\ y_{n+1} &= ex_n \end{aligned}\right\} x_n\geq 0 \qquad 1.13$$

Nusse and Yorke derive this form from any general piecewise smooth nonlinear mapping. The map is smooth in each of the half planes $x_n<0$, $x_n\geq 0$ and is continuous along the line $x_n=0$. The types of bifurcation which can occur in this class of dynamical system are very unusual when compared to the bifurcations of smooth maps of the plane onto itself (such as those discussed above). For example, if $a=-1.4$, $b=1$, $c=-0.1$, $d=-3$, $e=-4$ then a numerical investigation shows that there is a bifurcation when $\mu=0$ in which a stable periodic orbit of period 2 disappears and a stable period 3 orbit appears (figure 1.4). Using simple linear algebra it is easy to find the steady state solutions of this system. A systematic procedure can be used to test any possible steady state solutions of the mapping. We start off with the possible period 1 fixed points. These are solutions of the equations

$$A\begin{bmatrix} x_1^* \\ y_1^* \end{bmatrix} + \mu\begin{pmatrix} 1 \\ 0 \end{pmatrix} = \begin{bmatrix} x_1^* \\ y_1^* \end{bmatrix}, \quad A = \begin{bmatrix} a & b \\ c & 0 \end{bmatrix}$$
$$B\begin{bmatrix} x_2^* \\ y_2^* \end{bmatrix} + \mu\begin{pmatrix} 1 \\ 0 \end{pmatrix} = \begin{bmatrix} x_2^* \\ y_2^* \end{bmatrix}, \quad B = \begin{bmatrix} d & b \\ e & 0 \end{bmatrix} \qquad 1.14$$

Solving these equations we get that $(x_1^*,y_1^*)=(2\mu/5,-\mu/25)$, $(x_2^*,y_2^*)=(\mu/8,-\mu/2)$. Since, for the solutions to be valid, x_1^* must be less than zero and x_2^* must be greater than zero then the solution (x_1^*,y_1^*) is a period one solution only for $\mu<0$ and the solution (x_2^*,y_2^*) is a period one solution only for $\mu>0$. The eigenvalues of the matrices A and B give the stability characteristics of these period one solutions. The matrix A has eigenvalues $(-7\pm\sqrt{39})/10$ and so is a saddle type solution and the matrix B has eigenvalues $(-3\pm i\sqrt{7})/2$ and so is a repellor. A similar process can be used to find a period two solution by solving

$$B\left[A\begin{bmatrix}x_3^*\\ y_3^*\end{bmatrix}+\mu\begin{pmatrix}1\\0\end{pmatrix}\right]+\mu\begin{pmatrix}1\\0\end{pmatrix}=\begin{bmatrix}x_3^*\\ y_3^*\end{bmatrix} \qquad 1.15$$

to give $(x_3^*,y_3^*)=(76\mu/65,3\mu/130)$, and by noting also that $B(x_3^*,y_3^*)+\mu=(-3\mu/13,-2\mu/13)$ we see that this period two solution is only valid for $\mu<0$. The stability characteristics of this period two fixed point can be found by computing the eigenvalues of the matrix AB. In this case the eigenvalues are $(1\pm i\surd159)/20$, both less than one in modulus, and so the period two fixed point is stable (figure 1.4). There are two possibilities for period three fixed points which can be found by solving

$$\begin{gathered}B\left[B\left[A\begin{bmatrix}x_4^*\\ y_4^*\end{bmatrix}+\mu\begin{pmatrix}1\\0\end{pmatrix}\right]+\mu\begin{pmatrix}1\\0\end{pmatrix}\right]+\mu\begin{pmatrix}1\\0\end{pmatrix}=\begin{bmatrix}x_4^*\\ y_4^*\end{bmatrix}\\ A\left[A\left[B\begin{bmatrix}x_5^*\\ y_5^*\end{bmatrix}+\mu\begin{pmatrix}1\\0\end{pmatrix}\right]+\mu\begin{pmatrix}1\\0\end{pmatrix}\right]+\mu\begin{pmatrix}1\\0\end{pmatrix}=\begin{bmatrix}x_5^*\\ y_5^*\end{bmatrix}\end{gathered} \qquad 1.16$$

The solutions to these two equations are $(x_4^*,y_4^*)=(133\mu/88,\mu/88)$ and $(x_5^*,y_5^*)=(-70\mu/27,-124\mu/27)$. Full investigation shows that both are true solutions as long as $\mu>0$. The eigenvalues of the matrix AAB, which give the stability characteristics of the period three fixed point (x_4^*,y_4^*) are $(2\pm i\surd21)/25$, i.e. it is a stable fixed point since both eigenvalues are less than one in modulus. The eigenvalues of BBA, which give the stability characteristics of the other period three fixed point (x_5^*,y_5^*) are $(53\pm3\surd241)/20$. In this case, one eigenvalue is greater and one less than one in modulus, so the fixed point is a saddle. We now have a fairly comprehensive picture of what is going on in the apparent "period two to period three" bifurcation. When the parameter $\mu<0$ there are two fixed points, one stable period two and one period one saddle. At the critical, bifurcation value $\mu=0$ both of these solutions disappear, and three new solutions valid for $\mu>0$ are created. Two of these are period three solutions, one stable and one saddle type, and there is also a period one repellor. Nusse and Yorke in their paper did not find the unstable periodic solutions as well as the stable ones. We have given here a complete picture including all periodic orbits up to period three, and make the point that if we have a map which is continuous but not differentiable then we are no longer limited to the familiar bifurcations of smooth maps. The next example shows a bifurcation from a stable period one solution to an apparently chaotic solution as the fixed point crosses the discontinuity in gradient.

Consider again equation 1.13, this time with $a=1/2$, $b=1/2$, $c=1/2$, $d=-3$, $e=1/4$. In this case, numerical investigation shows that for $\mu<0$ there is a stable period one fixed point of the map. As μ increases through 0 a chaotic solution is created which grows out from the bifurcation point with no period doubling sequence of bifurcations, see figure 1.4. Again, we can use the systematic procedure described above to look for periodic solutions of the piecewise linear map. One period one solution is given by $(x,y)=(4\mu,2\mu)$, valid when $\mu<0$. The stability of this fixed point is given by the eigenvalues of A, i.e. $(1\pm\sqrt{5})/4$, so the fixed point is stable. Another period one fixed point is given by $(x,y)=(8/31,2/31)$, valid when $\mu>0$. The stability of this fixed point is given by the eigenvalues of B, i.e. $(-6\pm\sqrt{38})/4$, so the fixed point is of saddle type, with one stable and one unstable direction. If we look for further periodic fixed points, we find one of order two, none of order three, and one of order four. Both of these are valid only for $\mu>0$ and are of saddle type, and both only visit the left hand side of the plane once. The positions of these fixed points in the left hand plane are $(-68\mu/69, 10\mu/69)$, with eigenvalues $(-9\pm\sqrt{73})/16$, for the period two and $(-14892\mu/7819, 1894\mu/7819)$, with eigenvalues $(-669\pm\sqrt{447553})/128$, for the period four fixed point. Of course there will be many more, higher periodic orbits, which could be found in the same systematic way.

If we change the linear map for the right hand half plane in the example above such that $d=-1$, then the period one fixed point for $\mu<0$ is clearly identical. For $\mu>0$, there is still a period one saddle, $(x,y)=(8\mu/15,2\mu/15)$ with eigenvalues $(-2\pm\sqrt{6})/4$, but there is a stable period two orbit valid for $\mu>0$ (see figure 1.6). This orbit visits both sides once (as it must). Its position in the left half plane is $(x,y)=(-4\mu/37,10\mu/37)$ and in the right hand half plane $(x,y)=(40\mu/37,-2\mu/37)$. The eigenvalues of this period two fixed point are $(-1\pm i\sqrt{7})/16$, both less than one in modulus, so this is a stable orbit. So we have what appears to be a similar event to the supercritical flip bifurcation described above. A stable period one fixed point disappears at a critical parameter with the formation of a saddle type period one fixed point and a stable period two fixed point growing out of the bifurcation point. The characteristic shape of the stable period two orbit growing out from a supercritical flip bifurcation (the shape is a quadratic with respect to the parameter) is clearly not replicated in this piecewise linear example though. The only possibility here is that the period two orbit grows out at a constant angle, dependent on the precise linear mappings in the left and right hand half planes. All of these examples serve to show that we should not be too surprised in the later work on bifurcations in impact oscillators when bifurcations occur in continuous, non-differentiable maps, which cannot be classified using bifurcation theory for smooth maps. The bifurcations which occur in this special class of map have not been very deeply investigated. Nusse and Yorke did demonstrate a whole variety of the kinds of bifurcations which can occur, but they did not present anything like the simple, systematic procedure for finding orbits of a particular period described above.

1.3.2 Piecewise linear maps with a large direction of expansion

In this section we will look at a particular case of a border collision bifurcation in which the linear map in the right half plane has a large direction of expansion. This will be seen to be of relevance later on when we look at grazing bifurcations in impact oscillators, where there is a square root singularity in gradient.

Period one solutions of the piecewise linear mapping, equation 1.13, are found by solving equation 1.14, where A is the linear map in the left hand side of the plane ($x_n < 0$) and B is the linear map in the right hand side of the plane ($x_n > 0$). Assume that the mappings in both the right and left hand sides of the plane are orientation preserving and dissipative, i.e. the determinants of A and B are between zero and one. Further assume that A is such that both eigenvalues are less than one in modulus and the resulting stable, period one fixed point exists for $\mu < 0$. If we put $d = 1/\epsilon$, where $|\epsilon| \ll 1$, and $\det(B) = \beta$ then we have that $be = -\beta$, and the eigenvalues of B are $1/\epsilon + O(\epsilon^2)$, $\beta\epsilon + O(\epsilon^3)$. Solving equation 1.14 for x_2^* and y_2^* we obtain $x_2^* = -\mu/\epsilon + O(\epsilon)$, $y_2^* = ex_2^*$. This period one fixed point can only exist if $x_1^* > 0$. Therefore, if $\epsilon > 0$ we must have that $\mu < 0$ and if $\epsilon < 0$ then $\mu > 0$. In other words, if $\epsilon > 0$ then an orientation preserving period one saddle exists for $\mu < 0$ along with the stable period one fixed point which we assume to exist from the outset. Both stable and unstable fixed period one fixed points disappear at $\mu=0$, $(x,y)=(0,0)$. Otherwise, if $\epsilon<0$ then an orientation reversing (flip) period one saddle exists for $\mu>0$. In this case, the stable fixed point which we have assumed to exist for $\mu<0$ disappears at $\mu=0$, $(x,y)=(0,0)$ and a saddle is "created" at this point.

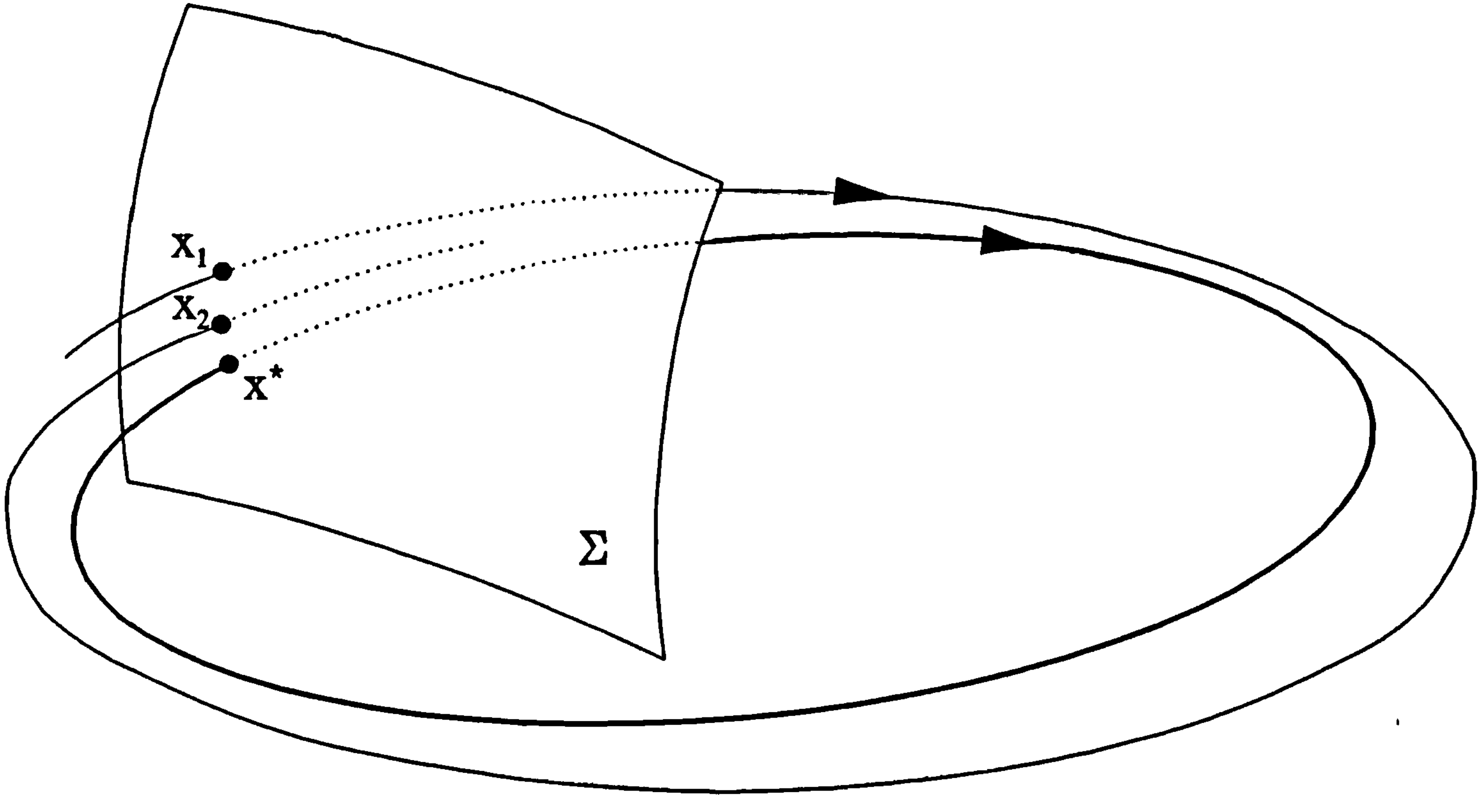

Figure 1.1 The Poincaré map : Σ is a local surface of section. The thick line represents a limit cycle, with x^* being the corresponding fixed point of the Poincaré map. The thin line represents a transient orbit, so x_2 is the image of x_1 under the Poincaré map.

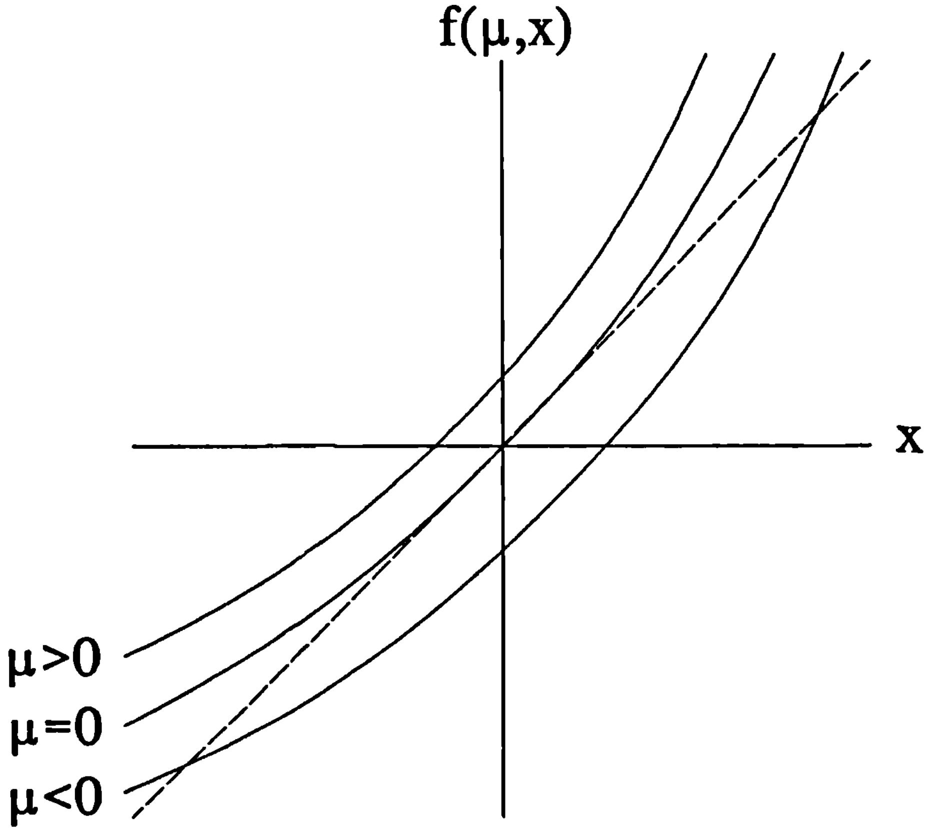

Figure 1.2 The saddle-node bifurcation. Three maps near to the bifurcation at $\mu=0$ are shown : $\mu<0$ for which there are two solutions (one stable, one unstable), $\mu=0$ for which there iss only one solution (neutrally stable) and $\mu>0$ for which there are no nearby solutions.

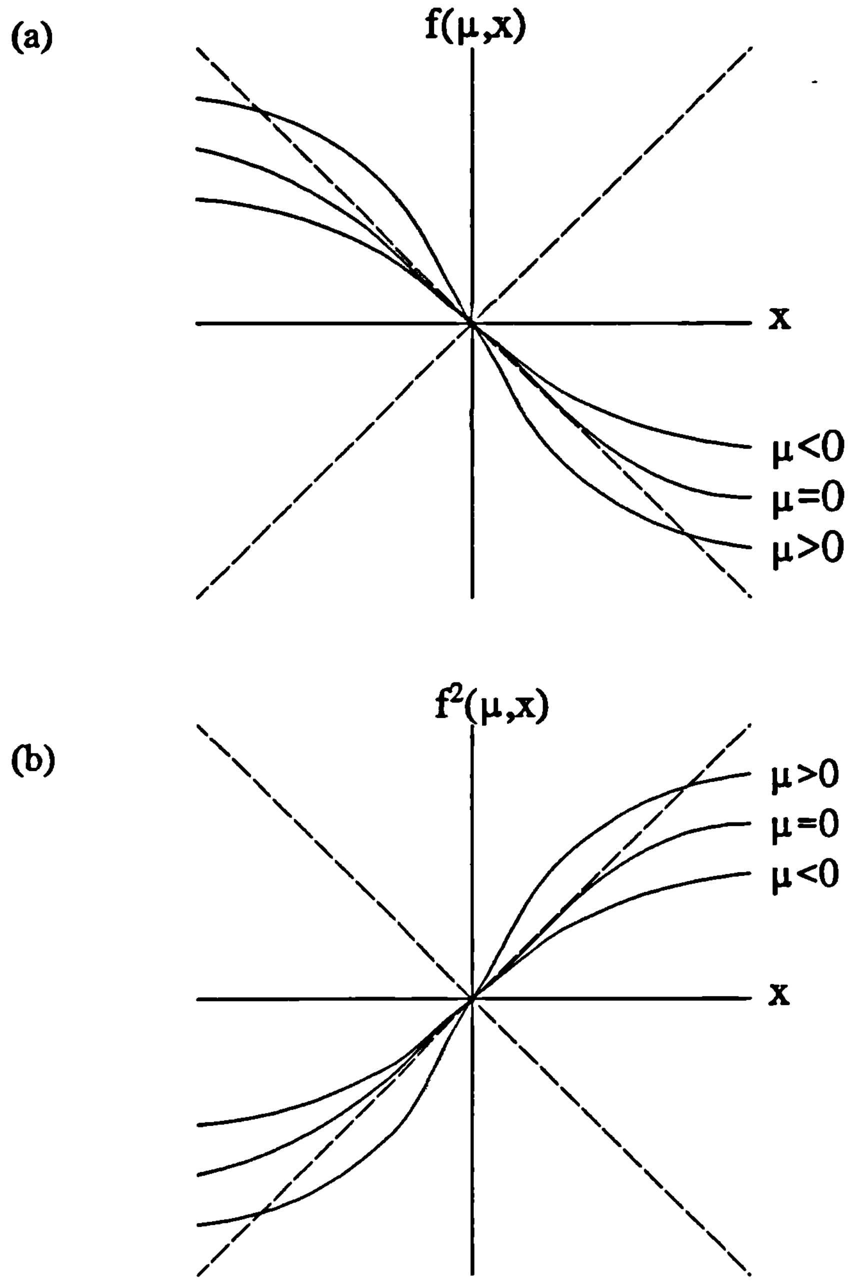

Figure 1.3 The flip bifurcation. The first and second iterates of three maps are shown in figures (a) and (b) respectively. In each case there is a fixed point of f at $x=0$, stable for $\mu<0$, neutrally stable for $\mu=0$ and unstable for $\mu>0$.

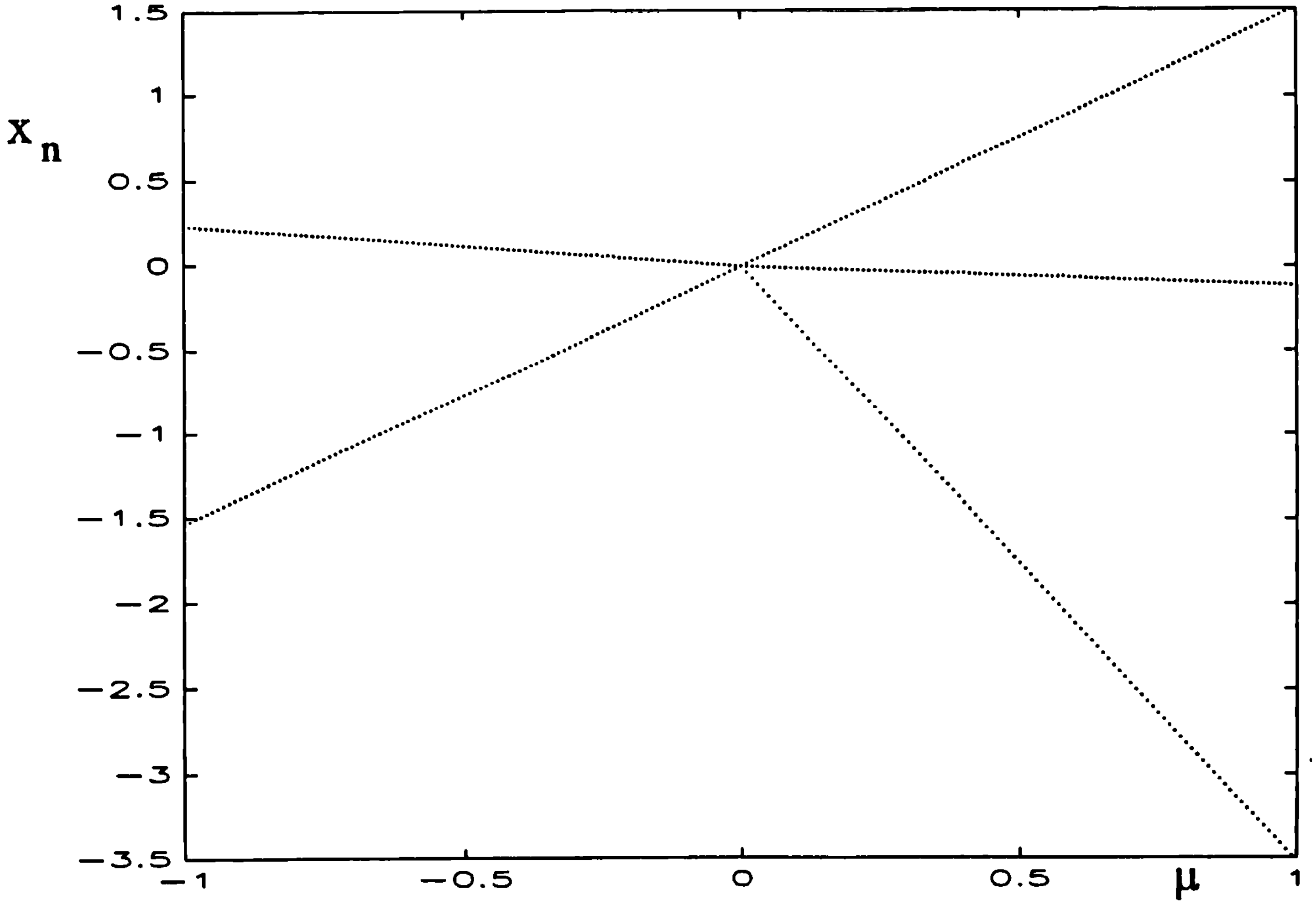

Figure 1.4 Period 2 to period 3 bifurcation for equation 1.13. a=-1.4, b=1, c=-0.1, d=-3, e=4.

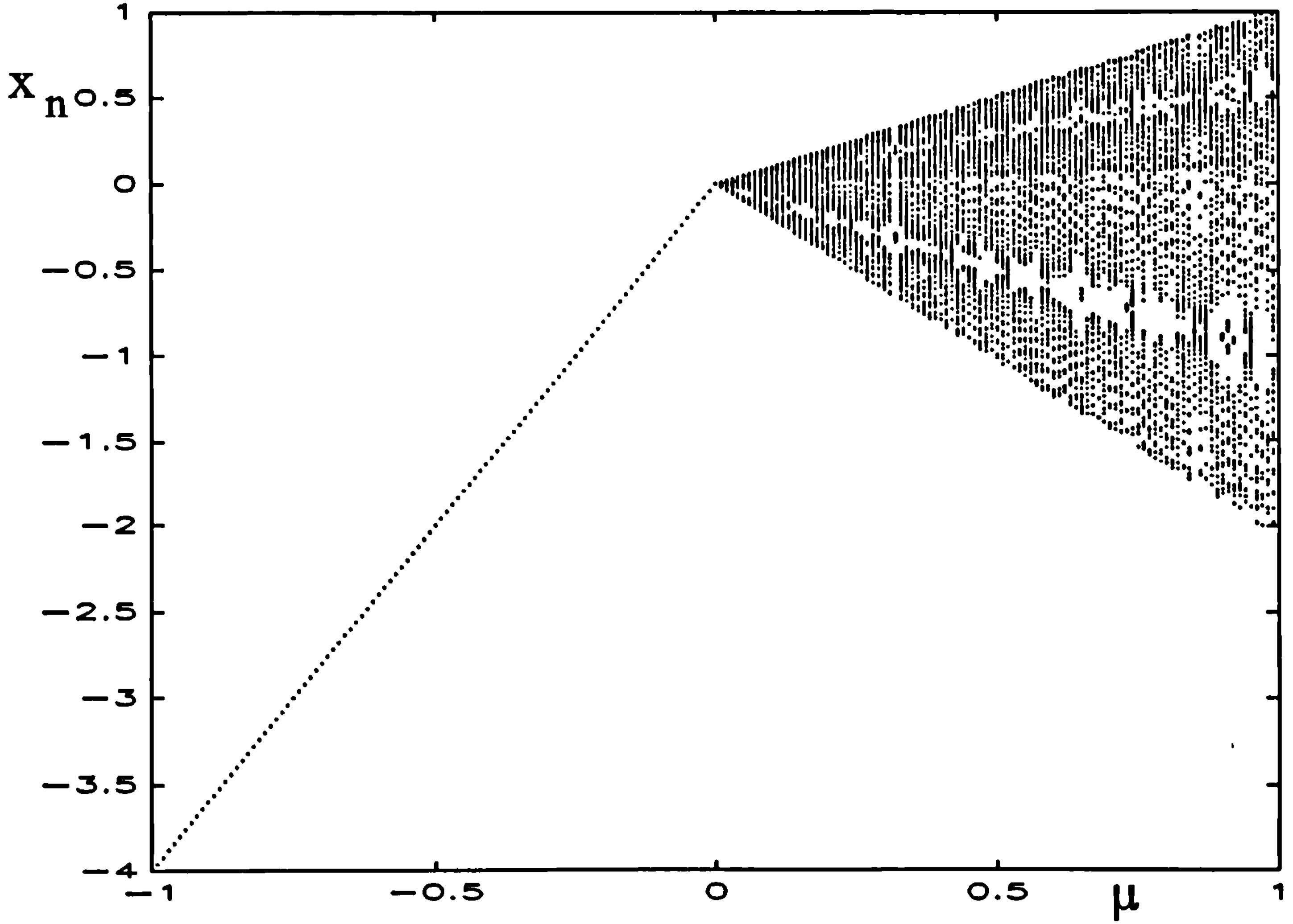

Figure 1.5 Bifurcation from period one to chaos for equation 1.13, a=1/2, b=1/2, c=1/2, d=-3, e=1/4.

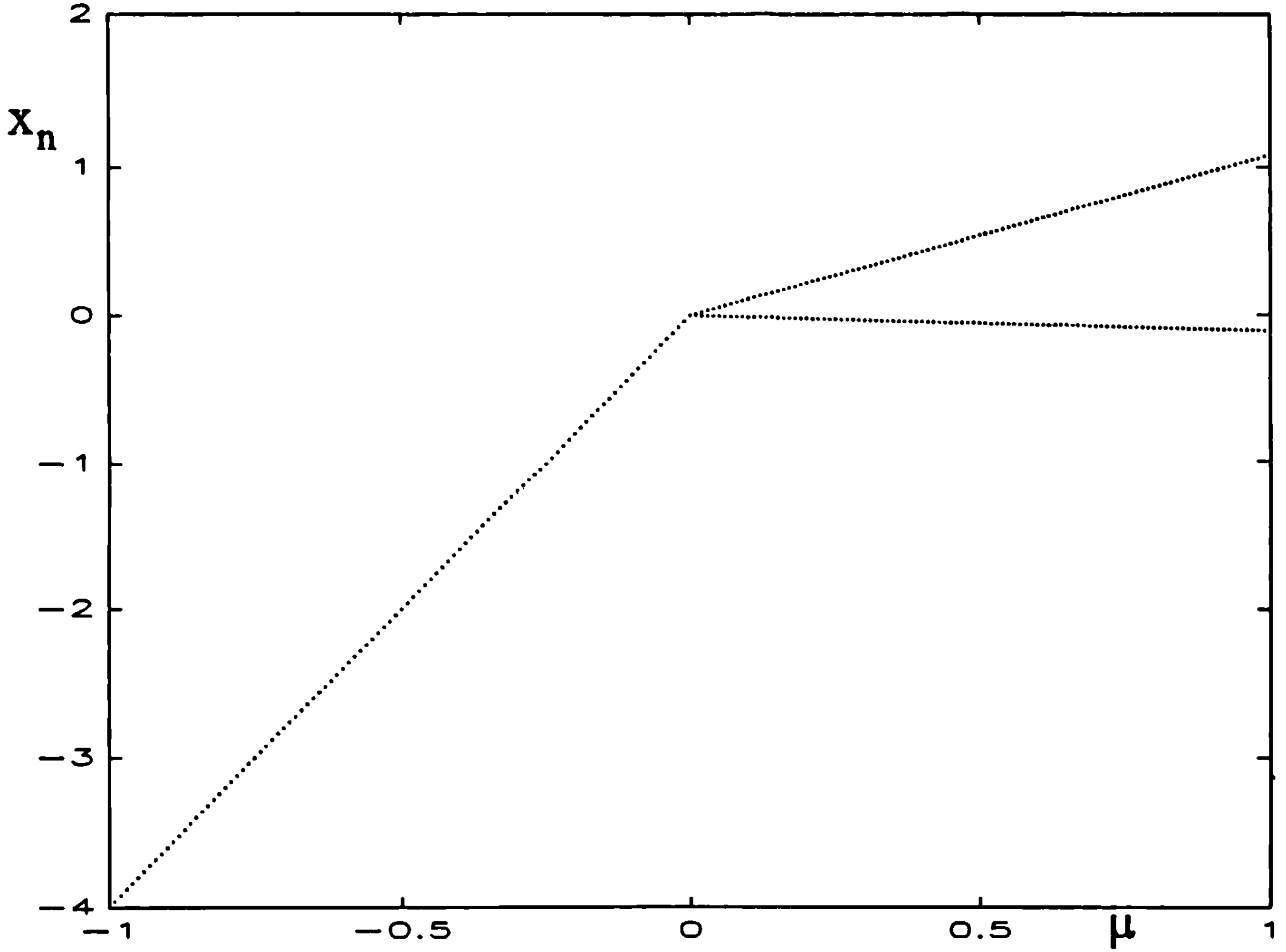

Figure 1.6 Period one to period two bifurcation for equation 1.13, a=1/2, b=1/2, c-1/2, d=-1, e=1/4.

2. Numerical Methods

2.1 Path following methods

One of the most common numerical procedures which is used in the analysis of nonlinear dynamical systems is the location and continuation of an asymptotic solution of a system as a parameter varies. Some of the numerical examples in later chapters use these techniques, generally known as continuation methods or path following methods. The general problem can be stated as solving

$$\begin{aligned} f(x;\mu) &= 0 \ , f:\mathbb{R}^{n+m}\rightarrow\mathbb{R}^{n} \ , \ x\in\mathbb{R}^{n}, \mu\in\mathbb{R}^{m} \\ c(x;\mu) &= 0 \ , \ c:\mathbb{R}^{n+m}\rightarrow\mathbb{R}^{k} \end{aligned} \qquad 2.1$$

where x is some set of state variables, μ is a set of parameters and $c(x;\mu)$ is an optional extra set of constraint equations (which could be used for example to find the location of a bifurcation), and both f and c are smooth functions (i.e. differentiable as many times as we will need in the following). If there are no constraints and no parameters, i.e. $m=0$, then the problem is just one of conventional root finding. The Newton method for determining roots can be derived by a Taylor expansion of the function and its derivative about a root, x^*

$$\begin{aligned} f(x^*+\delta x) &= f(x^*) + D_x f(x^*)\delta x + O(\delta x^2) \\ D_x f(x^*+\delta x) &= D_x f(x^*) + O(\delta x) \end{aligned} \qquad 2.2$$

Given a guess $x_i=x^*+\delta x$ then the next guess x_{i+1} is given by correcting x_i by δx where δx is given by solving the set of linear equations

$$f(x_i) = f(x^*) + D_x f(x^*)\delta x + O(\delta x^2) = D_x f(x_i)\delta x + \ldots \qquad 2.3$$

The n-dimensional Newton root finding algorithm is then given by the iterative procedure

$$x_{i+1} = x_i - \delta x \qquad 2.4$$

For a unique solution to the linear set of equations given by 2.3 the matrix of first derivatives at x_i must be of full rank. If this matrix is rank deficient by one then the correction δx is not unique. In the linearized system there is a line of solutions along the direction of the eigenvector corresponding to the zero eigenvalue.

Having discussed the familiar Newton method we now go on to extend it to not only find solutions of $f(x;\mu)=0$ (possibly with further constraints $c(x;\mu)=0$), but also to follow solutions as system parameters are varied. The standard Newton method locates zero dimensional (isolated point) solutions of $f(x)=0$ as long as the matrix of first derivatives is of full rank (and the initial guess is close enough to a root). If we form a new function g

$$g(v) = \begin{pmatrix} f(v) \\ c(v) \end{pmatrix} \quad ,g:\mathbb{R}^{n+m}\rightarrow\mathbb{R}^{n+k}, \;\; v=\begin{pmatrix} x \\ \mu \end{pmatrix} \qquad 2.5$$

then the matrix of first differentials of g at a point v^* where $g(v^*)=0$ generically has rank $n+k$ if $m \geq k$ (i.e. maximum rank). If $m-k=0$ the problem is just the one of root finding discussed above, but if $m-k=1$ then the implicit function theorem gives us that there exists an open interval I around zero such that for $\alpha \in I$ there is a function $\lambda(\alpha):\mathbb{R}\rightarrow\mathbb{R}^{n+m}$ such that $\lambda(0)=v^*$, $g(\lambda(\alpha))=0$, $\lambda'(\alpha)\neq 0$. Differentiating $g(\lambda(\alpha))=0$ gives $g'(\lambda(\alpha))\lambda'(\alpha)=0$, so the tangent to the curve λ spans the one dimensional kernel of g. Figure 2.1 illustrates a simple case where $g:\mathbb{R}^2\rightarrow\mathbb{R}$, γ is an arbitrary line passing through v^* and both $\lambda=g^{-1}(0)$ and γ are parameterised by α in such a way that $\lambda(0)=\gamma(0)=v^*$. This line λ is precisely the path which we want to find with a path following algorithm. The use we will have for these techniques is to locate the solution of a set of equations and then to follow it as a single parameter varies, or to follow a bifurcation as two parameters vary.

Given a function g as defined in equation 2.5 with $m-k=1$, and a root of g, v^*, then the aim of a path following algorithm is to continue this solution, i.e. find another nearby point along the one dimensional path of solutions for $g(v)=0$. First, a step in a direction tangent to the path at a known root v^* (or some approximation to that tangent) gives an initial guess for the next point on the path of solutions $g(v)=0$. There are several ways in which, given a guess for a new point on the solution path we can develop an iterative procedure based on Newton's method to locate a nearby solution, see figure 2.2. Perhaps the simplest is to simply "ignore" one of the directions altogether, i.e. choose an $n+k$ dimensional set of basis vectors along coordinate directions, and use a standard Newton root finding algorithm. In general, nearby there will be a unique isolated point solution to $g(v)=0$ in this $n+k$ dimensional space, see figure 2.2a. A problem arises with this method if the same coordinate direction is always ignored. If the solution curve has a turning point in this direction then at some point a step will take the hypersurface past the turning point and there will be no roots in the $n+k$ dimensional space for the Newton method to find. This problem can be overcome by varying the direction to ignore, for example, choose the ignored direction to be the one which was changing most at the previous step.

A similar idea is again to restrict the Newton algorithm to an $n+k$ dimensional space, but this time to use a set of basis vectors which span the space which is perpendicular to the direction tangent to the path at the last found point, see figure 2.2b. In this case, for small enough step sizes, there will in general be a unique root of $g(v)$ nearby.

Both of the above approaches are based on a similar idea : the overdetermined problem is reduced to conventional Newton Raphson (with as many equations as unknowns) by restricting the Newton search to a co-dimension one subspace. A different approach which can be used is to solve the overdetermined set of equations at each step to give a line of (approximate) roots and then to make some necessarily arbitrary choice of a point on this line as the next guess. The derivation of the conventional Newton method given above still holds even if there are more unknowns than equations, e.g. if $m\text{-}k=1$. In exactly the same way we can write

$$v_{i+1} = v_i - \delta v \qquad 2.6$$

where

$$g(v_i) = D_v g(v_i)\,\delta v + \dots \qquad 2.7$$

The solution of this set of linear equations is easily obtained using the singular value decomposition technique (SVD) [Golub & Van Loan 1989, Press et al 1988], which decomposes any matrix A into U,S,V where U,V are orthonormal matrices and S is diagonal such that $A=USV^T$. The positive real values s_i on the diagonal of S are called the singular values. SVD explicitly constructs an orthonormal basis for the range and nullspace of A. The columns of U which are associated with non-zero singular values form a basis for the range of A. The columns of V which are associated with zero singular values form a basis for the null space of A. We can use these ideas to solve the overdetermined set of equations, 2.8. If we pad the matrix of first differentials $D_v g(v)$ with a row of zeros to make it square and pad the corresponding row of the right hand side of the equation also with zeros then we have a square matrix (with no more or less information than before), i.e. as many equations as unknowns. The trivial equation which has been added will inevitably lead to a zero (or in practice very close to zero) singular value. We want to single out a solution from the one dimensional set of general solutions given by a particular solution vector plus any vector in the (one dimensional) null space. The "best" solution is the one of shortest length, i.e. the correction vector we want to choose is the one which drops a perpendicular line onto the approximation to the path (see figure 2.2c). This is achieved using the usual "trick" for inverting singular matrices with SVD : we replace $1/s_i$ by zero if $s_i=0$. Then the solution is given by

$$\delta v = V \left[diag \left[\frac{1}{s_i} \right] \right] \left[U^T \left[\begin{matrix} g(v_n) \\ 0 \end{matrix} \right] \right] \tag{2.8}$$

where the matrix $D_v g(v)$, padded with a row of zeros in the $(n+1)$th row has been decomposed into USV^T using SVD. To show that the solution given by equation 2.8 has the shortest length $|\delta v|$, we consider the vector $\delta v+z$, where z is in the nullspace of the padded matrix of first differentials. Then

$$\begin{aligned} |\delta v + z| &= \left| VS^{-1} U^T \begin{pmatrix} g(v_n) \\ 0 \end{pmatrix} + z \right| \\ &= \left| V \left(S^{-1} U^T \begin{pmatrix} g(v_n) \\ 0 \end{pmatrix} + V^T z \right) \right| \qquad (2.9) \\ &= \left| S^{-1} U^T \begin{pmatrix} g(v_n) \\ 0 \end{pmatrix} + V^T z \right| \end{aligned}$$

using the orthonormality of V for the second and third equalities. Now looking at the two terms on the right hand side, the first one is a vector with non-zero components in the i'th position only when $s_i \neq 0$ and the second is a vector with non-zero components in the i'th position only when $s_i=0$. Any non-zero vector z can only therefore increase the length of the vector $|\delta v+z|$.

Further information is yielded by SVD concerning the tangent to the path at the particular solution : this is just the column of V corresponding to the zero singular value. Other path following methods will typically use a finite difference approximation for the tangent of the path, but using SVD we actually compute a tangent as a by product of solving the set of linear equations given by the Newton algorithm 2.7.

2.1.1 Fixed points of autonomous vector fields

A direct application of the above techniques can be used to find fixed points of autonomous vector fields $\dot{x}=F(x,\mu)$ where $x \in \mathbf{R}^n$, $\mu \in \mathbf{R}$, $F:\mathbf{R}^{n+1} \rightarrow \mathbf{R}^n$. Since fixed points of a vector field are given by $\dot{x}=F(x,\mu)=0$, we can just use F as the equivalent of g in equation 2.7 above. If we have F explicitly we can also explicitly calculate the matrix of first differentials necessary for the Newton root finding algorithm.

2.1.2 Fixed points of maps

In order to locate fixed points of a mapping $x_{n+1}=P(x_n;\mu)$ we reformulate the problem to reduce it to one of root finding by defining a residual map $R(x;\mu)=P(x;\mu)-x$. If x^* is a fixed point of the mapping P at a parameter set μ^*, then clearly $R(x^*;\mu^*)=0$. The path following techniques described above can then be used directly on R (R is directly equivalent to the g used in equation 2.7).

2.1.3 The variational method

So far the path following methods discussed have been presented in theoretical terms with no discussion of their practical implementation. An essential requirement of any Newton type root finding algorithm is the first differential matrix of the function whose roots are to be found. In the common case where we are trying to follow the path of a fixed point of the mapping P, where P is not explicitly available because it arises from taking a Poincaré section of a vector field, then we need some way of approximating the matrix of first differentials. In particular we will consider the case of a periodically forced set of o.d.e.'s with our map P defined by taking the stroboscopic Poincaré section t mod $T=0$, where T is the period of the forcing and t

the time variable. The elements of the matrix of first differentials could be computed easily by simple finite difference approximations. A more accurate and efficient way is to use the variational method to compute the matrix of first differentials directly. Using the notation introduced above where $v=(x,\mu)$ we have

$$\dot{v} = f(v;t) \tag{2.10}$$

Differentiating with respect to a set of initial conditions v_0 we have

$$\begin{aligned} D_{v_0}\dot{v} &= D_{v_0} f(v;t) \\ i.e. \quad \frac{d}{dt}D_{v_0}v &= D_v f(v;t) D_{v_0} v \end{aligned} \tag{2.11}$$

Then setting

$$V = D_{v_0} v \tag{2.12}$$

we have a set of equations for the elements of the first differential matrix with respect to a set of initial conditions

$$\dot{V} = D_v f(v,t)\, V \tag{2.13}$$

This set of equations can be numerically integrated along with the original set of first order o.d.e.'s. Starting with initial conditions $t=0$, $v=v_0$ and integrating the equations given by 2.10 and 2.13 for one period until $t=T$ we obtain the image under the stroboscopic Poincaré map from 2.10 and the matrix of first differentials from 2.13. V is an $(n+k)\times(n+m)$ matrix of the first differentials of v at time t with respect to initial conditions v_0. To integrate 2.13 we use initial conditions $V_{ij}=0$ if $i\neq j$, $V_{ij}=1$ if $i=j$.

2.1.4 Following bifurcations

The path following methods described above can be used directly to locate fixed points of a map (and by finding the eigenvalues of the matrix of first differentials, the stability of the fixed points) and following them under the variation of one system parameter. By adding an extra constraint to the set of equations, it is possible for the parameter value at which a bifurcation occurs to be located, and followed. Since we have had to add one constraint, a one dimensional path can be found by allowing an extra parameter to vary. For example, we might follow a period one solution of a map as a parameter corresponding to the frequency is varied and find that at a particular frequency ω_0 there is a saddle node bifurcation. We could then follow the path of that bifurcation as both frequency and another parameter, corresponding say to the amplitude of forcing, are varied. All that is required is to add a suitable constraint equation, for example, for the saddle node bifurcation

$$c(x,\mu) = \det(D_{x_0}P(x) - I)$$

which is zero when the matrix of first differentials of the map P, $D_{x_0}P(x)$, has an eigenvalue of $+1$.

2.2 Location of basins of attraction

In this section we discuss ways in which we can locate the basins of attraction for the various asymptotic steady state solutions of a dynamical system. Recently there has been much interest in the concept of "safe basins" of attraction. In real world dynamical systems, where a physical system is operating in a noisy environment, the classical notions of stability are insufficient to guarantee that the operating conditions are safe. For example, Thompson et al [1990] propose a criterion for ship stability based on the size of the basin area which does not lead to eventual failure. This safe area can be rapidly eroded by incursive fractal "fingers", leading eventually to a situation in which, although there is a stable solution for the system to settle onto, almost any initial condition will lead to failure (i.e. capsize of the ship).

We will restrict ourselves to the discussion of the location of the basins of attraction of a two dimensional map *P*, for example a Poincaré section through a three dimensional flow. A robust approach to locating the basins and their boundaries is to take a grid of starts and iterate each forwards until a steady state behaviour is approximately realised. As the number of points is increased the location of the basin boundaries become better approximated. The computational effort required can soon become restrictive though, especially if working on a microcomputer. The method of cell to cell mapping [Hsu, 1987] for the location of attractors and their basins is ideally suited to the microcomputing environment, and gives a large improvement in efficiency over the 'integration of a grid of points' method.

An area of the Poincaré section is divided into small cells. The essential assumption made is that whole cells map to whole cells. Thus given a starting cell C_1, the centre of which maps under *P* to somewhere in C_2, we assume that we can continue by mapping the centre of C_2 to a point in a cell C_3, where we again re-centre before continuing. We proceed in this way until the string of cells settles on to 'an attractor', that is until a sequence of cells is visited repeatedly in order. The underlying assumption that all points within one cell map to one other cell then implies that all points in all cells in the string settling onto the attractor will themselves converge to that same attractor.

Initially all of the cells are labelled [E] for 'empty'. A starting cell is chosen and labelled [U] for 'under process'. A string of cells is generated as described above by mapping forward the centres of the cells encountered. Each time a new cell labelled [E] is encountered it is re-labelled [U]. When the string lands on a cell already labelled [U] then a limit cycle has been reached. The number of steps taken for this cell to be reached again determines the order of the attractor. Each of the cells in this attracting cycle are labelled as [A1] for 'attractor 1' and the labels of the remaining cells in the string are changed from [U] to [B1] for 'basin 1'. This finishes the processing of this string (see figure 2.3). Now a new cell labelled [E] is chosen and the process continues as before. Any string which now lands on a cell labelled [A1] or [B1] is labelled [B1] since it will eventually map onto the attracting cycle [A1]. New attractors are labelled [A2] , [A3] ,... and their basins labelled [B2] , [B3] ,... . This process is continued until there are no more cells labelled [U].

This algorithm can be seen to be very efficient as compared to a grid of starts by noting that each cell need only be mapped forwards once. With a grid of starts each point might be mapped forwards a large number of times, N say. The computational effort required for cell to cell mapping is decreased by a factor of N. Furthermore, there is no guarantee that even after N iterations convergence will have been reached.

The cell to cell mapping method is particularly well suited to a microcomputing environment where it is possible to use the screen graphics as memory storage. A cell is identified with a single screen pixel, with the labelling achieved by using different screen colours.

Several problems can arise using this algorithm. If the convergence to an attractor is slow it is possible for two or more labels to be assigned to the same underlying attractor. Repellors and saddles may also be labelled as attractors if the divergence is low or if the fixed point lies near the centre of the cell. If there is a chaotic attractor it will be labelled as a high order attracting cycle, since eventually some cell will be revisited. These problems can be avoided by modifying the algorithm slightly. Once an attracting cell cycle is located, processing is continued without re-centring. In this way the true nature of the underlying attractor, if any, can be deduced.

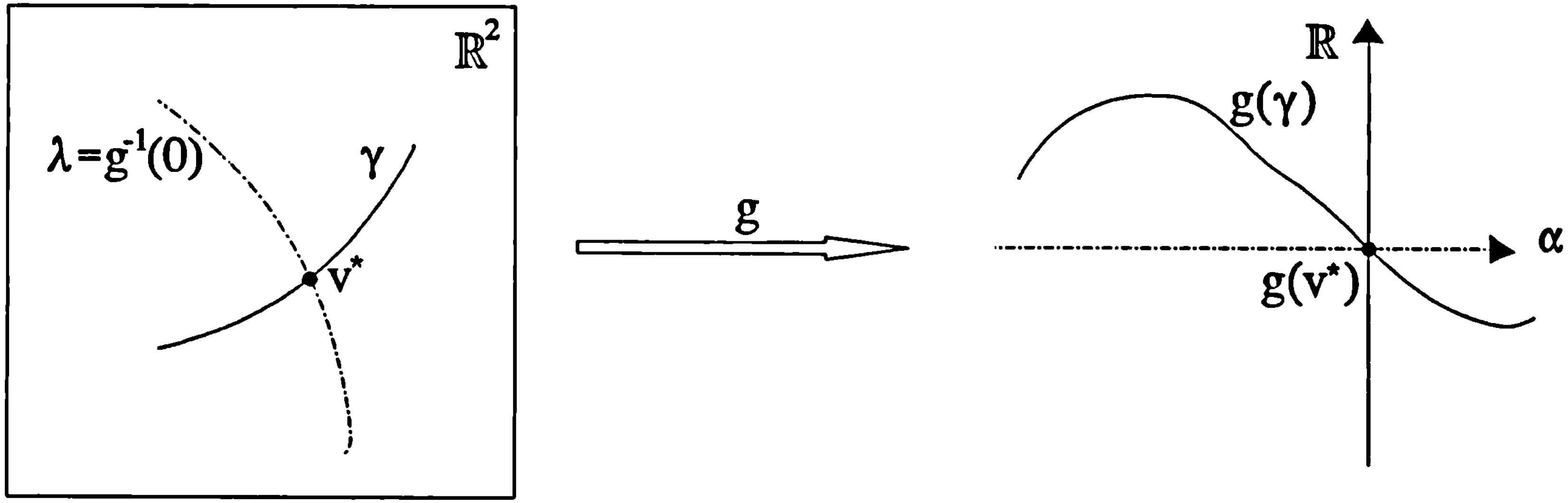

Figure 2.1 Two lines in $\mathbb{R}^2$, λ and γ, parameterised by α, are mapped by g into $\mathbb{R}$. The implicit function theorem implies the existence of $\lambda(\alpha)$ such that $g(\lambda(\alpha))=0$, given the existence of $\gamma(\alpha)$ such that $\gamma(0)=v^*$ and $g(v^*)=0$.

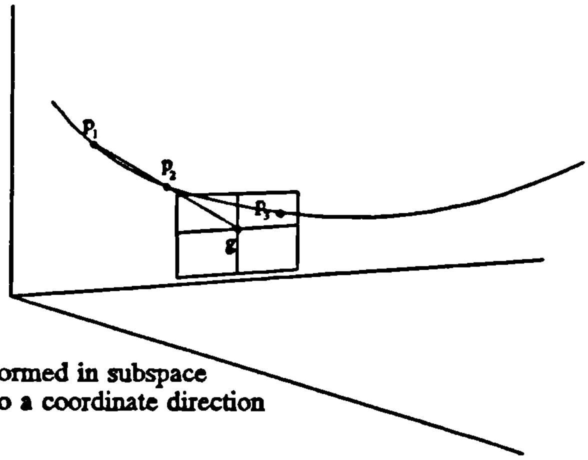

(a) Search performed in subspace perpendicular to a coordinate direction

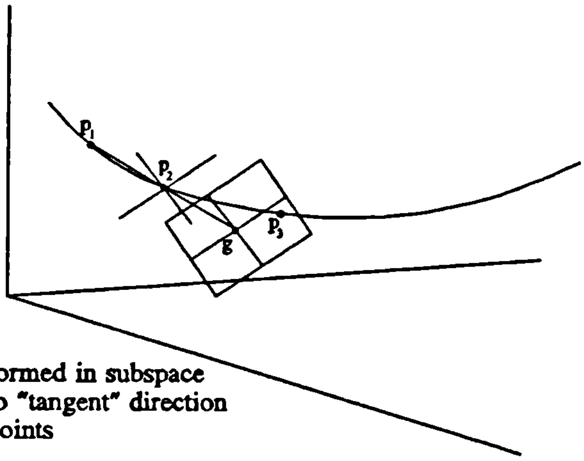

(b) Search performed in subspace perpendicular to "tangent" direction from last two points

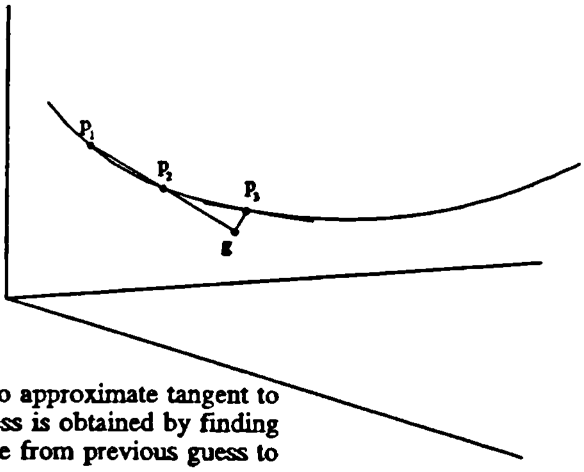

(c) SVD used to approximate tangent to path. Next guess is obtained by finding shortest distance from previous guess to this tangent.

Figure 2.2 Three strategies for path following. In each case p_1 and p_2 are previously located points on the path and g is the linear extrapolation "next guess". In (a) and (b) the Newton search is restricted to a two dimensional subspace perpendicular to a coordinate direction or the tangent direction respectively. In (c) SVD is used to locate an approximate tangent to the path onto which a perpendicular from g is dropped. The new point on the path is p_3.

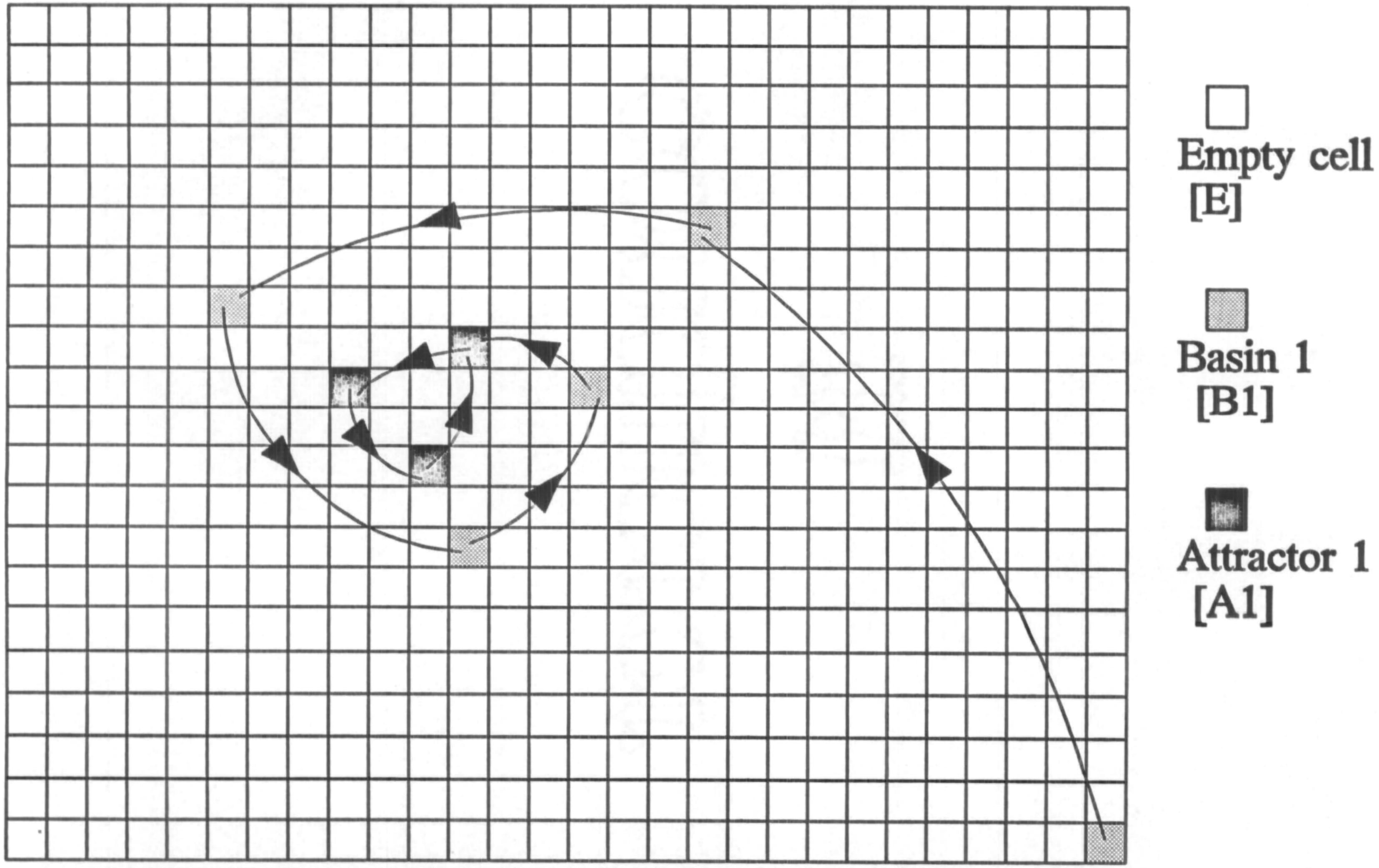

Figure 2.3 The cell-to-cell mapping algorithm. A schematic diagram showing the algorithm starting at an empty cell in the bottom right and falling onto a period three cell-cycle.

3. Impact Oscillators

3.1 Introduction

The mathematical modelling of dynamical systems involving impacts comprises of two parts : the modelling of the system away from the impact and the modelling of the impact process itself. In this chapter, we will concentrate on the second part, the impact process. Between impacts we will use a simple linear stiffness and damping model since this is sufficient to give all of the interesting behaviour which is found to occur in impact oscillators, described in this chapter and the next. Any system which undergoes sudden impacts at rigid stops will however clearly have two distinct regimes, one between impacts and one during impact. Nonlinearities are therefore inherent in models of impact oscillators. In this chapter we first examine some ways of modelling the impact process. We then go on to investigate one particular model in more detail, using the coefficient of restitution rule which is the simplest and most easy to apply impact model. Technical difficulties with this model involving discontinuities caused by it are highlighted and their consequences to the overall dynamical behaviour of the impacting system discussed. One of the advantages of using such a simple model is that much of the dynamical behaviour can be deduced analytically, and these techniques are shown.

3.2 Impact models

In the sections which follow, we describe three different ways in which the impact process can be modelled in an impact oscillator. The emphasis here is on modelling the impact process itself so away from impact, in each case, the dynamical system comprises of just the linearly damped, linear stiffness, sinusoidally forced oscillator described by the second order ordinary differential equation

$$\ddot{x} + d\dot{x} + x = \alpha\cos(\omega t) \quad , x < a \qquad 3.1$$

which is valid when the displacement $x < a$, where $x = a$ is the position of the stop. In equation 3.1 an overdot represents differentiation with respect to the time t, d is the linear damping coefficient, α the amplitude of the forcing function and ω the forcing frequency. In almost all cases, one more system parameter can be eliminated from the above by rescaling the displacement, x, so as the stop is at $x=1$. This does rule out the special case of x=0, so we will use the above form. In equation 3.1 we assume that time and displacement have been rescaled in order to scale to one any mass or stiffness terms. We also note that variation of the forcing amplitude α is directly equivalent (after rescaling) to adjusting the position of the stop. A further rescaling of x by putting $x \rightarrow \alpha x$ in equation 3.1 gives the exactly the same linear oscillator with the stop at a/α, i.e. increasing the amplitude of the forcing by some factor is equivalent to moving the stop closer to the equilibrium position by the same factor. For $x \geq a$ one of the following impact models is applied, giving overall a model of a one sided impact oscillator with a stop at $x=a$.

3.21 Coefficient of restitution (COR) impact model

The coefficient of restitution impact rule (COR) is the simplest to apply in practice and for impacts between hard surfaces, where the impact process takes a small amount of time compared with the time between impacts, can prove effective. In addition to equation 3.1, when the displacement x reaches the position of the stop $x=a$ the rule

$$\dot{x} \rightarrow -r\dot{x} \qquad , x=a \tag{3.2}$$

is applied, where the coefficient of restitution, r lies in the range $0<r\leq 1$. This coefficient, r, is determined empirically for the impact between two surfaces of different material properties. After the rule 3.2 has been applied then the linear oscillator 3.1 takes over again. This rule models two aspects of the impact process. Firstly, the direction of the velocity $\dot{x}$ is reversed and secondly some (kinetic) energy is lost in the process since if $r<1$ the size of the velocity is reduced at impact. The impact process is modelled here as taking place instantaneously. Whilst this is clearly never going to be completely true of any physical impact process, if the time between impacts is long with respect to the time taken for the impact process to occur then the coefficient of restitution rule acts as a reasonable model. Goldsmith [1960] gives some typical values for r for various materials. For example for a baseball against wood $r \approx 0.43$; for an one inch steel sphere against a cast iron plate r varies between 0.7 and 0.9 depending on the velocity of impact. We will always assume however that r is independent of the velocity at impact. The instantaneous reversal of velocity can cause problems when it comes to the more detailed study of the dynamical behaviour of the impact oscillator with a coefficient of restitution impact rule. Clearly this rule is discontinuous in velocity, whereas many of the tools of dynamical systems theory [e.g. Guckenheimer & Holmes, 1990, Thompson & Stewart, 1986] require continuity, and often differentiability to some degree in order to be applied. The consequences of these discontinuities, and further discontinuities in gradient which are caused by this instantaneous impact rule are discussed in subsequent sections. One of the advantages of having such a simple instantaneous impact rule is that, when used in conjunction with a simple linear oscillator away from impacts, much analysis can be performed on the system. Methods for locating simple steady state periodic orbits, their stability characteristics and some bifurcations will be described in later sections.

3.2.2 Hertz impact law

The Hertz impact law [Goldsmith, 1960], which describes the force/deformation relationship between two locally spherical bodies is given by $f=k(x-a)^{3/2}$, where f is the force between the two bodies which are impacting at displacement $x=a$. This impact rule has been used in several structural dynamics problems as a reasonable model for the impact process [Jing & Young, 1990,1991, Tso & Wong, 1989, Davis 1992]. Combining this impact law with equation 3.1 in such a way as to retain continuity we obtain

$$\ddot{x} + d\dot{x} + x + k(x-a)^{3/2} = \alpha\cos(\omega t) \qquad , x \geq a \qquad 3.3$$

where all parameters are as before, and k relates to the particular material properties of the impacting surfaces. Equations 3.1 and 3.3 then make up a one sided Hertz law impact oscillator. The stiffness function in equation 3.3, s, is shown in figure 3.1(a) and the integral with respect to x of this stiffness function, p, which represents the potential energy function of this system is shown in figure 3.1(b).

$$s = x + k(x-a)^{3/2} \qquad 3.4$$

It can be seen that the force exerted after impact rapidly grows to oppose the motion. In contrast to the coefficient of restitution rule, the impact process in this case will not

$$p = \int s\, dx = \frac{x^2}{2} + \frac{2k}{5}(x-a)^{5/2} \qquad 3.5$$

be instantaneous : the time spent in the impact regime will depend on the size of the parameter k and the velocity at which the impact process takes place. There is however no specific energy loss mechanism included in this impact law. The only way that energy will be lost during impact is through the usual linear damping. The equation 3.3 does however describe a continuous and differentiable vector field, which means that the tools of dynamical systems theory can far more readily be applied to this model. The main use we will have for this model later on will be as a 'close' (in some sense), continuous and differentiable system with which to compare the bifurcational behaviour of the COR model.

3.2.3 Piecewise linear stiffness

After the COR model, perhaps the simplest way of modelling the impact process is to regard the stop at which the impact takes place as a very stiff spring. In this case, when equation 3.1 describes the behaviour away from impact, the complete system is described by the equation

$$\begin{gathered} \ddot{x} + d\dot{x} + \kappa(x) = \alpha\cos(\omega t) \\ \kappa(x) = \begin{cases} x & , \ x < a \\ a + k_l(x-a) & , \ x \geq a \end{cases} \end{gathered} \qquad 3.6$$

where k_l is the stiffness after impact. The stiffness function $\kappa(x)$ is shown in figure 3.2(a) and the integral with respect to the displacement, x, of this function which represents the potential energy function of this system is shown in figure 3.2(b). As with the Hertz law model, the force exerted during the impact process grows rapidly to oppose the motion. Also, as with the Hertz law model, the linear damping is the only mechanism for energy loss. Although this impact model has a continuous vector field, it is not differentiable along the line $x=a$. The piecewise linear stiffness model is included here for completeness and since many case studies of systems with impacts have used it. Shaw and Holmes [1983] showed that as $k_l \to \infty$ the time taken in the impact region $x>a$ tends to zero and, if the velocity immediately before impact is y_0

then the velocity immediately after impact tends to $-y_0$, i.e. as the stiffness after impact tends to infinity the piecewise linear impact rule behaves like the COR rule with coefficient of restitution 1.

3.3 Numerical solution of the COR model

The COR model comprising equations 3.1 and 3.2 is governed by the simple linear o.d.e. with sinusoidal forcing 3.1. The numerical solution of this system away from the stop could be achieved by simple numerical integration, for example a variable step size Runge Kutta routine [Press *et al*, 1991]. The impact rule must be applied when an orbit reaches the stop $x=a$, so an additional check must be made at each step of the time integration to inspect the value of x. If this value is greater than a, then either the method of Hénon [1982] , or a root finding method must be used in order to evaluate the time and velocity at which the impact occurs. The coefficient of restitution rule, equation 3.2, can then be applied and the integration continued. However, due to its linear nature, the general solution to equation 3.1 is available (see equations 3.21 & 3.22). A set of initial conditions $(x,\dot{x},t)=(x_I,y_I,t_I)$ define the two constants of integration which then completely define the evolution of the system in time. The solution obtained in this way, valid only until an impact occurs, is allowed to evolve in time by stepping gradually until it is detected that an impact has occurred, $x>a$. A root finding routine is then used to locate the time at which the displacement $x=a$. A good root finding algorithm to use here is Newton-Raphson, which can be applied without any need for further differentiation since expressions for $x(t)$ and $\dot{x}(t)$ are already available. The Newton algorithm requires iteration of $t_{n+1}=t_n-(x(t_n)-a)/\dot{x}(t_n)$. This scheme has quadratic convergence, and so we have an efficient method for very accurately locating the time, and through this the velocity, of the impact. After the impact rule is applied there are a new set of initial conditions which define two new constants of integration. This new solution can again be stepped through gradually until another impact is detected, where the process is repeated. Since no errors accumulate in the time stepping part of this numerical scheme, the only place where errors can occur are in the root finding routine, and this quickly converges to any desired accuracy. There are two additional sources of possible error in this scheme. If the time step is too large to capture a low velocity impact then the important bifurcational events which will be shown to result from low velocity impacts will be missed. This is not too much of a problem since the if a parameter of the system is changed slightly the numerical scheme will detect a low velocity impact, so the bifurcation will just have been slightly shifted in parameter space. The other source of error in this numerical scheme is the possibility that there can be an infinite number of impacts with decreasing velocity in a finite period of time leading to a "sticking" condition, where the displacement is constant (at the stop) for some time before falling off again. As long as neither of these events happen then this gives a very simple to implement and accurate scheme for the numerical evaluation of the COR model.

3.4 Numerical observations of grazing bifurcations

In this section a simple two sided COR impact oscillator is investigated numerically. The numerical observations indicate that there is some "unusual" behaviour associated with low velocity impacts, and it is this behaviour which will be studied at greater length in the following work. Later on, the system which is used in order to try to understand these "unusual" events is the even simpler, one sided COR impact oscillator. Here we are considering the specific two sided coefficient of restitution law impact oscillator

$$\begin{aligned} \ddot{x} + 0.1\dot{x} + x &= \alpha\cos(1.9t) \quad , \quad -1 < x < 1 \\ \dot{x} &\rightarrow -r\dot{x} \quad , \quad |x| = 1 \end{aligned} \qquad 3.7$$

where there is only one free parameter α, the amplitude of the forcing. On inspection, it is clear that for small values of α there will be a simple, non-impacting stable period one solution which is just the solution to the linear o.d.e. as $t \rightarrow \infty$ (see section 3.7.1),

$$x = -\frac{\alpha}{\sqrt{(1.9\times0.1)^2 + (1.9^2-1)^2}}\cos(1.9t+\phi) \quad , \quad \tan(\phi) = \frac{1.9\times0.1}{1.9^2-1} \qquad 3.8$$

Such solutions will be valid if the forcing amplitude α obeys

$$\alpha < \sqrt{(1.9\times0.1)^2 + (1.9^2-1)^2} \approx 2.617 \qquad 3.9$$

, i.e. the maximum displacement $x < 1$ in size. To see numerically how the transition takes place from non-impacting solutions to impacting ones we slowly increase the parameter α in small steps from below this value where the stable non-impacting solution is known to exist. At each new value of α the numerical procedure is allowed to converge on to a fixed point (or series of fixed points), using as an initial condition the final point calculated at the previous parameter value. The newly computed solution will be a continuation of a solution path (as long as the parameter step is small enough), unless a bifurcation has occurred. After a bifurcation, the system will stabilize onto a different, possibly remote attracting solution which in turn is followed.

The attracting non-impacting solution existing at $\alpha = 2.0$ was numerically followed in this way until $\alpha=5.0$. At a sequence of points A-E at $\alpha=2.6, 2.65, 3.0, 3.5$ and 4.25, the attracting orbits onto which the system converged are shown in figure 3.3 in the phase plane projection, where time is projected out and $\dot{x}$ is plotted against x. The position of the x coordinate of the stroboscopic Poincaré map obtained by sampling the system at phase $\theta=t \bmod (2\pi/\omega)=0$ is plotted against the parameter α in the bifurcation diagram, figure 3.4. This bifurcation diagram shows that as α is increased through $\alpha=2.617$, the value at which the non-impacting orbit just starts to touch the stops on either side, there is a sudden jump to a distant solution. The orbits just before this jump at A and just after at B show that there is a sudden jump from a non-impacting solution to a symmetric impacting solution. As α is further increased the symmetry of the impacting solution breaks just before $\alpha=3.0$, which can be seen from orbit at C. At around $\alpha=3.5$ a loop develops on the symmetry broken orbit (the orbit at D), which moves towards the right hand stop at $x=1$, until the loop touches the stop just after E at $\alpha\approx4.3$. At this point, the asymmetric period one impacting solution disappears and the system restabilises onto an apparently chaotic solution.

The numerical observations described above seem to indicate that some kind of bifurcation occurs each time part of an orbit just touches a stop under the change of a parameter. However, if the stability of the fixed point in the stroboscopic Poincaré map is computed as the parameter changes, we do not see any of the usual indications that a bifurcation is about to occur. The standard, smooth bifurcations encountered in nonlinear maps occur when an eigenvalue of the first differential matrix of the map at a fixed point passes through the unit circle on the complex plane, i.e. one direction of the map linearised about the fixed point passes from stable to unstable. Up to the parameter value at which the first transition from non-impacting to impacting solutions occurs, $\alpha\approx2.617$, the stability characteristics of the stable orbit are constant : the eigenvalues of the fixed point of the stroboscopic Poincaré map depend only on the forcing frequency and linear damping coefficients, not on the forcing amplitude. There is clearly some kind of bifurcational event occurring as the stable orbit just touches both stops since there is a large jump in the response (as measured by the position of the Poincaré point), but it cannot be classified as one of the standard bifurcations of smooth dynamical systems. As we will go on to show, these *grazing* bifurcations occur when a part of an orbit just touches a stop with zero velocity. Another way of looking at this bifurcation is that a fixed point of a map from an impact oscillator crosses a line of discontinuity of gradient of the map. This discontinuity in gradient prevents the fixed point being linearised at bifurcation. Grazing bifurcations then are comparable to the "border collision" bifurcations described by Nusse & Yorke [1992].

A further, more detailed investigation of the second grazing bifurcation shown in figures 3.3 and 3.4, just after E shows that the apparent chaotic attractor which results from this bifurcation already "existed", i.e. a different path is followed if the direction of change of parameter is reversed. If we start with initial conditions on the period 4 attractor at $\alpha=4.4$ (just after the chaotic attractor at $\alpha=4.3$) and decrease the parameter α slowly then the complicated response is replicated and then continues below $\alpha=4.3$, as shown in the bifurcation diagram figure 3.5. This chaotic attractor disappears at $\alpha\approx4.28$, where there is a transition to a period 3 attracting solution which continues to $\alpha=4.15$ and beyond. The sequence of bifurcations shown in figure 3.5 is reversible, i.e. the same picture is obtained whether the parameter is increased from $\alpha=4.15$ to $\alpha=4.4$ or decreased. Figure 3.6 shows the period 3 orbit in the phase plane projection at $\alpha=4.28$, just before the complicated, apparently chaotic region appears. Again, we observe that part of a loop is very close to the right hand stop and is just about to graze.

In the bifurcation diagrams 3.4 and 3.5 and the phase plane projections of orbits 3.3 and 3.6, totally "unexpected" bifurcations associated with part of an orbit just grazing a stop have been observed. They are unexpected in the sense that there is no indication that a bifurcation is about to occur from the eigenvalues of the first differential matrix of the stable fixed point which is about to bifurcate. Three grazing events have been shown in these figures. The first, just after A, where the stable non-impacting orbit grazes the stop for the first time, leads to a jump to a distant attracting solution which already "exists". In this case, if the parameter α is decreased from above $\alpha=2.617$ to $\alpha=2$ there is no bifurcation : the system here is said to be hysteretic since a different path is followed on increasing the parameter to that followed decreasing the parameter. The second grazing event, just after E, where part of a loop on an asymmetric period one impacting orbit just touches a stop, is similar. Again there is hysteresis : a different path is followed increasing the parameter to that followed decreasing the parameter. The chaotic attractor onto which the system stabilises after the orbit grazes at the stop already "existed" and so cannot be said to have been "created" at the grazing bifurcation. The third grazing event, where part of a period three impacting orbit just touches a stop differs from the previous two. There is no hysteresis in this case. The same path is followed whichever way the parameter is changed. In this case the chaotic solution which occurs directly after the grazing event can be said to have been "created" at the grazing since it did not exist before.

An analogy can be made between the two types of grazing bifurcation described above and conventional saddle-node and flip bifurcations which occur in smooth maps. At a saddle-node bifurcation (where an eigenvalue of the first differential matrix of a map passes through $+1$) a stable and unstable fixed point come together and annihilate one another under the change of a parameter. After a saddle-node bifurcation there will be a jump to a distant attracting solution, but in general, if the parameter is then reversed, no bifurcation will occur in the opposite direction. This is qualitatively similar to the first two grazing events described above. After a supercritical flip bifurcation in a smooth map, a stable period n solution will period double : a stable period $2n$ fixed point solution will have been "created" at the bifurcation along with an unstable period n solution. This appears similar to the third grazing event described above. This apparent similarity will be expanded upon further in later sections.

3.5 Continuity considerations in the COR model

As discussed above in the section describing the COR model, the instantaneous reversal of velocity in the COR rule causes a discontinuity in the vector field described by the equations 3.1 and 3.2 together. We can define a three dimensional vector field from this second order o.d.e. by rewriting 3.1 as

$$\begin{aligned} \dot{x}_1 &= x_2 \\ \dot{x}_2 &= \alpha\cos(\omega\theta) - dx_2 - x_1 \\ \dot{\theta} &= 1 \end{aligned} \qquad 3.10$$

where the displacement $x=x_1$, velocity $\dot{x}=x_2$ and time, t has been replaced by $\theta = t \bmod 2\pi/\omega$, since the only place where time appears is in the periodic cosine function. Thus the vector field defined by 3.1 occupies the three dimensional space $R^2 x S^1$ illustrated in figure 3.7, and a three dimensional subspace of this when the constraint 3.2 is imposed. In section 1.2.1 the technique was described for reducing the dimension of a continuous time dynamical system by defining a surface of section transversal to the flow on a vector field, and then a Poincaré mapping which takes this surface back onto itself. In order to study the dynamics of the COR impact oscillator model it is convenient to define such a discrete time mapping. The discontinuities in the flow lead to problems in defining a surface of section which is valid everywhere. Two 'natural' surfaces of section are discussed below, and their advantages and disadvantages are considered. Whilst neither section is globally valid, in that both lead to maps which are discontinuous, there are only one dimensional sets of "bad points" and so, if used carefully, the reduction to a mapping is still possible and useful.

3.5.1 The impact map

One of the most natural surfaces of section which we can choose to reduce the dimension in the COR model is the stop itself. We define the impact section $\Sigma_i = \{\xi = (\xi_1, \xi_2) : (x, \dot{x}, \theta) = (a, \xi_1, \xi_2), \xi_1 > 0\}$, the positive half plane at the stop, and the impact map $P_i : \Sigma_i \to \Sigma_i$. The restriction to the positive half plane is possible since any orbit which impacts at the stop must do so with positive velocity. The condition which must be satisfied for a section to define a globally valid Poincaré map is that all orbits must be transverse to the section Σ_i. It is immediately obvious from the definition of the section that there is a line of points in Σ_{i-}, $\xi=(0,\theta)$, along which the flow is tangential to Σ_{i-} (inspection of equation 3.10 shows that the flow is always tangential to the velocity axis when the velocity is zero). It is also important to note that due to the linear damping in the o.d.e. describing the flow away from the stops, not all points in the section Σ_{i-} necessarily map back to this section : some orbits starting in the section could fall asymptotically on to a non-impacting periodic solution so the mapping is not surjective.

3.5.2 The stroboscopic section

A mapping can be obtained from any periodically forced dynamical system by sampling at a constant phase of the forcing. We define the stroboscopic section for 3.10, sampling at phase zero, $\Sigma_s=\{\xi=(\xi_1,\xi_2):(x,\dot{x},\theta)=(\xi_1,\xi_2,0)\}$, and the stroboscopic map $P_s:\Sigma_s\rightarrow\Sigma_s$. In any continuous periodically forced system the stroboscopic section is valid since $\dot{\theta}=1$ so the flow is perpendicular to the section. In the case of the COR impact oscillator, the impact rule is discontinuous at the stop, $x=a$. Although the flow is transverse to the section both before the impact rule is applied and afterwards, there is a discontinuous jump in velocity at the stop.

3.5.3 Discontinuities in P_{i-} and P_s

Define the preimage under the impact map of the line of zero velocity at the stop in the COR model $\lambda_{-1}=P^{-1}{}_{i-}(\lambda_0)$ where $\lambda_0=(0,\theta_0)\in\Sigma_{i-}$, $\lambda_{-1}=(y_{-1},\theta_{-1})\in\Sigma_{i-}$. In this section it is shown that on either side of this line λ_{-1} the mapping P_{i-} will behave in two distinct ways. The orbit starting from a point on one side (the impact side) of λ_{-1} will undergo a low velocity impact in time close to the time $\theta=\theta_0-\theta_{-1}$. On the other side of λ_{-1} the orbit will just miss the stop in a time close to θ and the next impact (if any) will not necessarily be close to the line λ_0. The mapping P_{i-} is therefore discontinuous along the line λ_{-1}. This is numerically demonstrated in figure 3.8, where a rectangular area over the line λ_{-1} for a particular one sided impact oscillator is mapped forwards once under the impact map P_{i-}. The image of the rectangular area consists of two distinct disconnected areas. This discontinuity of the impact map comes directly from the observation discussed in the previous section that the flow is not transverse to the surface of section along the zero velocity line. Any surface of section which has such properties will have similar kinds of discontinuity. This discontinuity is thus essentially artificial : it comes from a 'bad' choice of section. It has been discussed at some length here since the many papers in the literature have been concerned with the discontinuity of the impact map. As will be shown later, along the line of discontinuity in the impact map, the map is also discontinuous in gradient, and it is this property which causes much of the interesting bifurcational behaviour of COR impact oscillators.

Define the preimage under the stroboscopic map of a line along the stop in the COR model $\Lambda_{-1}=P^{-1}{}_s(\Lambda_0)$ where $\Lambda_0=(a,y_0)\in\Sigma_s$, $\Lambda_{-1}=(x_{-1},y_{-1})\in\Sigma_s$. This line is a line of discontinuity of the map P_s. On one side of the line Λ_{-1} points are mapped near to the stop with positive velocity (just before impact) and on the other side points are mapped near to the stop with negative velocity (just after the impact rule has been applied). This is numerically demonstrated in figure 3.9, where a rectangular area over the line Λ_{-1} for a particular impact oscillator is mapped forwards once under the stroboscopic map P_s. The image of the rectangular area consists of two distinct disconnected areas bordered by the stop, one with positive and one with negative velocity. Here the discontinuity is a direct result of the discontinuous COR rule, and not just a result of a bad choice of surface of section. However, both parts of the image border the stop and the relationship between points at the stop with positive velocity and points at the stop with negative velocity is simply given by the impact rule. This is a very 'simple' form of discontinuity : if a fixed point of P_s exists with positive velocity near to the stop, and under a smooth change of parameter moves towards the stop, reaching the stop at positive velocity v_f, a fixed point will 'emerge' with negative velocity $-rv_f$. By sampling at a different phase, this particular discontinuous jump would not occur, although any stroboscopic map will have its own one dimensional discontinuous set.

3.6 Discontinuities in gradient from the COR model

We have seen in section 3.4 that numerical observations indicate that some sort of bifurcation occurs in a COR impact oscillator when part of an orbit just touches a stop with zero velocity. This bifurcational event occurs when a stable fixed point of the map crosses a line of discontinuity in gradient (in fact a square root singularity in the derivative of the map). It is possible to show how this square root singularity in the derivative arises by expanding for a small time backwards and forwards in time from a low velocity impact. Let us take a dynamical system which is governed by a smooth second order ordinary differential equation with periodic forcing away from the impact, with the coefficient of restitution rule $\dot{x} \to -r\dot{x}$ applied at impact. Suppose that a low velocity impact occurs with velocity $\dot{x}=\theta \ll 1$ at time t_0. We will try to obtain the mapping from the plane defined by $t=t_1$ to the plane $t=t_2$ (see figure 3.10) where $t_1<t_0<t_2$, $\Delta t_1=t_0-t_1 \ll 1$, $\Delta t_2=t_2-t_0 \ll 1$, by expanding in the small variables defined above. The mapping takes the point (ξ_1,η_1,t_1) to (ξ_2,η_2,t_2) undergoing a low velocity impact at (a,θ,t_0) in the process. Expanding backwards from the impact we have

$$\xi_1 = a - \theta\Delta t_1 + A_1\Delta t_1^2 + \ldots \qquad 3.11$$

$$\eta_1 = \theta - \Delta t_1 A_1 + \ldots \qquad 3.12$$

and expanding forwards from the impact, after the application of the impact rule we have

$$\xi_2 = a - r\theta\Delta t_2 + A_2\Delta t_2^2 + \ldots \qquad 3.13$$

$$\eta_2 = -r\theta + A_2\Delta t_2 + \ldots \qquad 3.14$$

where A_1 and A_2 are the accelerations at the impact with positive and negative velocities respectively.

Now 3.12 gives θ

$$\theta = \eta_1 + \Delta t_1 A_1 + \ldots \tag{3.15}$$

and substituting 3.15 into 3.11 gives an expression for Δt_1

$$\Delta t_1 = \frac{-\eta_1 + \sqrt{\eta_1^2 - 2A_1(\xi_1 - a)}}{A_1} \tag{3.16}$$

where we take the positive root since when $\Delta t_1 = 0$ we must have that $\xi_1 - a = 0$. Now we define the total time between the initial and final times

$$\Delta t = \Delta t_1 + \Delta t_2 \tag{3.17}$$

Then, using 3.15, 3.16 and 3.17 in 3.13 and 3.14 we obtain expressions for ξ_2 and η_2

$$\xi_2 = (a - \xi_1)\left[2r + \frac{A_1}{A_2}\right] + a - r\eta_1 \tag{3.18}$$

$$\eta_2 = -\sqrt{\eta_1^2 - 2A_1(\xi_1 - a)}\left[\frac{A_2}{A_1} + r\right] + \eta_1\frac{A_2}{A_1} + A_2\Delta t \tag{3.19}$$

We note that

$$\theta = \sqrt{\eta_1^2 - 2A_1(\xi_1 - a)} + \ldots \tag{3.20}$$

so that, as the velocity of the impact tends to zero the expression under the square root tends to zero. The mapping from t_1 to t_2 given by equations 3.18 and 3.19 is only valid where $\theta > 0$. If $\theta < 0$ there is no impact between t_1 and t_2 and so a simple linear mapping which is such that the whole mapping is continuous takes a point (ξ_1, η_1, t_1) to (ξ_2, η_2, t_2) if Δt is small enough. The further mapping from t_2 back to $t_1 + T$ (assuming that the oscillator is periodically forced with period T this forms the stroboscopic Poincaré map sampled at phase t_1), if it has no further low velocity impacts, will also be a simple linear mapping locally. The total map, composed of the mapping around the low velocity impact and the further mapping back onto the plane $t = t_1$ has two distinct regions separated by the line $\theta = 0$. When $\theta < 0$ both parts of the total mapping behave in a simple locally linear manner, and so the resulting total mapping will also behave in a simple, locally linear manner. When $\theta > 0$ there is a square root term in the mapping around the low velocity impact, and thus in the total mapping. As $\theta^2 \to 0$ from above this square root term goes to zero, and the first differential of this mapping with respect to ξ_1 and η_1 will have terms involving $1/\theta$. There will therefore be a square root singularity in the derivative of the mapping on the impact side of the line $\theta=0$, although continuity will still be preserved. This discontinuity in gradient is very important to the dynamical behaviour of the impact oscillator.

Figure 3.11 shows a numerically calculated illustration of such a square root singularity. A rectangular area lying over a discontinuity in gradient of a stroboscopic Poincaré map from a one sided COR impact oscillator was mapped forwards one iteration and here x_{n+1} is plotted vertically against $x_n, \dot{x}_n$. The square root singularity is clearly evident. The effect of this form of discontinuity in gradient on an area which lies over the discontinuity in gradient is shown in figure 3.12. Figure 3.12a shows a small rectangle lying over part of the line of discontinuity of gradient in a stroboscopic map from a one sided impact oscillator. Figure 3.12b shows its image under one iteration of the map. Orbits which pass through the rectangle on one side of the line of discontinuity in gradient go on to just hit the stop with low velocity, while orbits which pass through the rectangle on the other side just miss the stop. On the low velocity impact side, there is a large degree of stretching and so the image is long, thin, almost one dimensional. On the other side, where orbits just fail to impact, there is no significant stretching. In the next chapter, the effect of a fixed point crossing this line of discontinuity under the change of a parameter is investigated through analytical steady state solutions to the one sided COR impact oscillator. The methods for locating such solutions are developed in the following sections.

3.7 Locating steady state periodic solutions of the COR model

3.7.1 General solution away from impacts

The strategy for the location of particular steady state periodic solutions of COR impact oscillators which behave linearly between impacts has been widely used, for example [Shaw, 1985, Shaw & Holmes, 1983c, Whiston, 1987b]. The general idea is that the solution of the linear oscillator away from impacts is known, and so conditions for simple steady state solutions with low period and low numbers of impacts can often be written down and solved analytically. The derivation is repeated here since the expressions obtained will be used later to analyse the behaviour of a COR impact oscillator when part of an orbit just touches a stop with zero velocity at a grazing bifurcation. First, we solve the second order linear o.d.e. 3.1 to find the general solutions away from impact. In subsequent sections, the matching conditions for particular steady state solutions are imposed and expressions for points on these solutions are obtained.

Away from any impacts, 3.1 has general solution

$$x = e^{-\beta(t-t_l)}[A\cos\Omega(t-t_l) + B\sin\Omega(t-t_l)] - \frac{\alpha}{\gamma}\cos(\omega t+\phi) \qquad 3.21$$

Differentiating this with respect to t gives

$$\begin{aligned}\dot{x} = & -\beta e^{-\beta(t-t_l)}[A\cos\Omega(t-t_l) + B\sin\Omega(t-t_l)] + \\ & e^{-\beta(t-t_l)}[-A\Omega\sin\Omega(t-t_l) + B\Omega\cos\Omega(t-t_l)] \\ & + \frac{\alpha\omega}{\gamma}\sin(\omega t+\phi)\end{aligned} \qquad 3.22$$

where

$$A = x_l + \frac{\alpha}{\gamma}\cos(\omega t_l+\phi) \qquad 3.23$$

$$B = \frac{1}{\Omega}[y_l + \beta x_l + \frac{\alpha\beta}{\gamma}\cos(\omega t_l+\phi)-\frac{\alpha\omega}{\gamma}\sin(\omega t_l+\phi)] \qquad 3.24$$

$$\tan\phi = \frac{d\omega}{\omega^2-1} \; ; \; \gamma = \sqrt{(d\omega)^2 + (\omega^2-1)^2} \; ; \; 2\beta = d \; ; \; \Omega = \sqrt{1-\beta^2}. \quad 3.25$$

3.7.2 Period one, one impact solutions

The simplest steady state solutions with impacts of the system defined by 3.11 are of period one (i.e. they repeat once in a complete forcing cycle) and undergo only one impact per period. In order to locate such solutions we impose these conditions on the general solution for 3.1 given above. We take initial conditions at the stop $(x,\dot{x},t)=(a,y_i,t_i)$ before imposing the coefficient of restitution rule. After applying the impact rule we have $(x,\dot{x},t)=(a,-ry_i,t_i)$ which defines the constants A and B in terms of the unknowns y_i and t_i. Then 3.21 and 3.22 are equations for x and $\dot{x}$ as functions of y_i, t_i and time t. By adding the matching conditions which need to be satisfied at a steady state period one, one impact per period, periodic orbit we have the conditions that $x(t_i+2\pi/\omega;y_i,t_i)=a$, $\dot{x}(t_i+2\pi/\omega;y_i,t_i)=y_i$. Using these conditions, 3.21 and 3.22 can be rewritten by collecting together terms in $c_i=\cos(\omega t_i+\phi)$, $s_i=\sin(\omega t_i+\phi)$, and constants depending only on the parameters to give:

$$-ry_i = l_1c_i + l_2s_i + l_3 \qquad 3.26$$

$$0 = m_1c_i + m_2s_i + m_3 \qquad 3.27$$

where the coefficients l_1,l_2,l_3,m_1,m_2,m_3 are given by the expressions below which are functions only of the system parameters

$$
\begin{aligned}
l_1 &= \frac{\Omega\mu}{s_w}\left[\frac{1}{\nu} - c_w\right] - \mu\beta \\
l_2 &= \mu\omega \\
l_3 &= \frac{a}{\mu} l_1
\end{aligned}
\qquad 3.28
$$

$$
\begin{aligned}
m_1 &= \frac{l_1}{r} + \nu\mu\left\{\frac{\Omega c_w}{s_w}\left[\frac{1}{\nu} - c_w\right] - \Omega s_w - \frac{\beta}{\nu}\right\} \\
m_2 &= \mu\omega\left[1 + \frac{1}{r}\right] \\
m_3 &= \frac{a}{\mu} m_1
\end{aligned}
\qquad 3.29
$$

$$
\mu = \frac{\alpha}{\gamma} \;;\; \nu = e^{-\beta(t_f - t_i)} \;;\; c_w = \cos\Omega(t_f - t_i) \;;\; s_w = \sin\Omega(t_f - t_i) \;;\; t_f - t_i = \frac{2\pi}{\omega} \qquad 3.30
$$

Now if we treat 3.26 and 3.27 as simultaneous equations in c_i and s_i we can obtain

$$
\begin{aligned}
s_i &= \frac{r y_i}{\dfrac{m_2}{m_1} l_1 - l_2} \\
c_i &= -\frac{\dfrac{m_2}{m_1} r y_i}{\dfrac{m_2}{m_1} l_1 - l_2} - \frac{m_3}{m_1}
\end{aligned}
\qquad 3.31
$$

And we can eliminate time completely by noting that $c_i^2 + s_i^2 = 1$, ie.

$$
\frac{r^2 y_i^2}{\left[\dfrac{m_2}{m_1} l_1 - l_2\right]^2}\left[1 + \left[\frac{m_2}{m_1}\right]^2\right] + 2\left[\frac{m_3}{m_1}\right]\frac{\dfrac{m_2}{m_1} r y_i}{\dfrac{m_2}{m_1} l_1 - l_2} + \left[\frac{m_3}{m_1}\right]^2 = 1 \qquad 3.32
$$

This is a quadratic equation in y_i which we can easily solve, then by substituting this into one of 3.31 we have an expression for the other unknown quantity t_i. Therefore, at a given set of parameters we have possible solutions for y_i and t_i which define a point on a steady state, period one, one impact per period orbit of the system defined by 3.1 and 3.2 together. It is only a possible solution : we must ensure that $x=a$ at times t_i and $t_i+2\pi/\omega$ but at no time in between, since this would correspond to a non-physical orbit, as shown in figure 3.13. Any possible solution must be numerically verified to ensure that it is a true, physical solution. Since very accurate numerical schemes can be used to calculate the time evolution of this COR impact oscillator (see section 3.3), using this analytical technique with numerical checks is a very accurate way of finding period one, one impact solutions.

3.7.3 Extension to symmetric, period one two sided impact solutions

A simple extension of the method for obtaining analytical period one, one impact, steady state solutions for the one sided one impact oscillator 3.1 & 3.2 allows period one symmetric steady state solutions of the two sided impact oscillator 3.33 to be found.

$$\begin{array}{lll} \ddot{x} + d\dot{x} + x = \alpha\cos(\omega t) & , & -a<x<a \\ \dot{x} \rightarrow -r\dot{x} & , & |x| = a \end{array} \qquad 3.33$$

A symmetric period one impacting solution with one impact at either stop can be found by considering only the first half of the period. Starting with initial conditions at the left stop $(x,\dot{x},t)=(a,y_i,t_i)$, reflected immediately to $(x,\dot{x},t)=(a,-ry_i,t_i)$, we impose the matching conditions that the impact at the right stop after half of a forcing period are $(x,\dot{x},t)=(-a,-y_i,t_i+\pi/\omega)$. If we put $x \rightarrow -x$ in the differential equation 3.33 and shift the phase of the forcing function by half a period then we see that the equation controlling the flow in the second half of a forcing period is the same as that controlling the flow in the first half, with $x \rightarrow -x$ (and therefore $\dot{x} \rightarrow -\dot{x}$). Thus once this matching condition has been reached, the orbit in the next half period must reach the original initial condition at the end of the second half period. This technique does not ensure that analytical solutions can be found for all period one solutions which impact once at either stop, but only those with the symmetry described above. Using almost exactly the same strategy as used in section 3.72 we impose the matching conditions $(x,\dot{x},t)=(-a,-y_i,t_i+\pi/\omega)$ onto the solutions 3.21 and 3.22 for the differential equation 3.1 where the constants of integration A and B are defined by the initial conditions just after impact $(x,\dot{x},t)=(a,$-

$ry_i,t_i)$. Again, terms in c_i,s_i and y_i can be collected together to give

$$-ry_i = p_1 c_i + p_2 s_i + p_3 \qquad 3.34$$

$$0 = q_1 c_i + q_2 s_i + q_3 \qquad 3.35$$

where

$$\begin{aligned} p_1 &= -\left[\frac{\Omega\mu}{s_w}\left[\frac{1}{\nu}+c_w\right]+\mu\beta\right] \\ p_2 &= \mu\omega \\ p_3 &= \frac{a}{\mu}p_1 \end{aligned} \qquad 3.36$$

$$\begin{aligned} q_1 &= -\frac{\mu\omega s_w}{\Omega}-p_1\left[\frac{\nu\beta s_w}{\Omega}-\nu c_w+\frac{1}{r}\right] \\ q_2 &= -\mu\omega\left[1+\frac{1}{r}\right] \\ q_3 &= \frac{a}{\mu}q_1 \end{aligned} \qquad 3.37$$

$$\mu=\frac{\alpha}{\gamma}\ ;\ \nu=e^{-\beta(t_f-t_i)}\ ;\ c_w=\cos(\Omega(t_f-t_i))\ ;\ s_w=\sin(\Omega(t_f-t_i))\ ;\ t_f-t_i=\frac{\pi}{\omega} \qquad 3.38$$

So by replacing l_1,l_2,l_3 with p_1,p_2,p_3 and m_1,m_2,m_3 with q_1,q_2,q_3 in 3.31 and 3.32 we obtain expressions for y_i and t_i in exactly the same way as for the analytical one sided period one steady state solutions. Again, the solutions obtained in this way are only possible solutions. Non-physical orbits will occur exactly as for the one sided impact oscillator and numerical checks must be made to ensure that the analytical solution found is a true, physical one.

3.7.4 Stability analysis of period one, one impact solutions

We have given above a method for locating a point on a steady state, period one, one impact per period orbit of the system defined by equations 3.1 & 3.2. Since this point is always on the plane $x=a$ (the stop) we can regard it as a fixed point of the mapping which takes this plane onto itself. This *impact map* , $P_i{:}\Sigma_{i-}\rightarrow\Sigma_{i-}$ where $\Sigma_{i-} = \{\xi=(\xi_1,\xi_2):(x,\dot{x},t)=(a,\xi_1,\xi_2),\xi_1>0\}$ is one of the 'natural' Poincaré maps which can be defined by taking a section almost everywhere transverse to the flow defined by 3.1, as discussed in section 3.7. It is only almost everywhere transverse to the flow since along the zero velocity line $\dot{x}=0$ the flow is always tangential to the plane $x=a$. We can similarly define $\Sigma_{i+}=\{\xi=(\xi_1,\xi_2):(x,\dot{x},t)=(a,\xi_1,\xi_2),\xi_1<0)$. Then the total mapping $P_i{:}\Sigma_{i-}\rightarrow\Sigma_{i-}$ is made up of two parts : the instantaneous reversal of velocity by the impact rule $P_r{:}\Sigma_{i-}\rightarrow\Sigma_{i+}$, and the rest of the mapping $P_p{:}\Sigma_{i+}\rightarrow\Sigma_{i-}$. Now we differentiate 3.21 and 3.22 with respect to the initial time and velocity t_i and y_i and evaluate at $t_f=t_i+2\pi/\omega$ to give the elements of the first differential matrix of the mapping from $\xi_{i+}=(-ry_i,t_i)$ to $\xi_{i-} =(y_f,t_f)$ and we set $y_f=y_i$ since we are at a fixed point of the map P_i.

$$\frac{\partial t_f}{\partial y_i} = -\frac{\nu s_w}{\Omega y_f} \tag{3.39}$$

$$\frac{\partial t_f}{\partial t_i} = 1-\frac{\mu\omega}{y_f}\left[s_i-\nu s_i c_w-\frac{s_w}{\Omega}(\beta s_i+\omega c_i)\right] \tag{3.40}$$

$$\frac{\partial y_f}{\partial y_i} = \frac{\partial t_f}{\partial y_i}\ddot{x}_f+\nu\left(c_w-\frac{\beta s_w}{\Omega}\right) \tag{3.41}$$

$$\frac{\partial y_f}{\partial t_i} = \left(\frac{\partial t_f}{\partial t_i}-1\right)\ddot{x}_f+\mu\omega\nu\left[\frac{s_w}{\Omega}(s_i+\beta\omega c_i)-\omega c_i c_w\right]+\mu\omega^2 c_i \tag{3.42}$$

The acceleration at impact is denoted by $\ddot{x}_f$. The mapping $P_r{:}\Sigma_{i-}\rightarrow\Sigma_{i+}$ which takes the initial point $\xi_{i-}=(y_i,t_i)$ with positive velocity to the point $\xi_{i+}=(-ry_i,t_i)$ also contributes to the total first differential matrix **D** of the impact map, which by the chain rule is given by

$$DP_i = DP_r DP_p = \begin{bmatrix} -r & 0 \\ 0 & 1 \end{bmatrix} \begin{bmatrix} \frac{\partial y_f}{\partial y_i} & \frac{\partial y_f}{\partial t_i} \\ \frac{\partial t_f}{\partial y_i} & \frac{\partial t_f}{\partial t_i} \end{bmatrix} \qquad 3.43$$

From 3.43 we have the trace and determinant of **D**, tr(**D**) and det(**D**) respectively

$$\begin{aligned} \det(D) &= \nu^2 r^2 \\ tr(D) &= 1 - r\nu c_w - \frac{\beta \nu r s_w}{\Omega} + \frac{s_i \mu \omega}{y_f}\left[\frac{\beta \nu s_w}{\Omega}(1+2r) + \nu c_w - 1\right] + \\ &\qquad \frac{\nu c_i s_w}{\Omega y_f}\left[\mu\omega^2 - \mu r + \mu\omega^2 r - a r\right] \end{aligned} \qquad 3.44$$

The eigenvalues of the first differential matrix of the impact mapping are given then by

$$\lambda_{1,2} = \frac{tr(D) \pm \sqrt{tr(D)^2 - 4\det(D)}}{2} \qquad 3.45$$

and so it is clear that as $y_f \to 0$ one of the eigenvalues will tend to either positive or negative infinity (and since the map is dissipative overall and the product of the eigenvalues equals the determinant, the other eigenvalue must tend to zero with the same sign). Steady state solutions with very low velocity impacts will therefore be saddle solutions with one direction of large expansion and one of large contraction. This observation ties in with the previous observations of a square root singularity in a Poincaré mapping from an impact oscillator. We see again that a grazing bifurcation occurs at parameter values where the velocity at impact of a steady state periodic orbit equals zero.

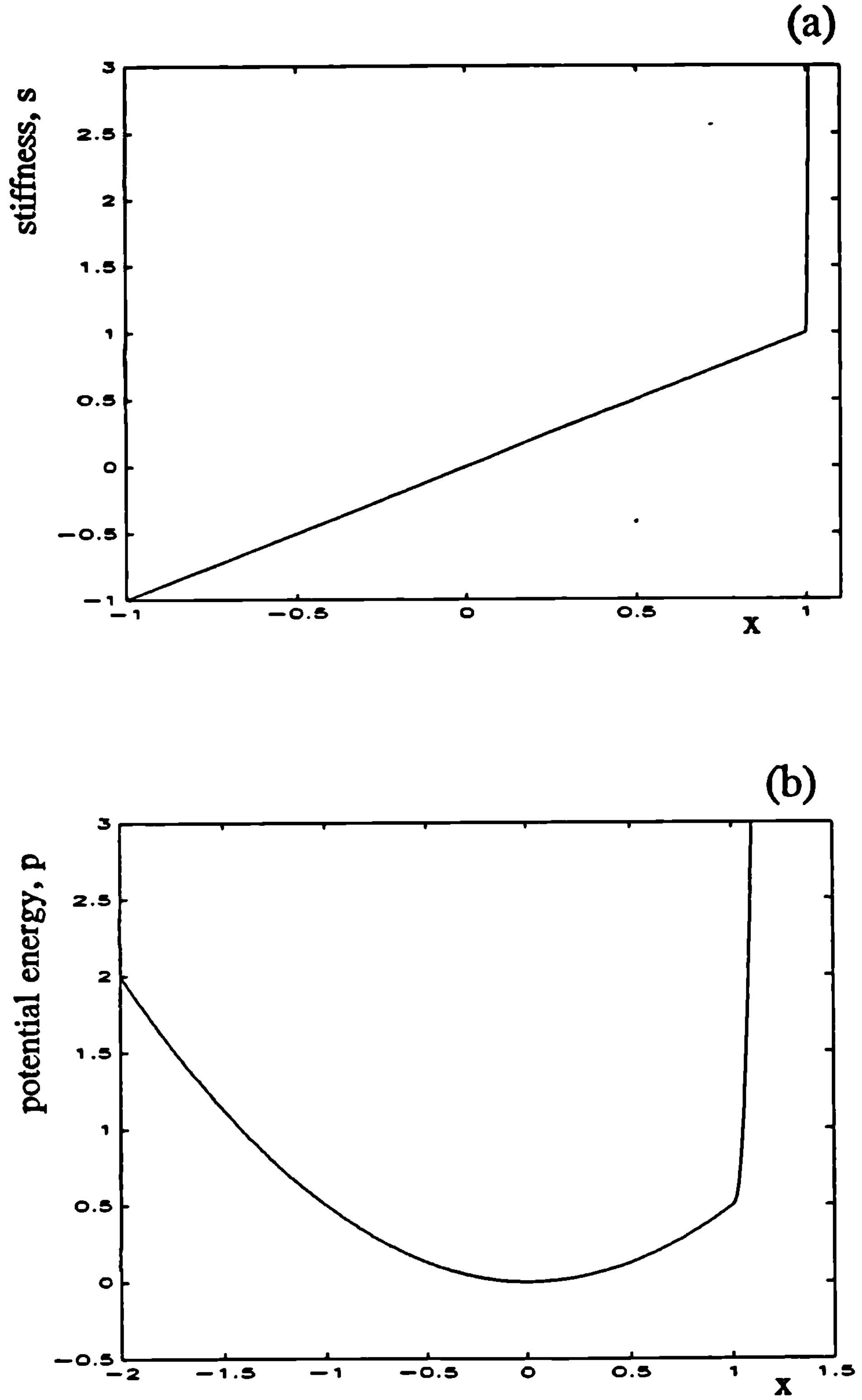

Figure 3.1 (a) Stiffness and (b) potential energy functions for the Hertz law model, equations 3.1 and 3.3, k=2000.

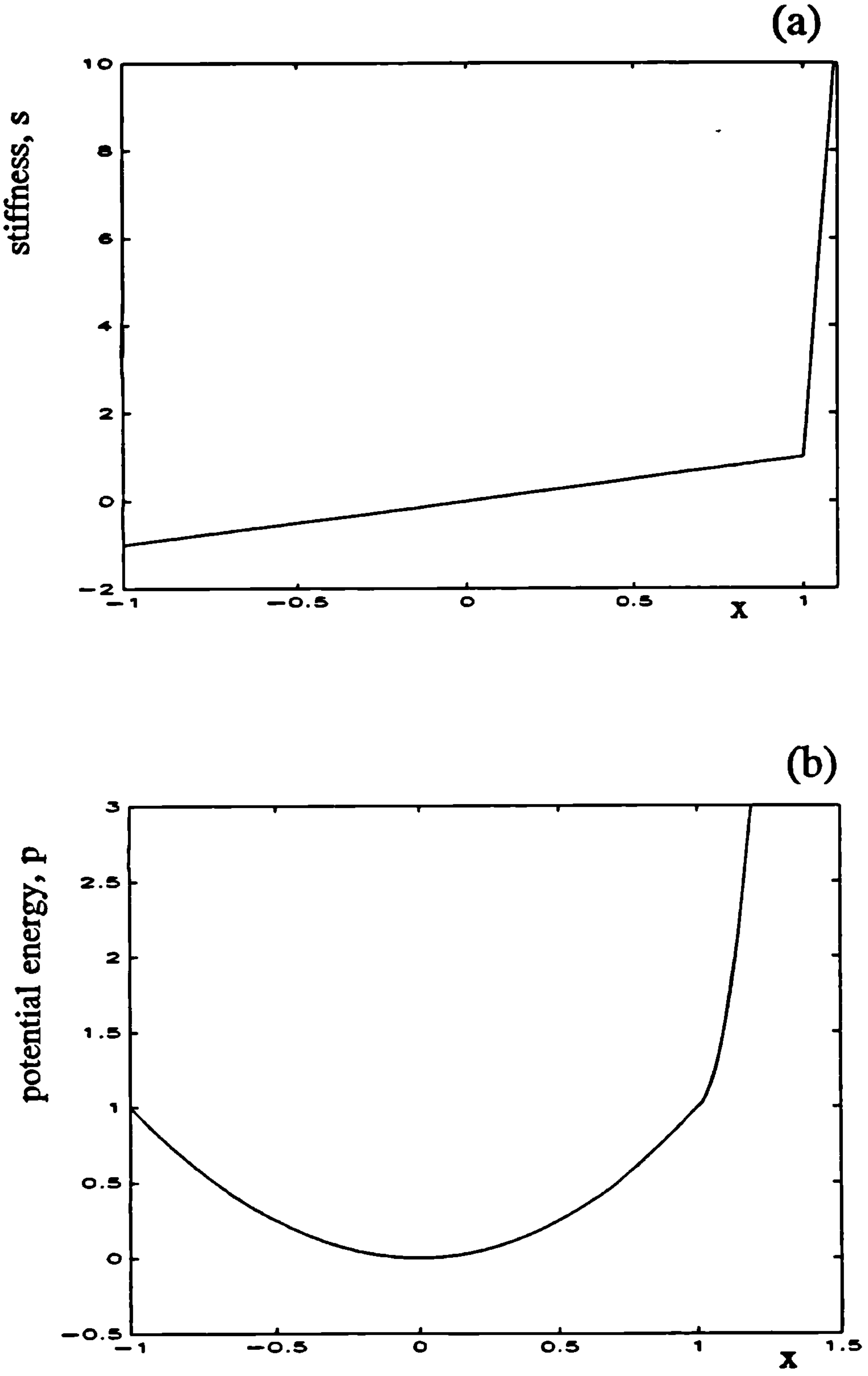

Figure 3.2 (a) Stiffness and (b) potential energy functions for the piecewise linear model, equation 3.6, $k_I = 100$.

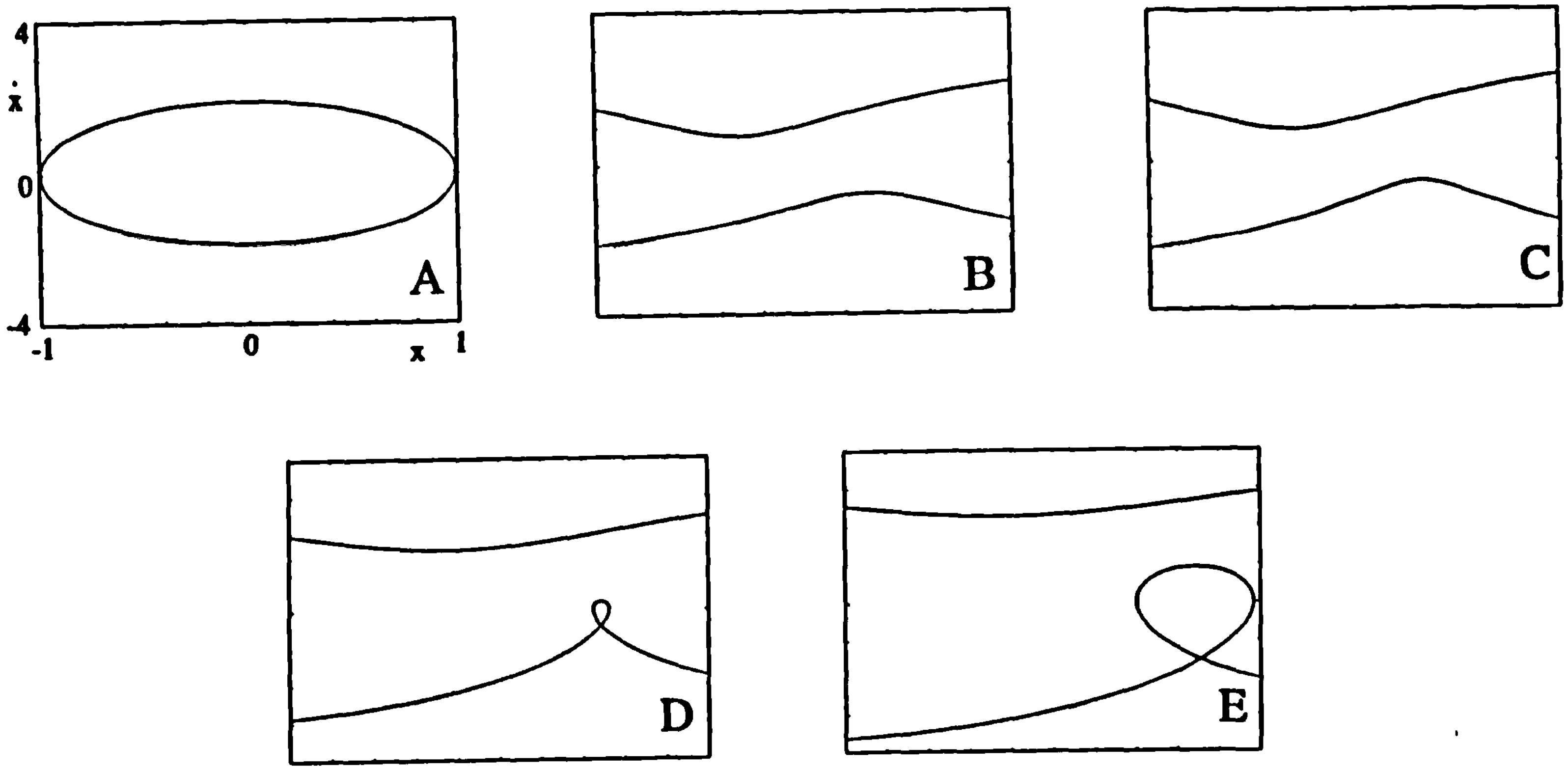

Figure 3.3 Phase plane projections ($\dot{x}$ against x) of period one orbits for equation 3.7 at A, ω=2.6; B, ω=2.65; C, ω=3.0; D, ω=3.5; E, ω=4.25. In each case the axes are $-1<x<1$, $-4<\dot{x}<4$.

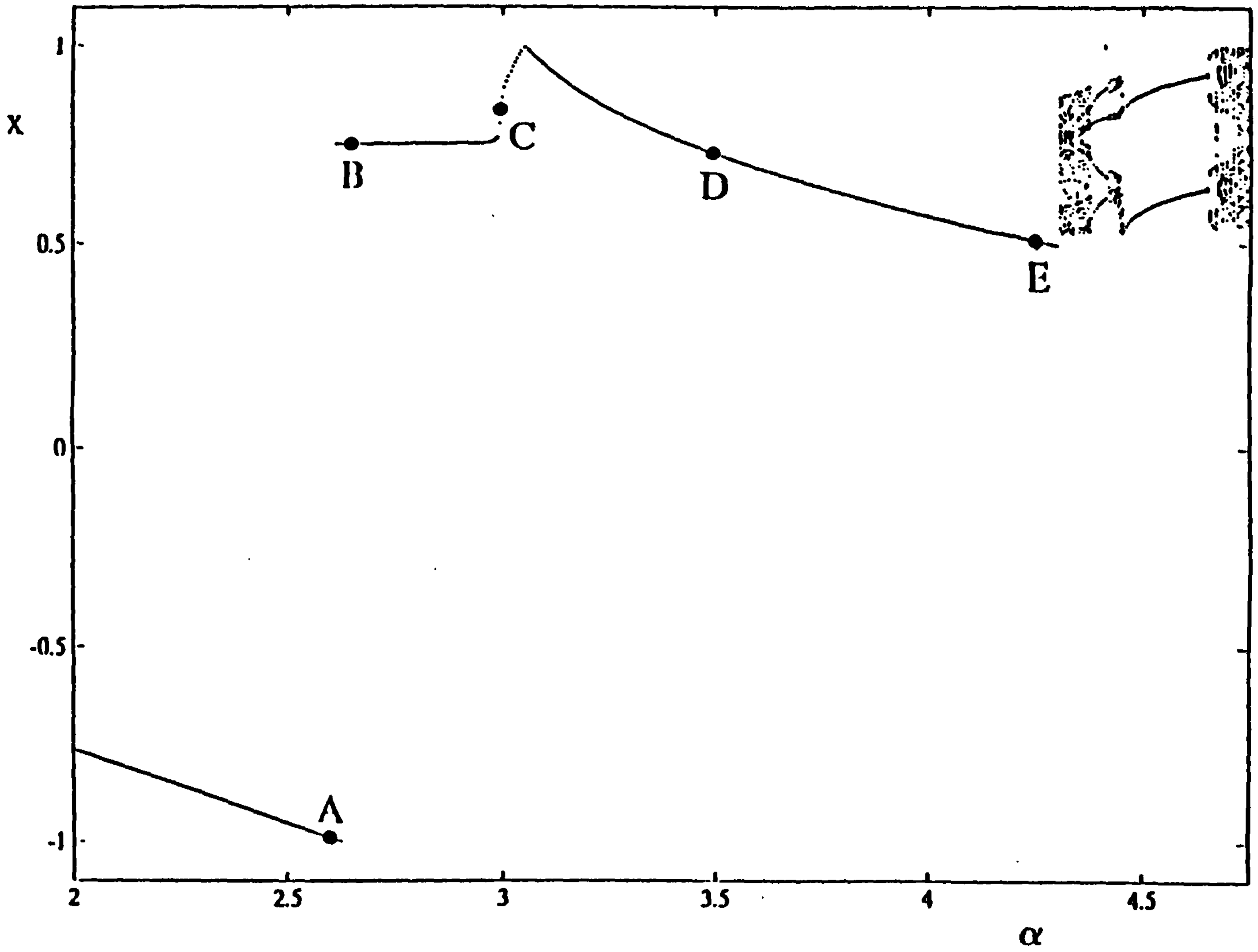

Figure 3.4 Bifurcation diagram showing the displacement, x, in the stroboscopic Poincaré map against the forcing amplitude value α from equation 3.7. Points A-E are marked corresponding to the orbits in figure 3.3.

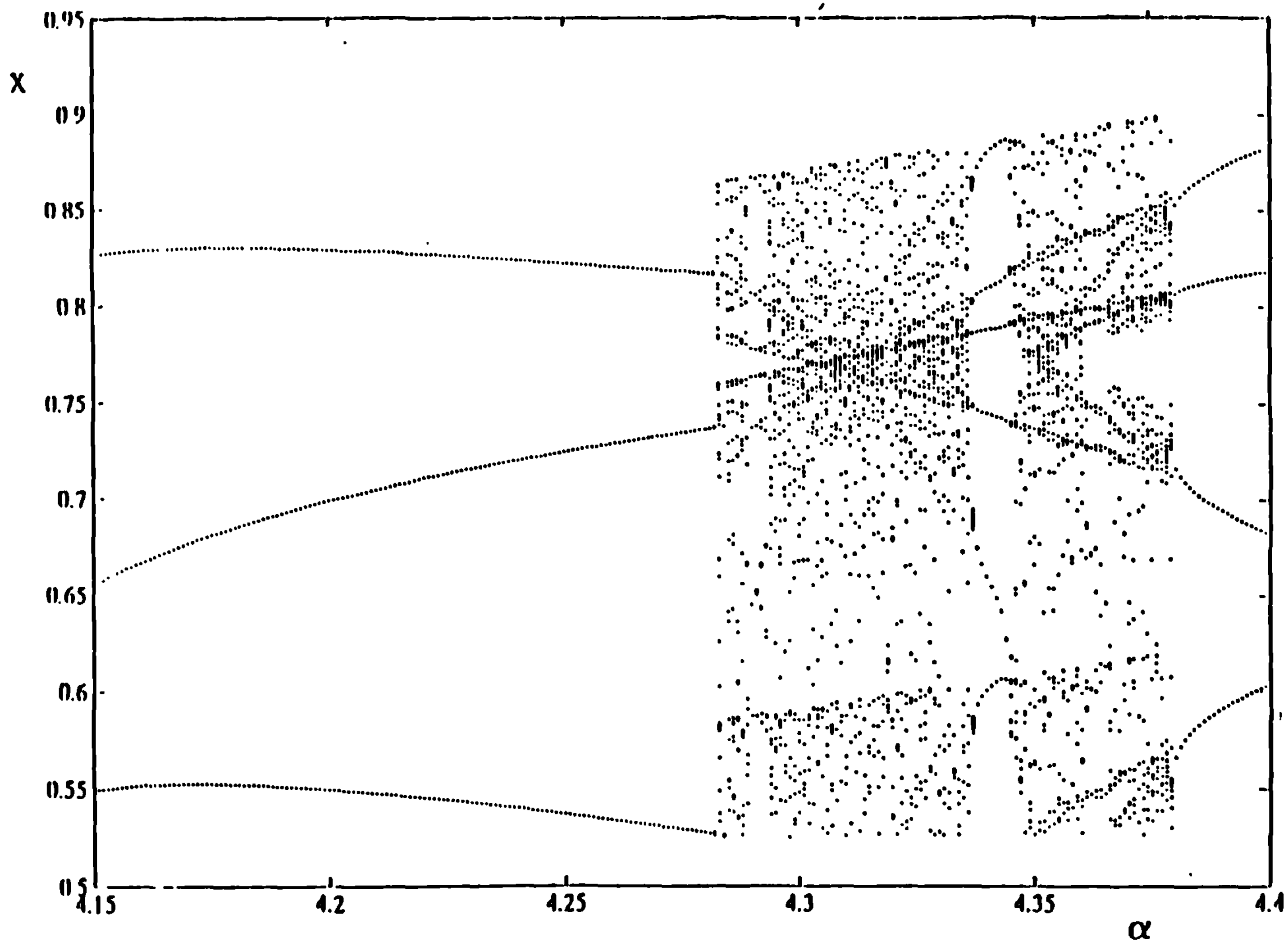

Figure 3.5 Enlargement of the area around $\alpha = 4.3$ in the bifurcation diagram 3.4.

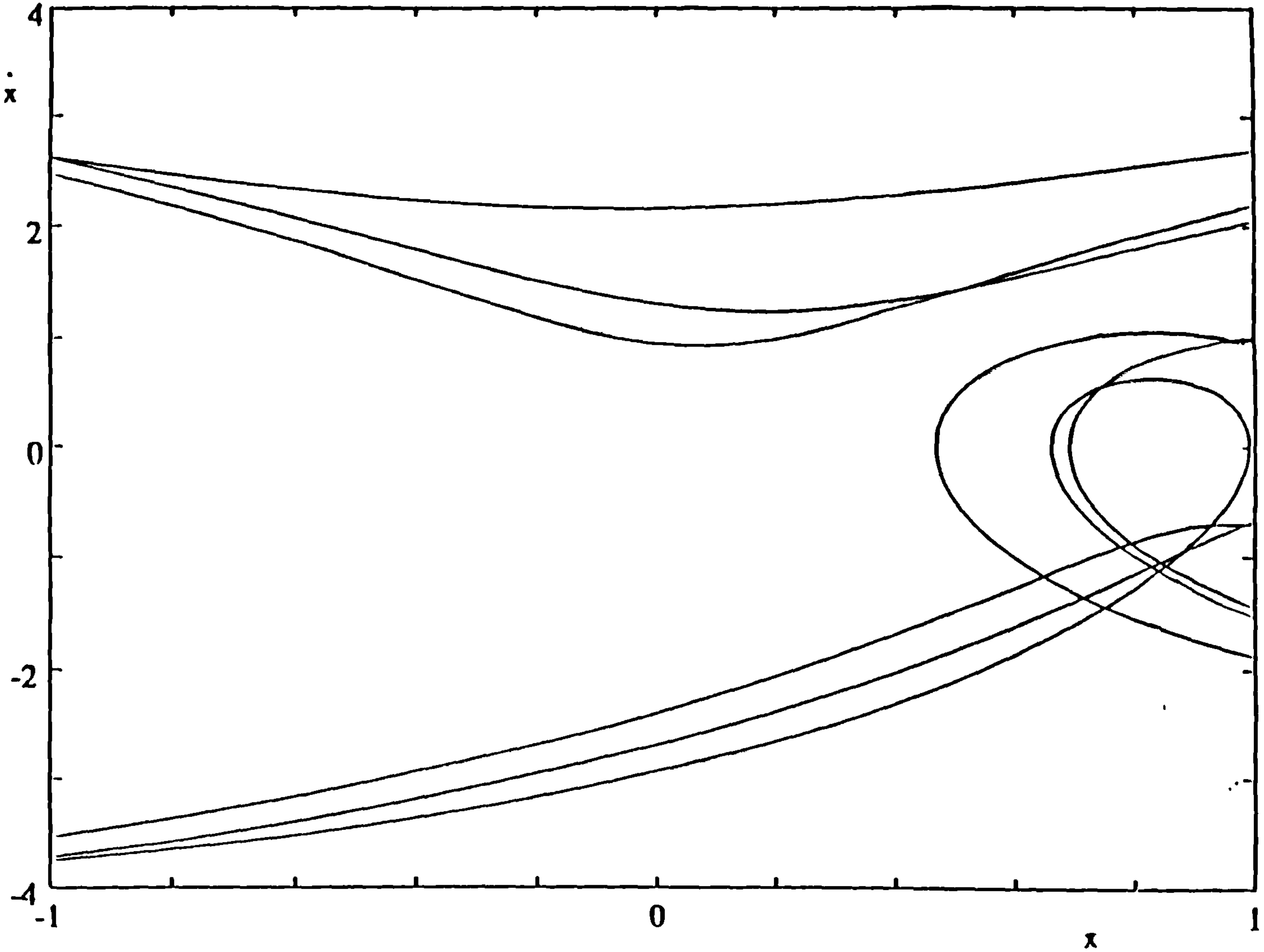

Figure 3.6 Phase plane projection $\dot{x}$ against x, of the period three orbit at α=4.25 in equation 3.7.

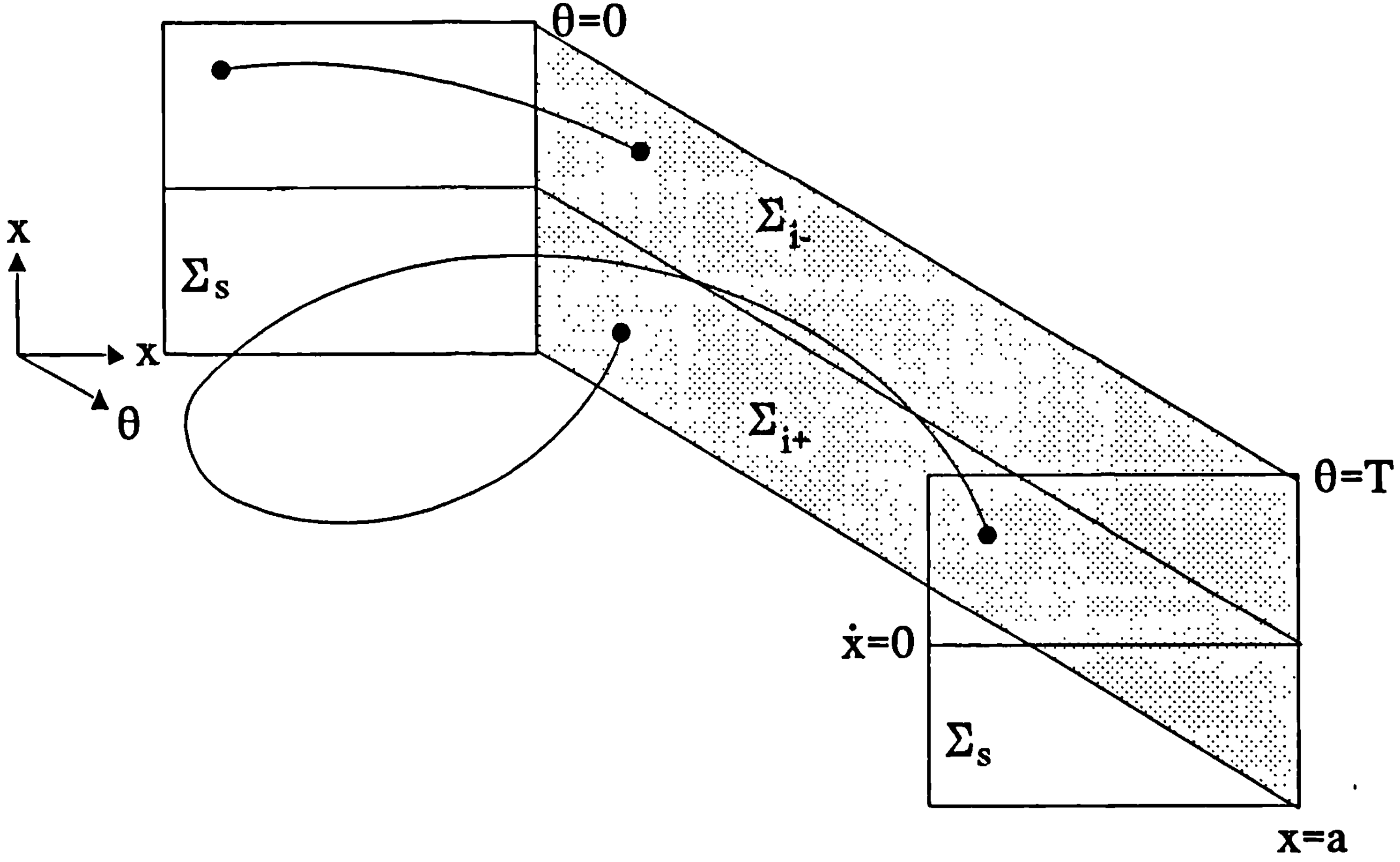

Figure 3.7 The phase space for the one sided impact oscillator given by equations 3.1 and 3.2. The shaded area represents the stop. A period one orbit is depicted which starts at $\theta=0$ in Σ_s then impacts at Σ_{i-}, is reflected by the coefficient of restitution rule to Σ_{i+} and then continues until $\theta=T$ ($=2\pi/\omega$), back at Σ_s .

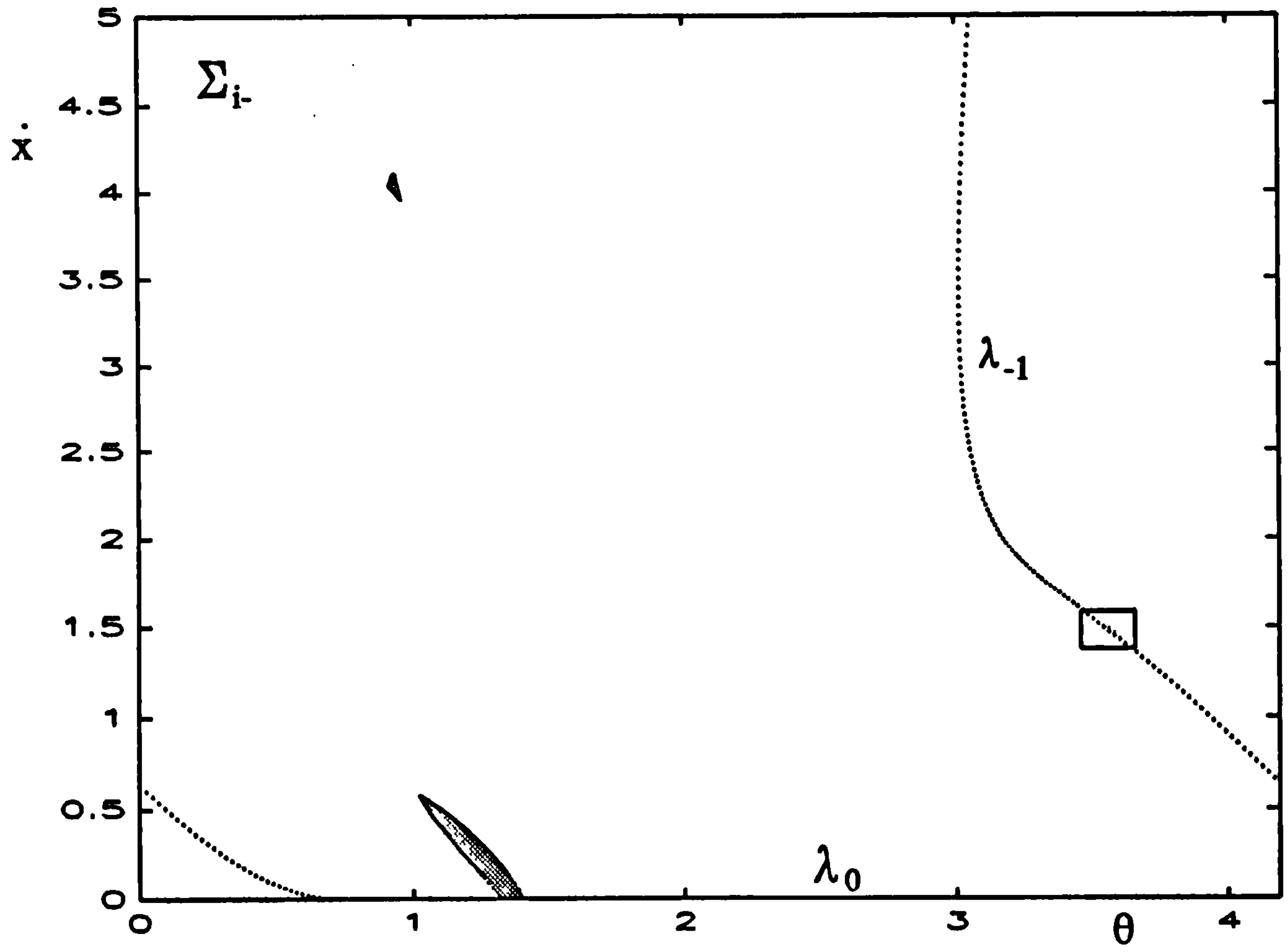

Figure 3.8 Discontinuity in P_{i-} . A portion of Σ_{i-} is shown, with a rectangular area lying over the line γ_{-1} . The image of the rectangle is shown shaded, one part bordering the stop and the other part (corresponding to those orbits which just miss the stop) around $(x,x)=(1,4)$.

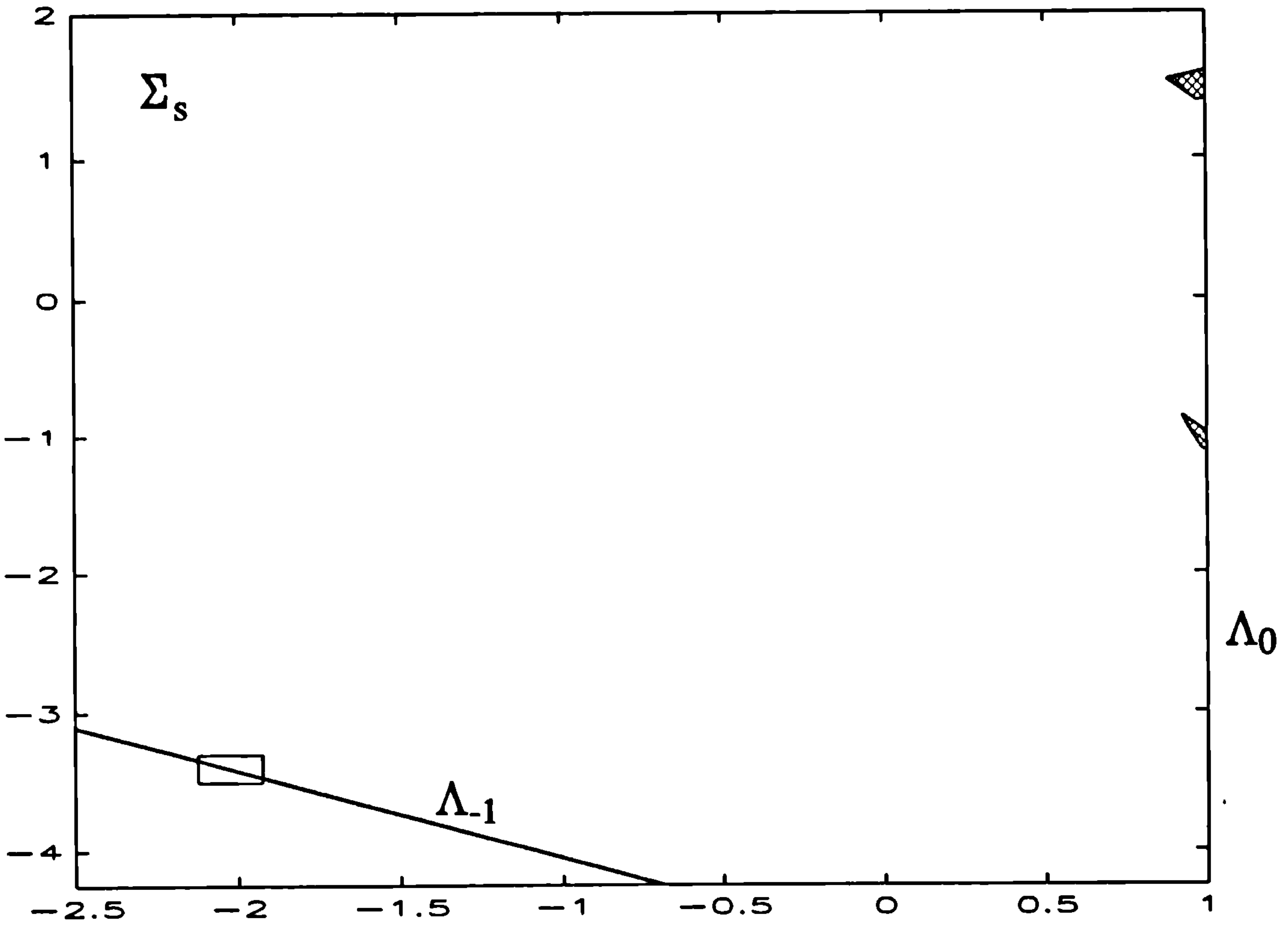

Figure 3.9 Discontinuity in P_s . A portion of Σ_s is shown, with the a rectangular area lying over the line Λ_{-1} . The image of the rectangle is shown shaded, one part bordering the stop $\Lambda_{-1}$with positive velocity and one with negative velocity.

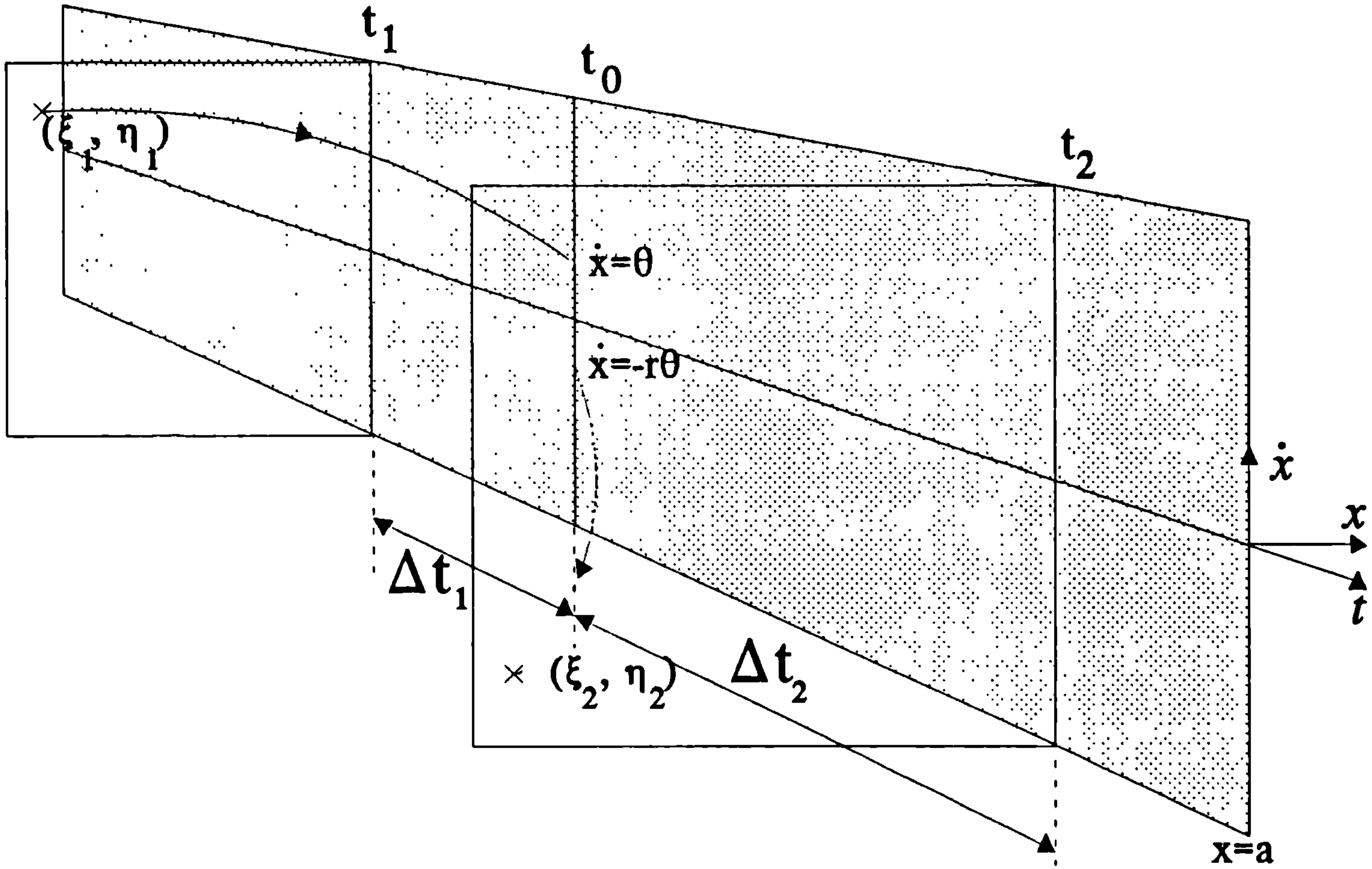

Figure 3.10 Taylor expansion backwards and forwards from a low velocity impact. An impact osccurs at $x=\theta$, $t=t$. Thr orbit shown intersects with the plane $t=t$ at (ξ_1,η_1) and the plane $t=t$ at (ξ_2,η_2).

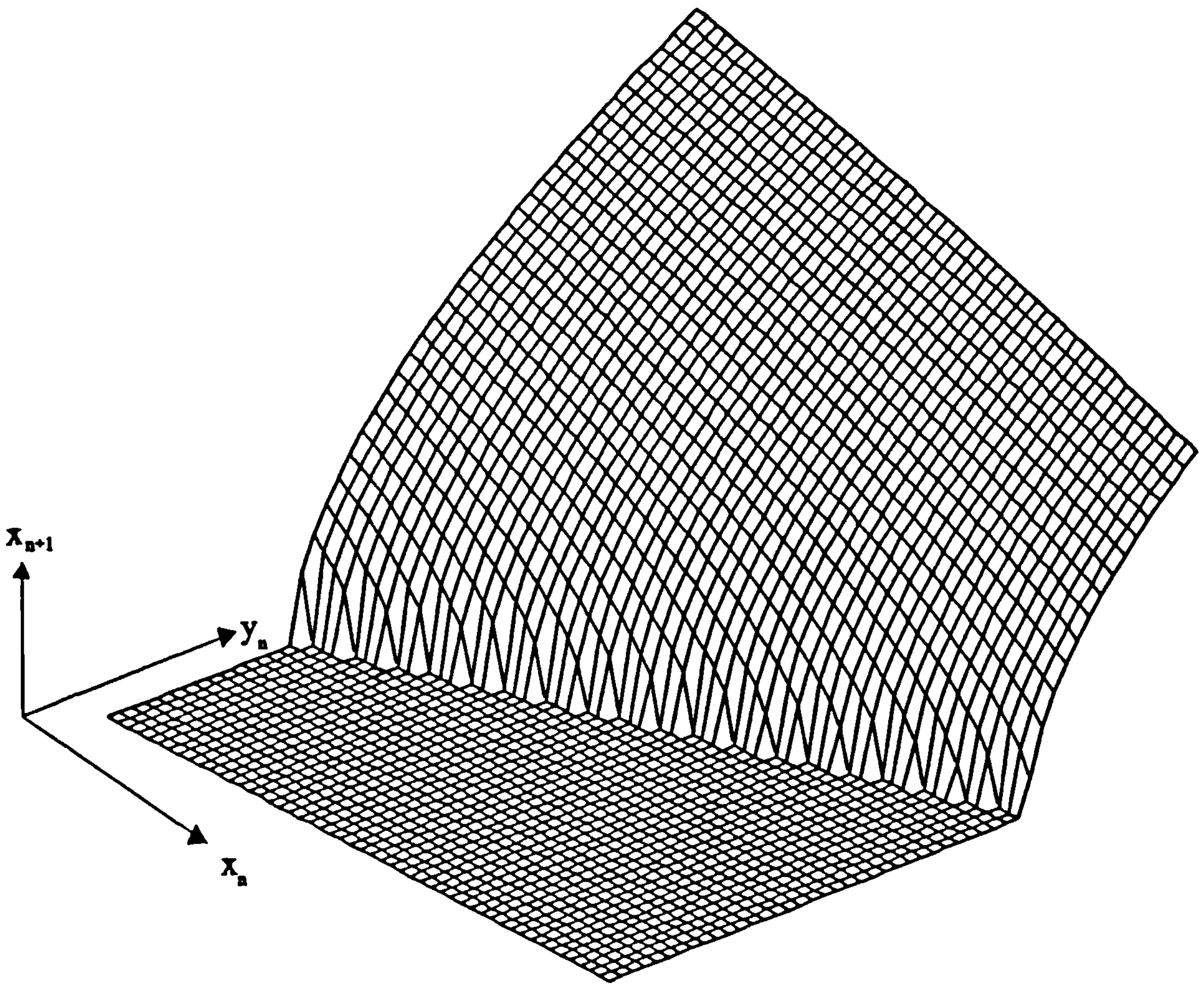

Figure 3.11 The square root singularity in gradient of a stroboscopic map from an impact oscillator. Shown is the x coordinate of the image over the original rectangular area. The line of discontinuity of gradient is clearly seen.

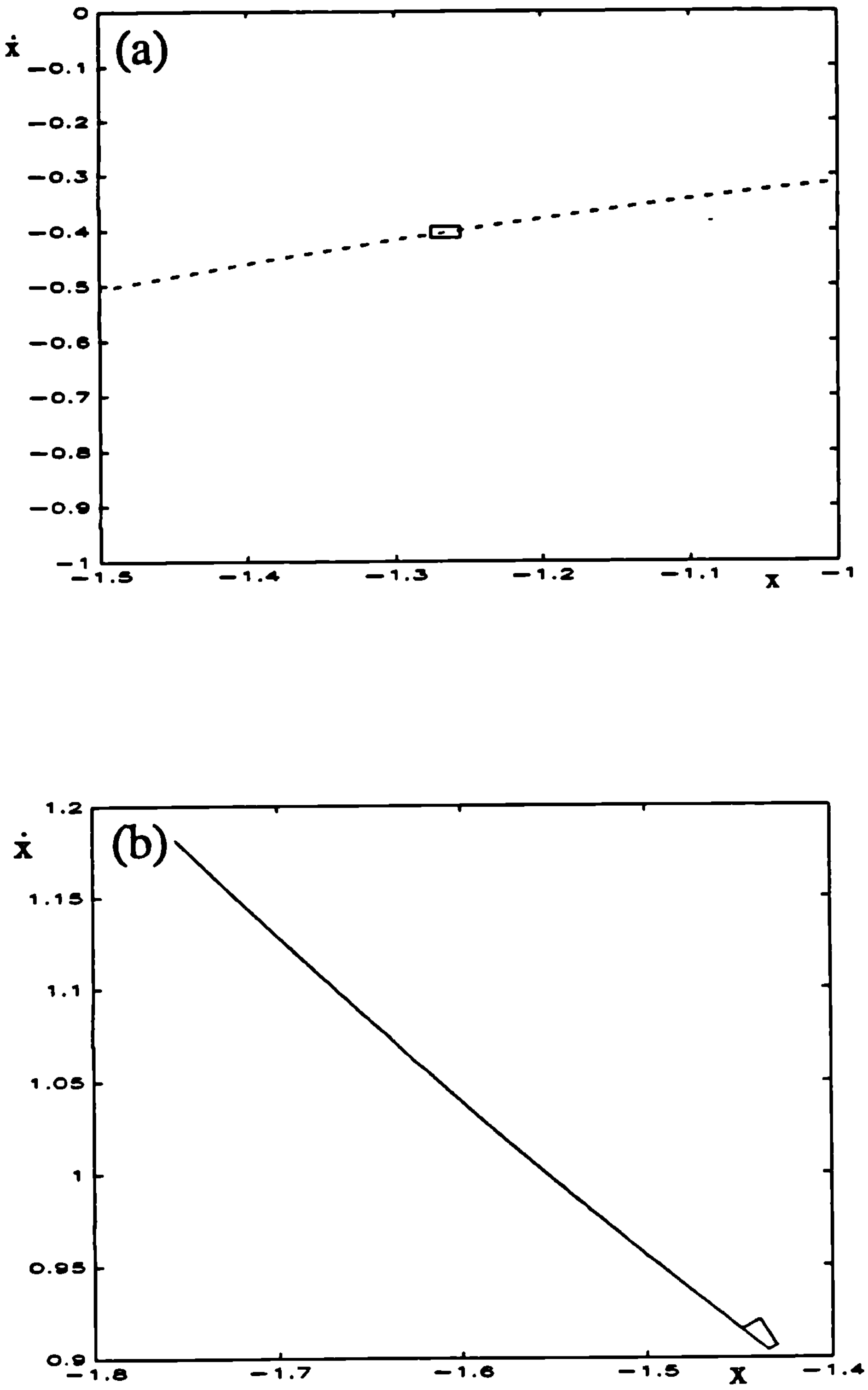

Figure 3.12 (a) The small rectangle from figure 3.11 lying over a line of discontinuity of gradient in the stroboscoopic section and (b) its image under one iteration of the map P_s .

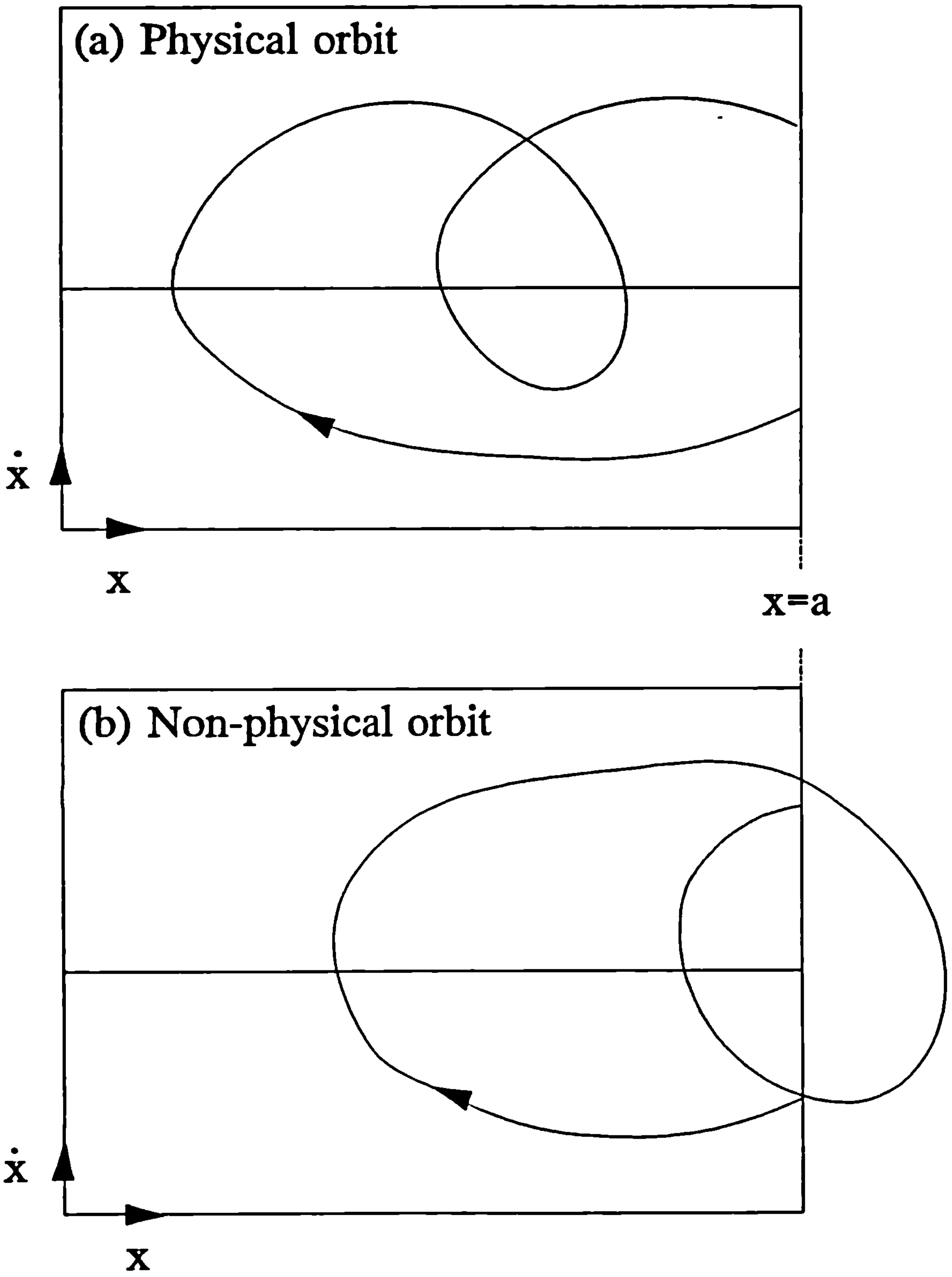

Figure 3.13 Physical and non-physical orbits. The non-physical orbit shown in (b) to penetrates the stop before repeating.

4. Bifurcations in impact oscillators

4.1 Bifurcations in the COR model

4.1.1 Bifurcations of period one, one impact solutions

The one sided COR impact oscillator given by equations 3.1 & 3.2 together, as well as undergoing conventional, smooth bifurcations (flips and saddle nodes), see for example Shaw & Holmes [1983], can undergo bifurcations due to low velocity impacts, called grazing bifurcations. We also note here that equation 3.1 is dissipative (if the damping, $d>0$), as is the impact rule equation 3.2, and so any Poincaré map which we obtain from the COR impact oscillator will have an overall area contraction. This implies that no Neimark bifurcation can occur, since this would require both eigenvalues of the two dimensional map to lie on the unit circle at bifurcation, which would require there to be no area contraction. Nordmark [1991], Whiston [1992], Foale & Bishop [1992] and Budd et al [1993] have all investigated various aspects of the effect of low velocity impacts on COR impact oscillators. In this chapter the analytical solutions available (see chapter 3) are used to try to relate grazing bifurcations to conventional, smooth bifurcations. As discussed in section 3.6 there are discontinuities in gradient in any Poincaré map from an impact oscillator along lines of grazing points. When a fixed point crosses a line of grazing points under the change of a system parameter then a grazing bifurcation occurs. In this section we look at the simplest case of a grazing bifurcation in the one sided, linear COR impact oscillator 3.1 & 3.2, where a non-impacting period one stable steady state solution, under a change in parameter just starts to hit the stop with low velocity.

4.1.2 Locus of *first grazing* bifurcations

Non-impacting steady state solutions of 3.1, where they exist, just consist of the 'particular integral' part of the general solution 3.21 and 3.22, after the transients have exponentially decayed away. We form a discrete time dynamical system from the continuous time one in the usual way, by taking a surface of section Σ and defining the Poincaré map P which takes points in Σ back onto itself. In this case it is most convenient to use the stroboscopic Poincaré section where x and $\dot{x}$ are sampled at a given phase of the forcing function, $\phi = t \bmod 2\pi/\omega = 0$. Fixed points of this map corresponding to non-impacting periodic steady state solutions are easily seen from 3.21 and 3.22 to be given by $x_n=-\alpha\ cos(\phi)/\gamma$, $\dot{x}_n=\alpha\omega\ sin(\phi)/\gamma$ and the first differential matrix of this mapping is obtained by differentiating the equations 3.21 and 3.22 with respect to x_i and $\dot{x}_i$ and evaluating at time $t=2\pi/\omega$ giving

$$DP = \begin{bmatrix} \nu\left[c_w + \frac{\beta s_w}{\Omega}\right] & \frac{\nu s_w}{\Omega} \\ -\frac{\nu s_w}{\Omega} & \nu\left[c_w - \frac{\beta s_w}{\Omega}\right] \end{bmatrix} \qquad 4.1$$

The eigenvalues of the mapping P can then be calculated to be $\lambda_{1,2}=\nu(-c_w \pm s_w)$. We can see that the maximum displacement x of the non impacting solution is α/γ, so at when $\alpha/\gamma<a$ the steady state, non-impacting orbit does exist. At a critical, grazing value of α, $\alpha_c=a\gamma$, the non-impacting orbit will just graze the stop at $x=a$ with zero velocity. As α is increased past α_c this stable orbit, or the stable fixed point of the stroboscopic map, can no longer exist. It disappears at a grazing bifurcation. The locus of these grazing bifurcations is given then by

$$\alpha_c = a\gamma = a\sqrt{(d\omega)^2+(\omega^2-1)^2} \qquad 4.2$$

4.1.3 Types of grazing bifurcation

In section 1.3.2 we looked at the behaviour of a continuous, piecewise linear map consisting of two 2-dimensional linear maps, one with a large direction of expansion. We assumed that the coordinates had been transformed so that the line of discontinuity of gradient, where the two linear maps join, lies along the coordinate direction separating the left and right half planes. This piecewise linear map was parameterised by μ in such a way that a stable period one fixed point exists in the left hand half plane when $\mu \leq 0$, and lies along the line of discontinuity in gradient when $\mu=0$. The mapping in the right hand half plane has one large direction of expansion, i.e. one eigenvalue with a large absolute value, λ_1 say. We required that both linear mappings were orientation preserving and dissipative, so that there is a corresponding small eigenvalue, λ_2 of the same sign such that $0<\lambda_1\lambda_2<1$. It was shown that if $\lambda_1>0$ then another (unstable) period one solution exists for $\mu \leq 0$. If $\lambda_l < 0$ then an unstable period one orbit was shown to exist for $\mu \geq 0$.

A stroboscopic Poincaré map from a one degree of freedom COR impact oscillator was shown in section 3.6 to have lines along which the map is continuous but discontinuous in gradient, with a square root singularity on one side of the line. We again assume that we have transformed coordinates such that the line of discontinuity of gradient lies along the coordinate direction separating the left and right half planes and that the system is parameterised by μ such that for $\mu \leq 0$ there is a stable, period one fixed point in the left hand half plane. For any particular parameter μ close to zero, we can replace the map on the right hand side with an equivalent linear map. By this we mean that there is a linear map with an identical period one fixed point, if any, as the map with square root singularity, i.e. the fixed point has the same position, same eigenvalues. We then have an equivalent piecewise linear system which has one large direction of expansion, and the result described above shows the bifurcational behaviour we can expect from such a system. If the eigenvalue corresponding to the direction of large expansion is positive, there will be two period one fixed points (stable and unstable) for $\mu < 0$. If the eigenvalue corresponding to the direction of large expansion is negative, there will be a stable fixed point for $\mu < 0$ and an unstable fixed point for $\mu > 0$.

In summary, we expect to find two distinct types of grazing bifurcation in a two degree of freedom COR impact oscillator. In both cases an unstable periodic orbit of the same period continues on from the stable periodic orbit after grazing, either from below or above. In the next section we use analytical solutions to show that this is the case for the most simple grazing bifurcations.

4.1.3.1 One sided impact oscillator

We have discussed above how the simple, non-impacting stable solution reaches a critical point at which the amplitude of the solution is such that part of the orbit is just grazing the stop with zero velocity. In order to form a continuous solution path, a period one solution with one low amplitude impact per period must continue on from the end of this stable path. In order to see that this is so we look again at the analytical solutions for period one, one impact per period solutions of 3.1.

Take equation 3.32, and by further noting that the parameter α only occurs in l_1,l_2,l_3,m_1,m_2,m_3 linearly (if at all) we can define new quantities L_1,L_2,L_3,M_1,M_2,M_3 all independent of α.

$$\alpha L_1 = l_1 \ , \ \alpha L_2 = l_2 \ , \ L_3 = l_3 \ , \ \alpha M_1 = m_1 \ , \ \alpha M_2 = m_2 \ , \ M_3 = m_3 \qquad 4.3$$

3.32 can then be rearranged to give

$$\alpha^2 = \alpha_c^2 + 2\alpha_c r y_i \frac{\frac{M_2}{M_1}}{\frac{M_2}{M_1}L_1 - L_2} + r^2 \frac{y_i^2}{\left[\frac{M_2}{M_1}L_1 - L_2\right]^2}\left[1 + \left[\frac{M_2}{M_1}\right]^2\right] \qquad 4.4$$

From equation 4.4 we can see that near grazing, when $0<y_i \ll 1$ then $\alpha \to \alpha_c$ from above or below depending on the sign of the coefficient of the linear term of this quadratic in y_i. Since $r, y_i, \alpha_c > 0$ we have that the sign of z where

$$z = \frac{\frac{M_2}{M_1}}{\frac{M_2}{M_1}L_1 - L_2} \qquad 4.5$$

controls the type of grazing bifurcation. There are two distinct types of grazing bifurcation depending on whether z is positive or negative : the two cases are sketched in figure 4.1, where the maximum amplitude of the period one solutions are plotted against the forcing amplitude α with all other parameters fixed. In both cases when $\alpha<\alpha_c$ there is a stable non-impacting period one solution whose amplitude grows linearly with α (the solid lines). The stability characteristics of this non-impacting solution do not change as α changes as can be seen from equation 4.1 (c_w and s_w are functions of ω and d and the other terms in 4.1 are functions only of d). In figure 4.1a, with $z<0$, as the velocity of the period one, one impact solution $y_i \to 0$, $\alpha \to \alpha_c$ from below, with $\alpha=\alpha_c$ when $y_i=0$. Since the velocity at impact, y_i, is very small then we can see from 3.44 and 3.45 that this solution is very unstable, with one eigenvalue tending to infinity as $\alpha \to \alpha_c$. In figure 4.1b, with $z>0$, as the velocity of the period one, one impact solution $y_i \to 0$, $\alpha \to \alpha_c$ from above, with $\alpha=\alpha_c$ when $y_i=0$. Again the velocity at impact, y_i, is very small and so this solution is very unstable, with one eigenvalue tending to infinity as $\alpha \to \alpha_c$. These unstable solutions are represented by dotted lines in figure 4.1.

On examining the expression for z (using the parameters d=0.1, r=0.7, a=1.0 in equations 3.1 and 3.2) we see that $z=0$ when $s_w=\sin(2\pi\Omega/\omega)=0$, i.e. when $\omega=2\Omega/n$ for $n=1,2,\ldots$ These are the values of ω where the function z changes sign, see figure 4.2.

4.1.3.2 Two sided symmetric impact oscillator

A similar analysis can be carried out for bifurcations from the non-impacting stable steady state solutions of the two sided impact oscillator, equation 3.33, to symmetric, period one steady state solutions with one impact at each stop in one period. We note that we can rewrite $p_1=\alpha P_1, p_2=\alpha P_2, p_3=P_3$ and $q_1=\alpha Q_1, q_2=\alpha Q_2, q_3=Q_3$, where P_1,P_2,P_3,Q_1,Q_2,Q_3 are all independent of α. Then equations 3.31, 3.32 and thus 4.4 can be rewritten by changing L_1,L_2,L_3,M_1,M_2,M_3 to P_1,P_2,P_3,Q_1,Q_2,Q_3 respectively, giving

$$\alpha^2 = \alpha_c^2 + 2\alpha_c r y_i \frac{\frac{Q_2}{Q_1}}{\frac{Q_2}{Q_1}R_1 - R_2} + r^2 \frac{y_i^2}{\left[\frac{Q_2}{Q_1}R_1 - R_2\right]^2}\left[1 + \left[\frac{Q_2}{Q_1}\right]^2\right] \qquad 4.6$$

Since the expression 4.2 for the critical first grazing value $\alpha=\alpha_c$ is the same as for the one sided case we can interpret the quadratic equation 4.6 in the same way as before.

The coefficient of the linear term in y_i again controls the type of grazing bifurcation, this time between stable non-impacting period one solutions and unstable period one symmetric, one impact per stop solutions. We have that the sign of z' where

$$z' = \frac{\dfrac{Q_2}{Q_1}}{\dfrac{Q_2}{Q_1}R_1 - R_2} \qquad 4.7$$

controls the type of grazing bifurcation. When $z'<0$ then $\alpha \to \alpha_c$ from above and when $z'>0$ then $\alpha \to \alpha_c$ from below. On examining the expression 4.7 for z' we see that $z'=0$ when $s_w = sin(\pi\Omega/\omega)=0$, i.e. when $\omega=\Omega/n$ for $n=1,2,...$ These are the values of ω where the function of z' changes sign, and therefore where the type of grazing bifurcation changes, see figure 4.3 (the parameters used here are d=0.1, r=0.7, a=1.0).

4.1.4 Illustrations of grazing bifurcations

Using the methods described in sections 3.71 and 3.72 we are able to analytically locate steady state period one solutions of the system given by equations 3.1 & 3.2, both for the case of non-impacting and one impact per period solutions. We must always numerically ensure that the one impact per period orbits are physically possible (see section 3.72 and figure 3.13). The stability analyses in sections 3.74 and 4.1.2 allow us to monitor the stability of the periodic orbits found analytically in this way. Using these methods we semi-analytically, semi-numerically obtain the amplitude-response figures 4.4 & 4.5, where the maximum absolute displacement $max(x)$ is plotted against α. Here, all parameters are kept fixed ($d=0.1$, $r=0.7$, $a=1.0$, $\omega=1.8$ & 2.2) except the amplitude of the forcing α : solid lines denote stable solutions and dotted lines unstable solutions. The two cases are taken at constant values of the forcing frequency, ω, either side of the largest value of ω at which the function z (equation 4.5) changes sign, $\omega=2\Omega\approx 1.9975$, and illustrate the two types of grazing bifurcation described in section 4.1.3.

Case 1 : $\omega = 1.8$, figure 4.4

As α is increased up to the critical, first grazing value $\alpha_c \approx 2.247$ there exists a linearly increasing path of the stable non-impacting period one solution. This solution must disappear at grazing. Since the function z here is less than zero, it was shown in section 4.1.3.1 that a period one, one impact per period solution approaches the first grazing parameter value α_c from below, and since the velocity at impact is tending to zero an eigenvalue of the impacting solution is tending to infinity as grazing is approached. We see then a grazing bifurcation in figure 4.4 at G where a stable and unstable solution meet and disappear together. As the path continues there is a saddle-node bifurcation at SN. Although there are similarities between the two bifurcations G and SN since in both cases stable and unstable solutions meet and annihilate one another, they are quite different. At SN the stability characteristics of the two orbits change smoothly, with an eigenvalue of the jacobian of P_s tending to $+1$ from above and below. At G the stability characteristics of the stable solution do not change up to grazing, but an eigenvalue of the unstable solution tends to infinity as grazing is approached.

Case 2 : $\omega = 2.2$, figure 4.5

Again, as α is increased up to the critical, first grazing value $\alpha_c \approx 3.846$ there exists a linearly increasing path of the stable non-impacting period one solution. The function z here is greater than zero, so the period one, one impact per period solution approaches the first grazing parameter value α_c from above. Again, since the velocity at impact is tending to zero as $\alpha \to \alpha_c$ from above, an eigenvalue of the impacting period one solution tends to infinity as the grazing bifurcation G is approached. In this case, as the path continues, there is a flip bifurcation at F.

4.1.5 Bifurcation loci of smooth and grazing bifurcations

In section 4.1 equation 4.2 was derived which gives the locus of first grazing bifurcations in terms of the system parameters. If we fix all parameters as in section 4.1.4 then as the forcing frequency ω varies the first grazing occurs at α_c, the thick solid curve in figure 4.6. Using the analytical expression for the eigenvalues of the period one, one impact solution, equation 3.45, we can numerically compute the loci of flip bifurcations, where an eigenvalue equals -1 and saddle-node bifurcations where an eigenvalue equals +1. Figure 4.6 shows the locus of flip bifurcations as a thin solid line and the locus of saddle-node bifurcations as a chain dotted line. Below $\omega=0.5$ there are further alternating flip and saddle node bifurcations, but the loci of these bifurcations have not been computed here. It appears that the flip and saddle node loci meet at the values of ω where the function z passes through zero (equation 4.1.6, figure 4.2) and the type of grazing bifurcation changes. Again we show that this is the case in section 4.1.6.

4.1.6 Co-dimension two bifurcations

It appears in the bifurcation locus diagram 4.6 that when the type of grazing bifurcation changes, i.e. when the sign of z changes, then a line of saddle node bifurcations and a line of flip bifurcations meet at this point. We now demonstrate that this is indeed the case. Let $2\pi\Omega/\omega=\pi+\epsilon$. Then $s_w=-sin(\epsilon)$, $c_w=-cos(\epsilon)$. If we substitute these expressions into the equation 3.44, using equations 3.31 for s_i and c_i as well, we have an expression for $tr(D)$ in ϵ. Expanding this in powers of the small variable ϵ we have

$$tr(D) \;=\; 2\nu r \;+\; \frac{a\nu\omega^2(1+r)}{\Omega}\frac{\epsilon}{y_i} \;+\; \frac{2\beta\nu(1+r)(\nu r-1)}{\Omega(\nu+1)}\epsilon \;+\; O(\epsilon^2) \qquad 4.8$$

The small variable ϵ depends on the driving frequency ω, not on the amplitude of the forcing α, and so however small ϵ is, we can choose α close enough to α_c such that y_i is as small as we like, and so ϵ/y_i is of $O(1)$ or greater. Any term in ϵ can therefore be ignored as small.

The condition which must be satisfied for a saddle-node bifurcation is

$$det(D) - tr(D) + 1 \;=\; 0 \qquad 4.9$$

and for a flip bifurcation

$$det(D) + tr(D) + 1 \;=\; 0 \qquad 4.10$$

so we define $sn=det(D)-tr(D)+1$ and $pd=det(D)+tr(D)+1$. Using equation 4.8 for $tr(D)$ gives

$$sn = (r\nu - 1)^2 - K\frac{\epsilon}{y_i} + \ldots \tag{4.11}$$

$$pd = (r\nu + 1)^2 + K\frac{\epsilon}{y_i} + \ldots \tag{4.12}$$

where

$$K = \frac{a\nu\omega^2(1+r)}{\Omega} > 0 \tag{4.13}$$

The condition 4.11 for a saddle-node bifurcation, $sn=0$, then gives

$$sn=0 \Rightarrow y_i = \frac{K\epsilon}{(r\nu-1)^2} + \ldots \tag{4.14}$$

The velocity at impact of the steady state, period one, one impact solution, y_i must be positive, and this can only be so if $\epsilon>0$ in 4.14. Thus we conclude that when ϵ is small and positive (i.e. $\omega<2\Omega$) there is a period one, one impact steady state solution with velocity at impact given by 4.14 which is undergoing a saddle-node bifurcation. For a given small positive ϵ the parameter α_{sn} at which this bifurcation occurs can be obtained from 4.4. Since $\omega<2\Omega$ the variable z which controls the type of grazing bifurcation nearby is negative, so $\alpha_{sn}<\alpha_c$ and $\alpha_{sn}\rightarrow\alpha_c$ as $\epsilon\rightarrow 0$, i.e. as $\omega\rightarrow 2\Omega$ from below. The amplitude of forcing α at which the saddle-node bifurcation occurs can be seen from 4.4 to be

$$\alpha_{sn} = \sqrt{\alpha_c^2 + \frac{2\alpha_c rzK}{(r\nu-1)^2}\epsilon + \ldots} \tag{4.15}$$

Similarly, the condition 4.10 for a flip bifurcation, $pd=0$, gives

$$pd = 0 \Rightarrow y_i = -\frac{K\epsilon}{(r\nu+1)^2} + \ldots \tag{4.16}$$

Again, we must have that y_i is positive, and this can only be so if $\epsilon<0$ in 4.16. Thus we conclude that when ϵ is small and negative (i.e. $\omega>2\Omega$) there is a period one, one impact steady state solution with velocity at impact given by 4.16 which is undergoing a flip bifurcation. For a given small negative ϵ the parameter α_{pd} at which this bifurcation occurs can be obtained from 4.4. Since $\omega>2\Omega$ the variable z which controls the type of grazing bifurcation nearby is positive, so $\alpha_{pd} > \alpha_c$ and $\alpha_{pd} \rightarrow \alpha_c$ as $\epsilon \rightarrow 0$, i.e. as $\omega \rightarrow 2\Omega$ from above. The amplitude of forcing α at which the flip bifurcation occurs can be seen from 4.4 to be

$$\alpha_{pd} = \sqrt{\alpha_c^2 + \frac{2\alpha_c rzK}{(r\nu + 1)^2}\epsilon + \ldots} \qquad 4.17$$

4.2 Bifurcations in the Hertz law model

4.2.1 Bifurcations of period one, one impact solutions

In the previous sections the analytical solutions available for the one sided COR impact oscillator were used to investigate the bifurcational behaviour of this model. An important set of bifurcational events were found to occur when an orbit undergoes a low velocity impact at the stop, a grazing bifurcation. In particular, the simplest grazing bifurcation, the first grazing, when a stable non-impacting orbit just starts to hit the stop with low velocity, was investigated. It was shown that two types of grazing bifurcation occurred : as the amplitude of the forcing is increased towards the first grazing, an unstable solution with low velocity impacts approaches the stable non-impacting solution either from above or below. Examples of these grazing bifurcations were shown in figures 4.4 and 4.5. If the Hertz law model (equations 3.1 and 3.3) and the COR model both model the impact process reasonably well then we should expect the bifurcational behaviour of the two models to be similar. Since the Hertz law model is continuous and differentiable it does not suffer the same problems as the COR model : there is no discontinuity in gradient and therefore grazing bifurcations cannot occur. Using the same parameters as were used in the illustrations of grazing bifurcations 4.4, 4.5, and $k=2000$, a path following algorithm (see chapter 2) was used to locate and follow fixed points of the stroboscopic Poincaré map of the Hertz law model as the amplitude of the forcing α changes. The eigenvalues of the Jacobian matrix of this map were also monitored in order to locate changes in stability (bifurcations) along the path. When a period one fixed point was located, the equations were further integrated over a period in order to find the maximum absolute displacement *max(x)* of the periodic orbit.

Case 1 : $\omega=1.8$, figure 4.7 (cf. figure 4.4)

Just after the non-impacting orbit starts to hit the stop at $\alpha_c \approx 2.247$ we observe a saddle-node bifurcation SN (an eigenvalue of the Jacobian matrix of the stroboscopic Poincaré map leaves the unit circle at +1). An unstable impacting orbit meets and annihilates the stable orbit. As the path continues there is a further saddle-node bifurcation SN. Comparing this figure to the COR model, figure

4.4, it can be seen that there are great similarities. Although in the COR model, as the non-impacting orbit just grazes the stop, there is a grazing bifurcation **G** as opposed to the conventional saddle-node bifurcation **SN** in the Hertz law model, an unstable low velocity impacting orbit meets and annihilates the stable non-impacting orbit.

Case 2 : $\omega=2.2$, figure 4.8 (cf. figure 4.5)
In this case, just after the non-impacting orbit starts to hit the stop at $\alpha_c \approx 3.846$ there is a flip bifurcation at **F** (an eigenvalue of the Jacobian matrix of the stroboscopic Poincaré map leaves the unit circle at -1), with an unstable, impacting period one orbit continuing on from the stable non-impacting one. As the path continues there is a further flip bifurcation. Comparing this figure to the COR model, figure 4.5, again there are great similarities. Instead of a grazing bifurcation **G** in the COR model just after the first grazing there is a flip bifurcation **F** in the Hertz law model, but in both cases an impacting unstable low velocity orbit continues on from the stable non-impacting orbit.

4.2.2 Bifurcation loci for the Hertz law model

In figures 4.4 & 4.7 and 4.5 & 4.8 a strong similarity between the paths of solutions of the Hertz law impact oscillator and the COR model was numerically demonstrated. For figure 4.9, showing the bifurcation loci for the Hertz law model at the parameter set used above, we again use numerical path following methods to follow the loci of flip and saddle-node bifurcations in the space of the two parameters α and ω, near to the largest forcing frequency $\omega \approx 1.9975$ at which the grazing bifurcation type in the COR model changes as the function z (equation 4.2) passes through zero. Figure 4.6 shows the equivalent bifurcation loci for the COR model, where a saddle-node and flip bifurcation also meet at this point. In the Hertz law model there are no grazing bifurcations, but near to where there is a line of grazing bifurcations in the COR model there is a line of either flip or saddle-node bifurcations in the Hertz law model. Both the locus of flip bifurcations and saddle-node bifurcations ends at a cusp near to the location of the codimension two event in the COR model in which a flip and saddle-node bifurcation loci meet along the grazing bifurcation locus at the same point as the type of grazing bifurcation changes. The degenerate codimension two event in the COR model appears to have split into two generic codimension two events (cusps).

4.2.3 Attractor following through bifurcations

Figures 4.5 and 4.8 show the paths of the stable and unstable solutions of the COR and Hertz law impact oscillators which correspond to the stable non-impacting low amplitude solution and the unstable low velocity impact solutions which continue on from it. If instead of trying to locate the unstable solutions we simply allow the system to evolve slowly as the amplitude increases we will follow the stable non-impacting solution up to bifurcation, where the system will lose its stability and restabilise onto a different attracting solution. Figure 4.10 and 4.11 show the comparison between the two models at the parameter settings used in figures 4.5 and 4.8 (ω=2.2). Here there is a flip bifurcation in the Hertz law model at a forcing amplitude just greater than the critical amplitude at which the first impacts start to occur. This flip bifurcation is the start of a period doubling cascade. Figure 4.11 appears to show an immediate jump to a period 4 solution, but if we look more closely at the region where the period four solution begins we indeed see a period two solution (see inset, figure 4.11). In figure 4.10 there appears to be an immediate jump to a long period or chaotic solution immediately after the point at which grazing occurs. No matter how closely we look at this region we see this same sudden jump. There is a strong similarity between the overall qualitative behaviour of the two models : in both cases there is a bifurcation which leads to a large amplitude solution which appears to eventually become chaotic.

4.3 Analogous bifurcations in one dimensional maps

The numerical observations described in section 4.1 and 4.2 suggest that grazing bifurcations are in some sense limiting cases of saddle-node and flip bifurcations as the increase in stiffness at impact becomes large. However, we have presented only numerical results showing similarities between particular, first grazing bifurcations and their counterparts in the Hertz law model with a steeply increasing stiffness function at impact. In order to try to explain how the grazing bifurcation behaviour of a two dimensional map defined from the COR model could arise, we look at the behaviour of one dimensional maps of the interval with the same essential characteristics. The square root singularity in the derivative of a mapping defined by taking a two dimensional section through the three dimensional phase space of the COR model is seen to be the cause of the grazing bifurcation. We now examine the effect of introducing the same kind of square root singularity into the derivative of a one dimensional map of the interval. We consider two cases

$$x_{n+1}=\begin{cases} b+(h-2b)x_n \ , & 0 \le x_n \le \dfrac{1}{2} \\ \dfrac{h}{2}-\dfrac{\sqrt{2}h}{2}\left(x_n-\dfrac{1}{2}\right)^{\frac{1}{2}} \ , & \dfrac{1}{2} < x_n \le 1 \end{cases} \qquad 4.18$$

$$x_{n+1}=\begin{cases} b+(h-2b)x_n \ , & 0 \le x_n \le \dfrac{1}{2} \\ \dfrac{h}{2}+\sqrt{2}\left(1-\dfrac{h}{2}\right)\left(x_n-\dfrac{1}{2}\right)^{\frac{1}{2}} \ , & \dfrac{1}{2} < x_n \le 1 \end{cases} \qquad 4.19$$

These one dimensional mappings are illustrated in figures 4.12 and 4.13. We set the parameter $b=0.1$. The particular value of this parameter is not important to the argument, except that $b=0$ is avoided so that when $h=1$ we do not have a line of fixed points.

The parameter h in equations 4.18 and 4.19 corresponds to twice the height at which the square root singularity occurs, it can be seen from the equations to always occur at

$x_n=\frac{1}{2}$. Both in equations 4.18 and 4.19, as h is increased towards 1 there is a stable period one fixed point of the one dimensional maps (the points at which the solid curve crosses the dotted 45° line in figures 4.12 and 4.13, seen in figure 4.14 when $h<1$. In the higher line in figure 4.12, h has increased above 1 ($h=1.1$), and the period one fixed point has gone highly unstable (the derivative of the mapping is large and negative). Figure 4.13 shows the bifurcation diagram resulting from equation 4.18. There is an immediate jump to a long period, complicated, apparently chaotic solution as soon as $h>1$, similar to that seen in figure 4.6. However closely we zoom in on the bifurcation point at $h=1$ we never see a period doubling cascade to chaos. We can prove that equation 4.18 is indeed chaotic as soon as $h>1$. Rewrite the equation as $x_{n+1}=f(x_n)$. Define $x_0<\frac{1}{2}$ where $f(x_0)=\frac{1}{2}$ (i.e., $x_0=(1-2b)/2(h-2b)$) and $x_1>\frac{1}{2}$ where $f(x_1)=\frac{1}{2}$ (i.e., $x_1=1-1/h+1/h^2$). Then define $L=[x_0,\frac{1}{2}]$, $R=[\frac{1}{2},x_1]$. Now $f^2(L)=[f^2(\frac{1}{2}),f(\frac{1}{2})]$ and $f^2(R)=[f^2(\frac{1}{2}),f(\frac{1}{2})]$. Then if $h=1+\epsilon$, $\epsilon\ll 1$, we have $f^2(\frac{1}{2})-x_0=-\epsilon/2+O(\epsilon)<0 \Rightarrow f^2(\frac{1}{2})<x_0$ and $f(\frac{1}{2})-x_1=\epsilon-O(\epsilon^2)>0 \Rightarrow f(\frac{1}{2})>x_1$. Therefore $[x_0,x_1]=L\cup R \subset f^2(L)\cap f^2(R) = [f^2(\frac{1}{2}),f(\frac{1}{2})]$, and so f is chaotic as soon as $h>1$ (for the proof result about one dimensional maps see for example Block and Coppel [1992]). Furthermore we can define an interval $T\subset[0,1]$, $T=[f^2(\frac{1}{2}),f(\frac{1}{2})]$. The interval T can be decomposed into $T_1=[f^2(\frac{1}{2}),\frac{1}{2})$ over which f increases monotonically and, $T_2=[\frac{1}{2},f(\frac{1}{2})]$ over which f decreases monotonically. Now $f(T_1)\subset f(T_2)=[f^2(\frac{1}{2}),f(\frac{1}{2})]$. Therefore $f(T)=T \Rightarrow$ any point $t\in T$ is mapped by f into T, i.e., T is a trapping region for f, $f(\frac{1}{2})=h/2$, $f^2(\frac{1}{2})=(1-\sqrt{h-1})h/2$.

When the parameter h is less than one in equation 4.19 there are three fixed points, the points of intersection between the solid curve and the dotted $x_n=x_{n+1}$ line, two of which are stable and one unstable, illustrated by the lower line in figure 4.12 ($h=0.9$). At $h=1$ we can see that a stable and unstable fixed point meet and both disappear. As h is further increased above 1 as illustrated by the upper line in figure 4.12 ($h=1.1$), only one fixed point remains (at $x_n=1$) and this is stable since the slope is less than one so all initial conditions in the unit interval lead to this solution.

The relationship between the bifurcational behaviour of the one dimensional maps of the interval 4.18 and 4.19, and conventional saddle node and flip bifurcations can easily be seen. If the square root singularities were 'rounded off' and smooth maps were considered instead, at approximately $h=1$ there would clearly be a flip bifurcation in 4.18 and a saddle node bifurcation in 4.19.

The one dimensional maps described above, although displaying similar bifurcational behaviour to the two dimensional maps arising from the COR impact oscillator model, have not been derived from this model. Rather, they have been constructed so as to have the same square root singularity characteristic which causes grazing bifurcations. In order to analyze codimension one bifurcations of smooth maps it is possible to use centre manifold theory to reduce the dynamics of the system to a one dimensional (centre) manifold. A further coordinate transformation in the centre manifold yields the normal form of a bifurcation, which allows it to be classified, for example as a flip or saddle-node. Grazing bifurcations cannot be analyzed in this way since a centre manifold does not exist at a grazing bifurcation. One cannot even linearise the map around the fixed point at grazing, since the derivative of the map is not unique at this point. Since the qualitative behaviour of the two dimensional maps arising from COR impact oscillators seem to be captured by the one dimensional maps, equations 4.18 and 4.19, a similar transformation to reduce the behaviour at bifurcation to a one dimensional map would be desirable. This is an area which requires further work, as does the study more generally of maps which are continuous but not differentiable (to some degree).

4.4 Bifurcations of subharmonics

In section 3.7.2 and 3.7.4 we derived expressions for possible solutions to the COR impact oscillator of period one with one impact per period. Almost exactly the same analysis can be used to locate subharmonics of the same COR model with one impact in N periods where N=2,3,4,... . The only changes which are required are that instead of looking for an orbit which repeats after time T (one period) we look for one which repeats after time NT (N periods). In equation 3.30 the we just put $t_f-t_i=2\pi N/\omega$, which modifies the constants ν, c_w and s_w. The procedure for locating possible steady state solutions is then identical to that for period one solutions. First, the quadratic 3.32 is solved for the velocity at impact y_i and this is then substituted into one of 3.31 to solve for the time at impact, t_i. The possible solution given by this procedure must be numerically verified to ensure it is a true, physical solution. The jacobian matrix of the impact map for period N solutions is obtained by substituting the modified constants ν, c_w and s_w into equations 3.39 to 3.42 to obtain the elements of the matrix defined in equation 3.43. Equation 3.45 then gives the eigenvalues of the jacobian exactly as before.

Using the expressions for the eigenvalues of the jacobian we can locate the loci of saddle-node and flip bifurcations of period N, one impact steady state solutions as in section 4.1.5. The loci of these bifurcations for steady state, one impact solutions of periods 2,3 and 4 are shown in figure 4.15 as the two parameters α and ω are varied. Also shown in this figure are the lines of grazing bifurcations.

Frequency response curves for various fixed forcing amplitudes are shown in figures 4.16 to 4.19. Both the maximum absolute displacement, x_{max} and the maximum velocity at impact $\dot{x}_{max}$ over N forcing cycles are shown plotted against the forcing frequency ω. Stable solutions are represented by a solid line whilst unstable solutions are shown with a dotted line. Only the period N, one impact steady state solutions are shown in these figures, i.e. those which can be calculated analytically. In figure 4.16 the forcing parameter is kept fixed at $\alpha=0.5$. In this case there are two "first grazing" bifurcations either side of the linear natural frequency $\omega=1$. As the forcing frequency is increased from 0 only there is a stable non-impacting limit cycle whose amplitude grows as the frequency is increased towards 1. First grazing bifurcations occur at $\omega=0.710...$ and $\omega=1.218...$, of "flip type" and "saddle-node type" respectively. The overall shape of this frequency response curve is typical for small forcing amplitudes, such as in the experiment which we describe in chapter 6. All of the solutions shown in figure 4.16 are of period one, and no higher period, one impact solutions exist at this low forcing amplitude. Figures 4.17 to 4.19 show the response curves up to period four for the forcing amplitudes $\alpha=1.5$, 2.5 and 3.5. In each of these figures, there is only one first grazing bifurcation, at $\omega=1.578...$, 1.868... and 2.119... respectively. The higher period, one impact solutions all disappear as frequency ω is increased at a saddle-node bifurcation, but some appear at saddle-node bifurcations and others are created at grazing bifurcations.

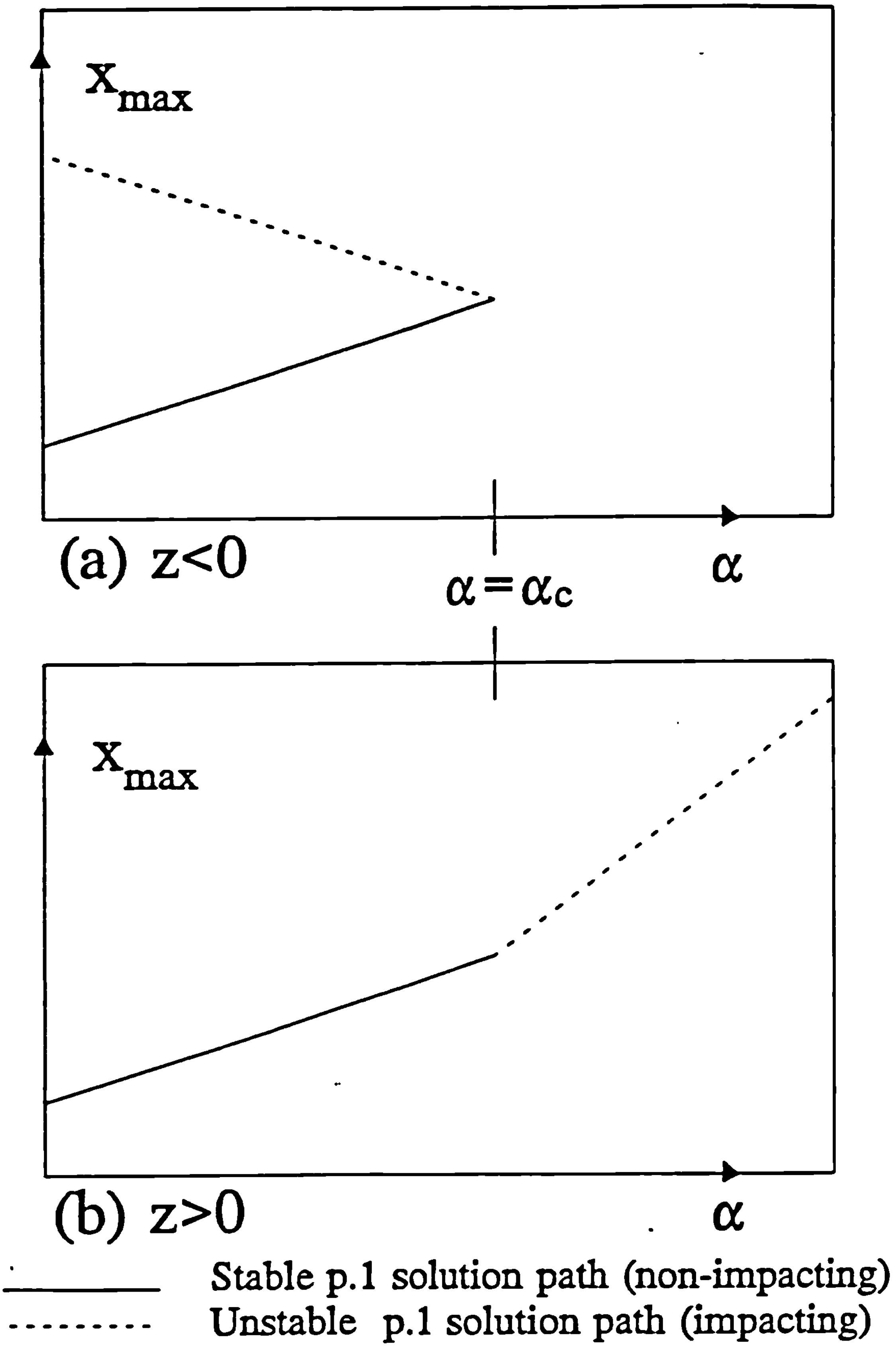

Figure 4.1 The two types of first grazing bifurcation for (a) $z<0$, (b) $z>0$

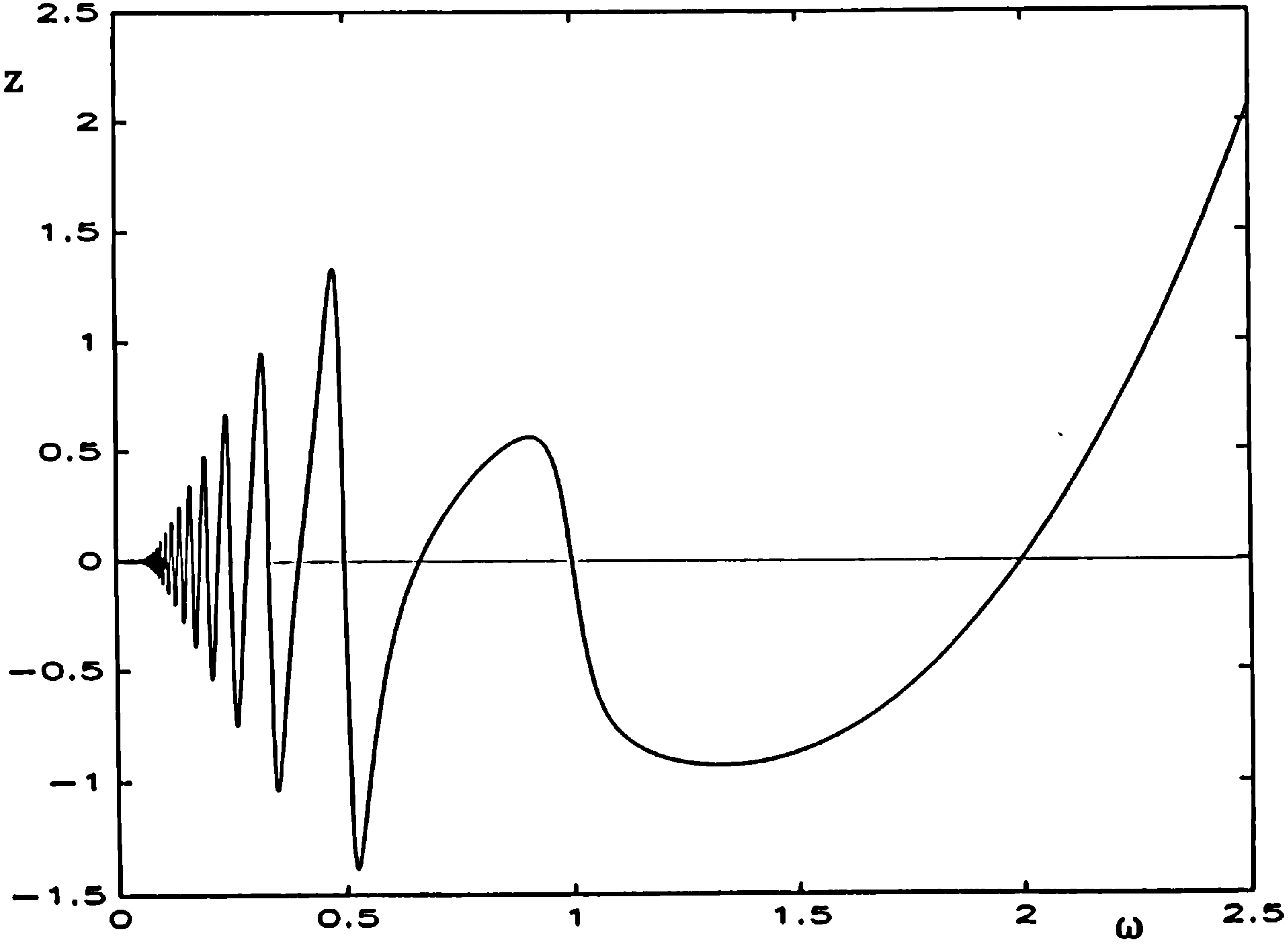

Figure 4.2 The function $z(\omega)$ against ω. The sign of z determines the type of first grazing bifurcation of the one sided COR impact oscillator.

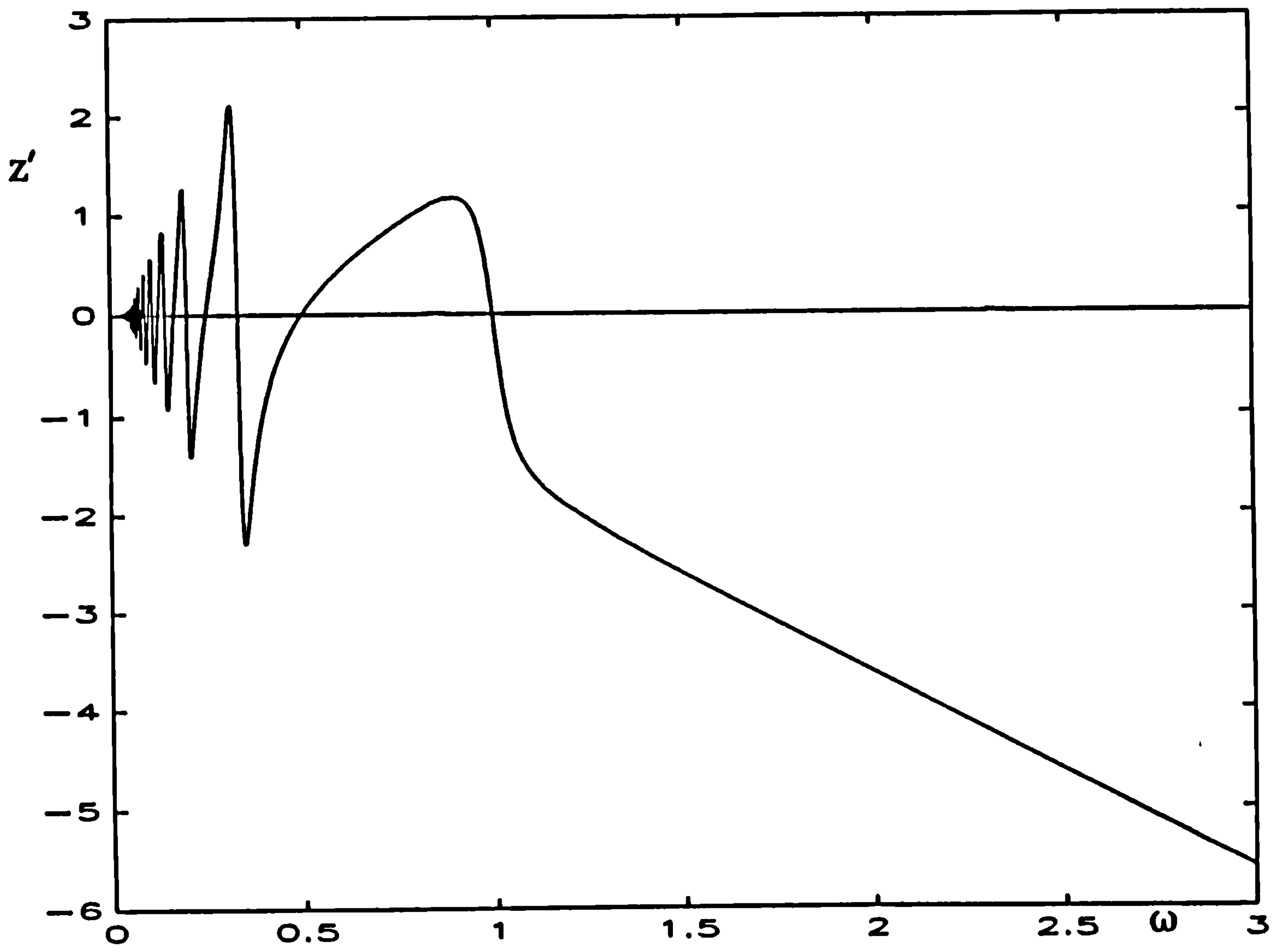

Figure 4.3 The function $z'(\omega)$ against ω. The sign of z' determines the type of first grazing bifurcation of the two sided COR impact oscillator.

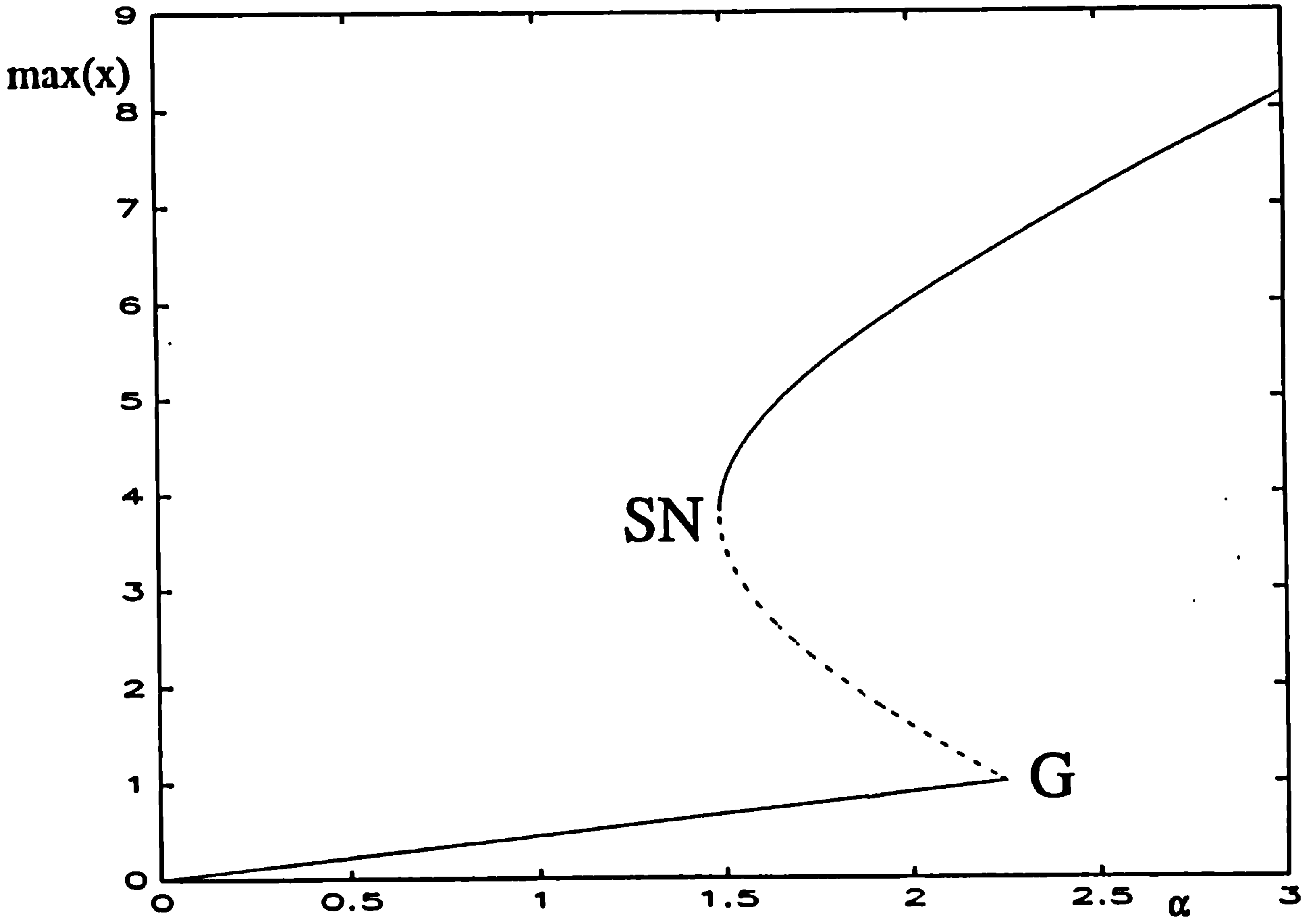

Figure 4.4 The saddle-node type first grazing bifurcation at $\omega=1.8$. The maximum absolute displacement over one period, *max(x)*, is plotted against forcing amplitude α with all other parameters fixed as in section 4.1.4. G indicates a grazing bifurcation, SN a conventional saddle-node. Solid lines represent stable, dotted lines unstable period one solutions.

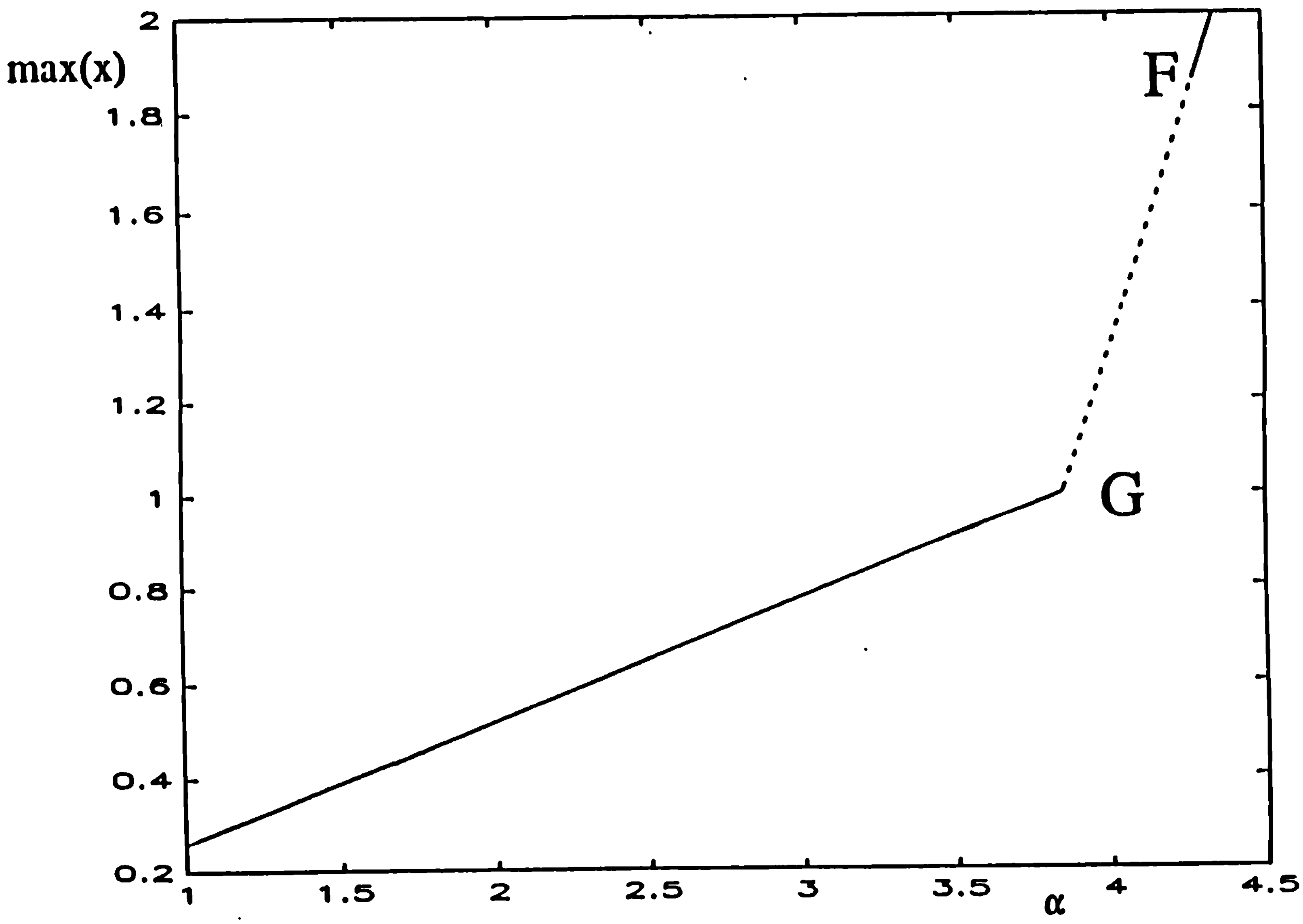

Figure 4.5 The flip type first grazing bifurcation at $\omega=2.2$. The maximum absolute displacement over one period, *max(x)*, is plotted against forcing amplitude α with all other parameters fixed as in section 4.1.4. G indicates a grazing bifurcation, F a conventional flip. Solid lines represent stable, dotted lines unstable period one solutions.

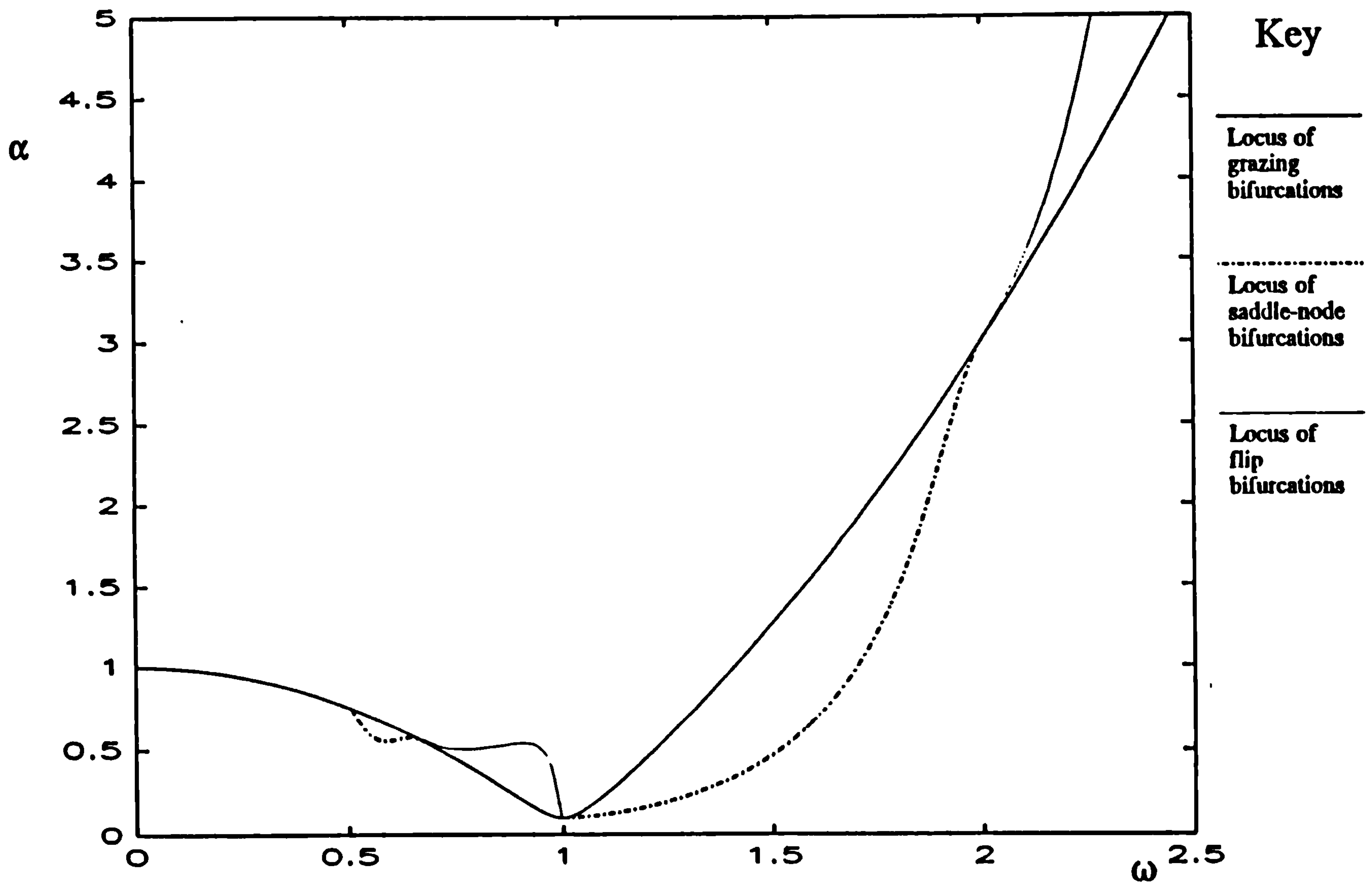

Figure 4.6 Bifurcation loci for the one sided COR impact oscillator. Shown are the locus of first grazing bifurcations, the locus of flip bifurcations of period one, one impact orbits and the locus of saddle-node bifurcations of period one, one impact orbits.

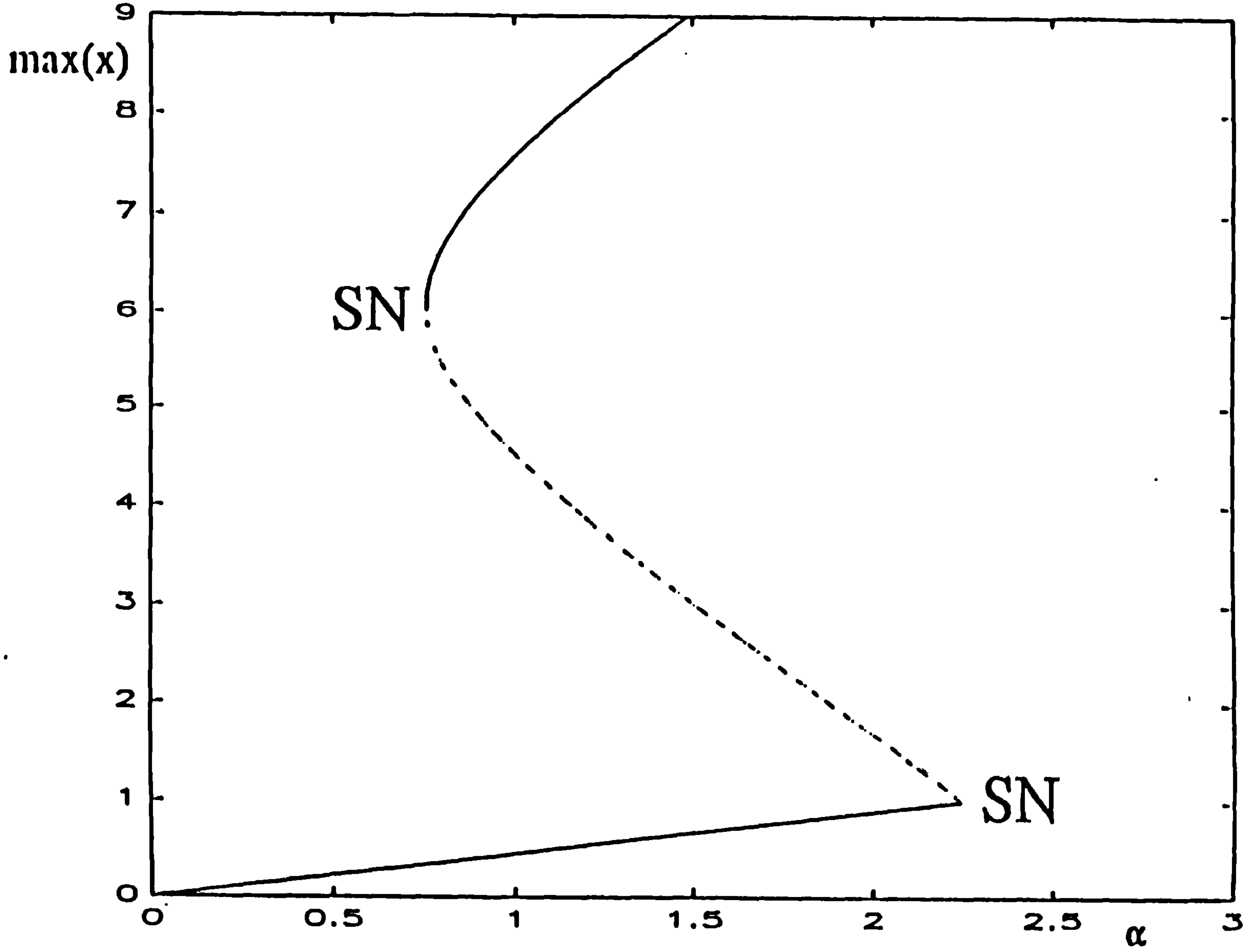

Figure 4.7 Path of period one solutions of the Hertz law model, parameters as for figure 4.4, k=2000 in equation 3.3. The maximum displacement over one period, *max(x)*, is plotted against α. SN indicates a saddle-node bifurcation. Solid lines represent stable, dotted lines unstable period one solutions.

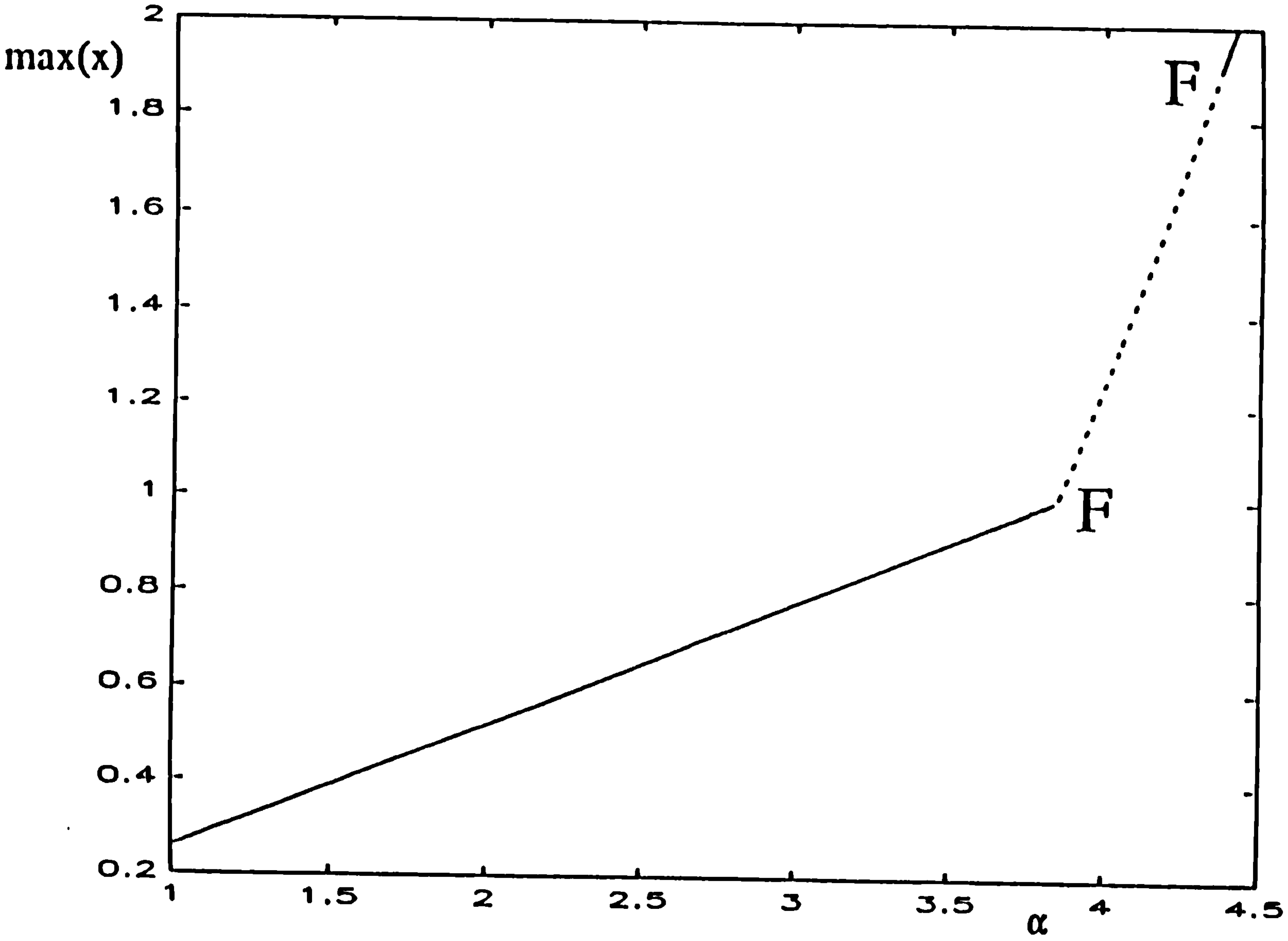

Figure 4.8 Path of period one solutions of the Hertz law model, parameters as for figure 4.5, k=2000 in equation 3.3. The maximum displacement over one period, *max(x)*, is plotted against α. **F** indicates a flip bifurcation. Solid lines represent stable, dotted lines unstable period one solutions.

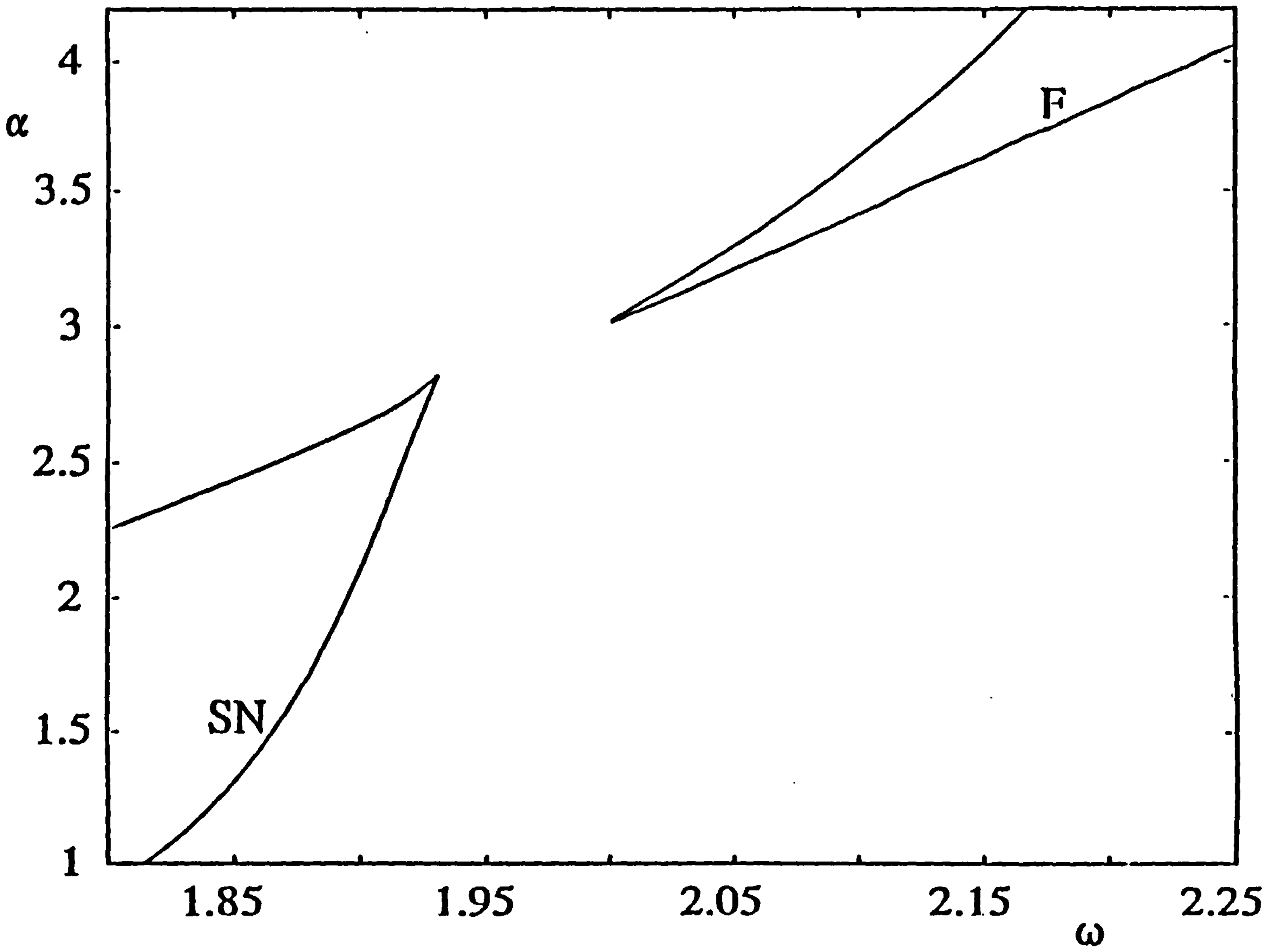

Figure 4.9 Bifurcation loci for the one sided Hertz law impact oscillator. Shown are the locus of saddle-node bifurcations SN and the locus of flip bifurcations F of period one orbits.

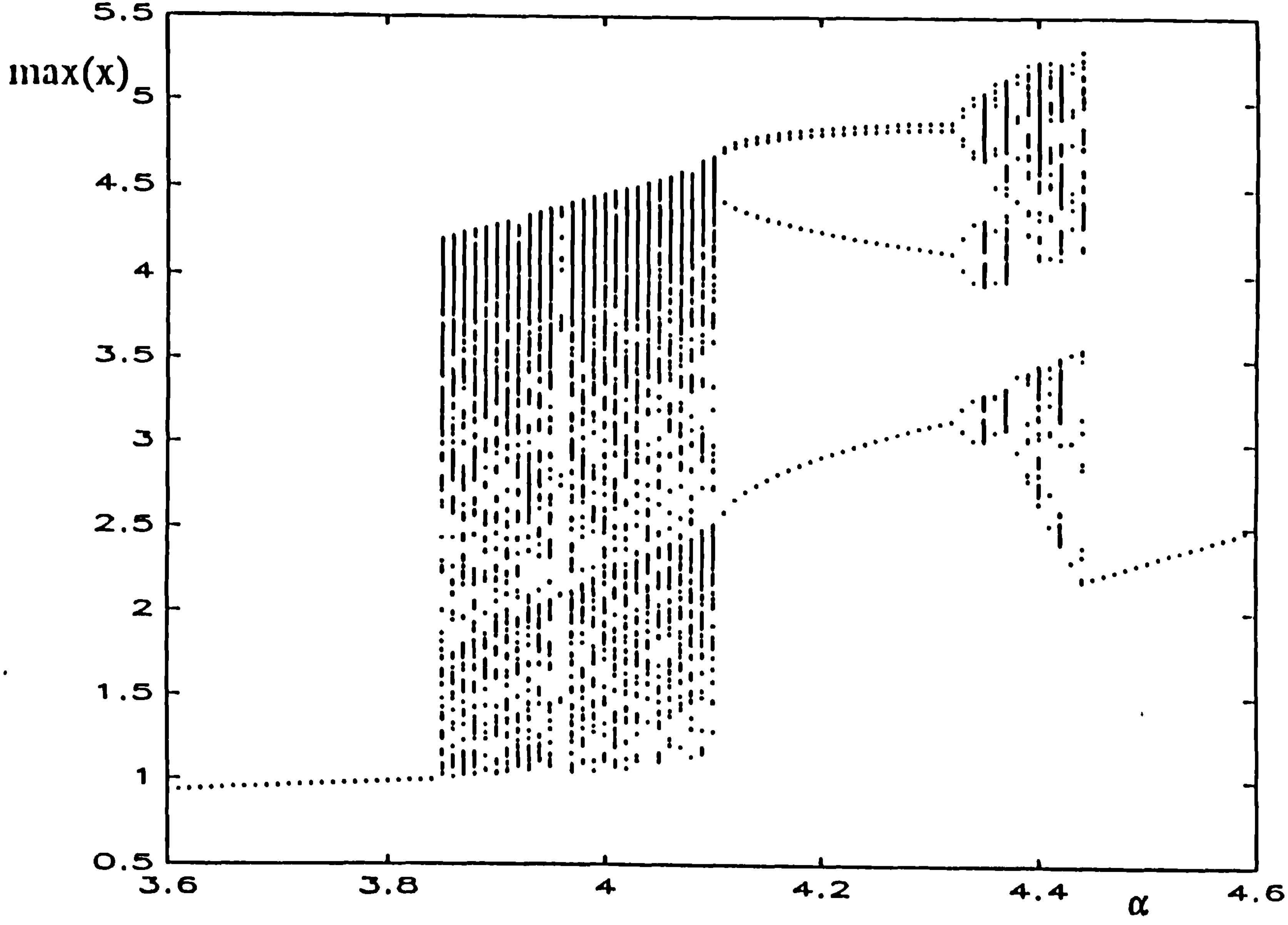

Figure 4.10 Bifurcation diagram for the COR model, parameters as in figure 4.5, obtained by allowing α to slowly increase. The maximum displacement over one period, *max(x)* is plotted against α for 100 periods.

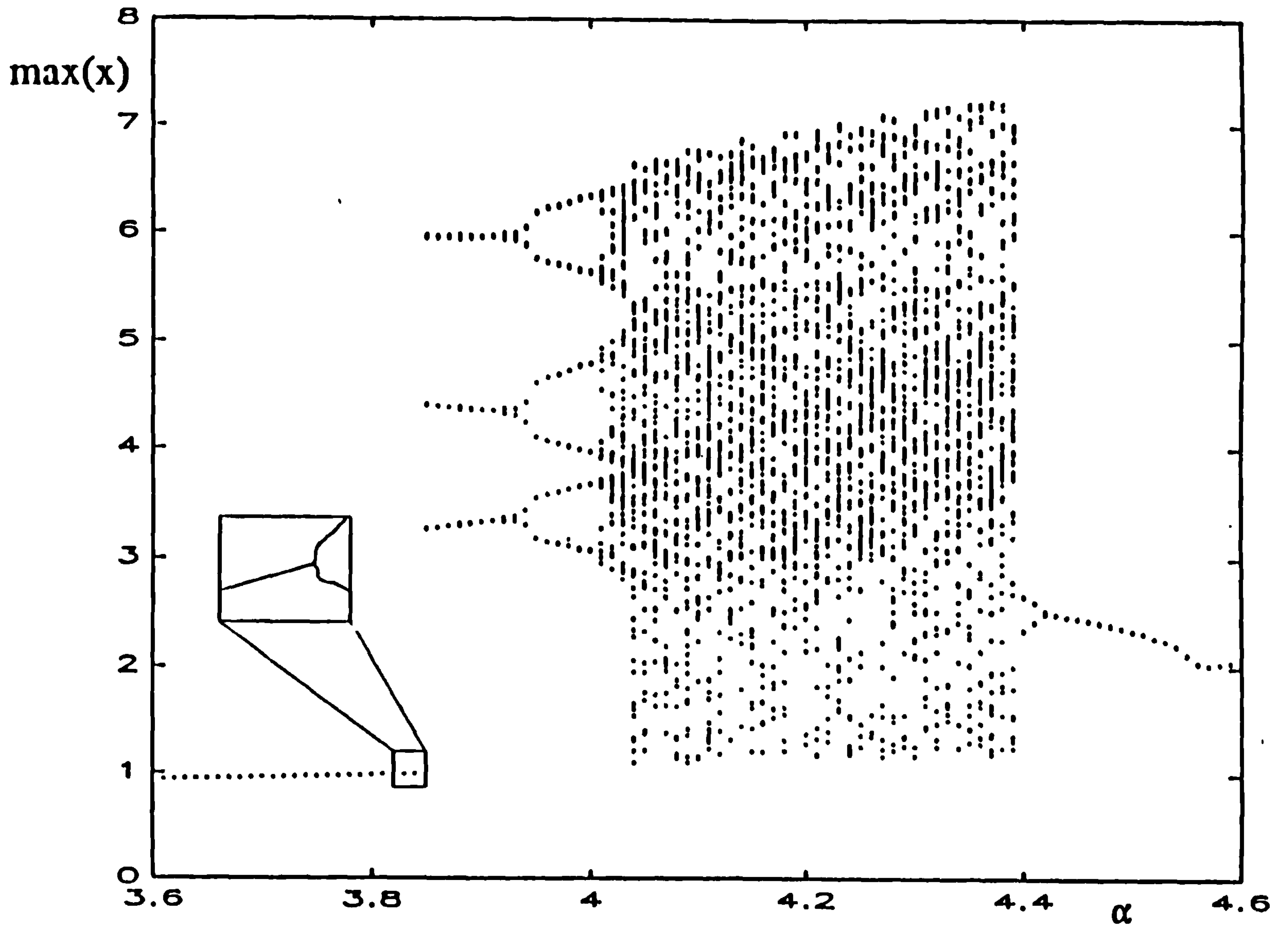

Figure 4.11 Bifurcation diagram for the Hertz law model, parameters as in figure 4.8, obtained by allowing α to slowly increase. The maximum displacement over one period, *max(x)*, is plotted against α for 100 periods. The inset shows a blown up area around the region where impacts initially occur, showing a period two solution.

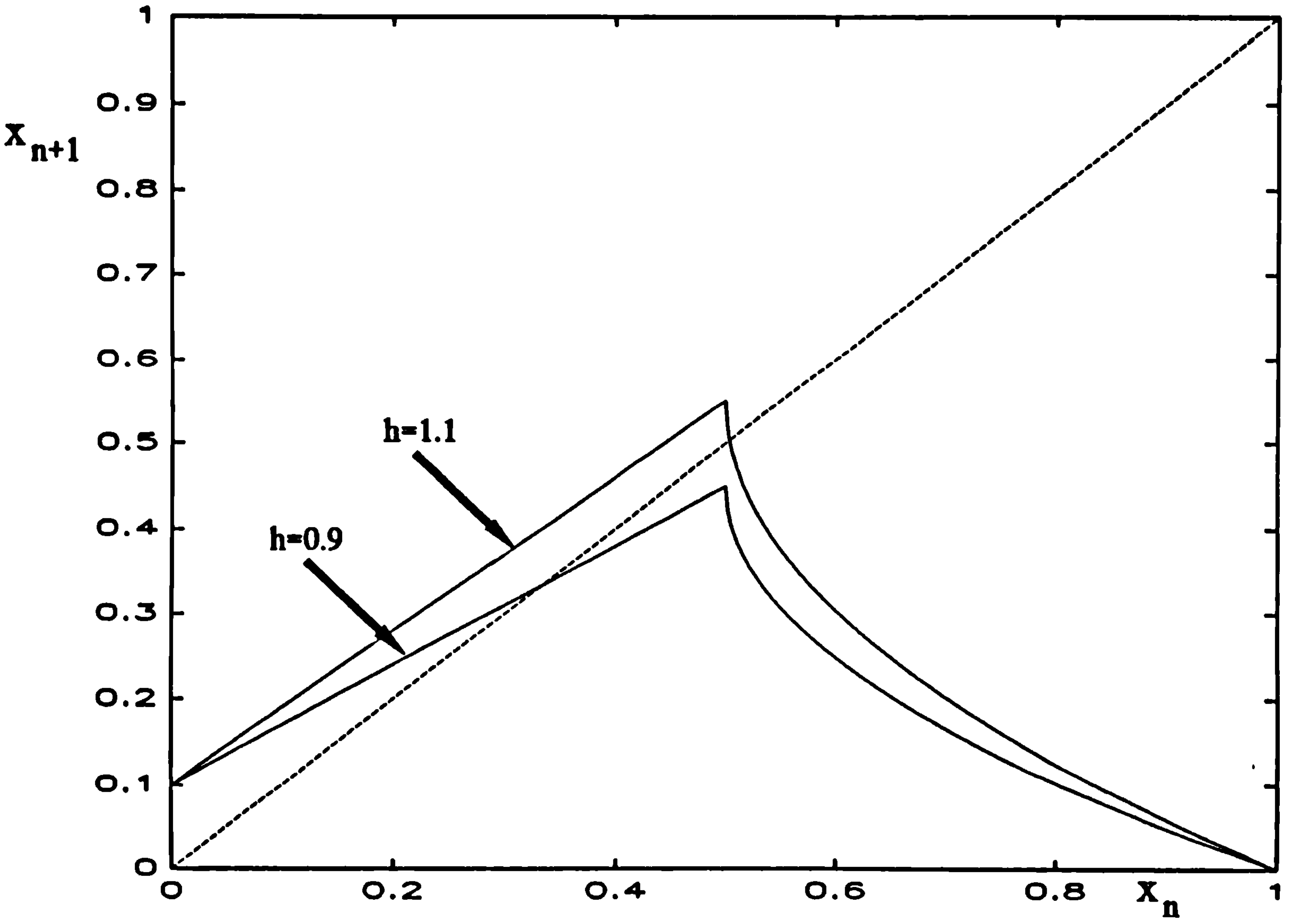

Figure 4.12 The one dimensional mapping given by equation 4.18 with b=0.1, h=0.9 and h=1.1. The 45° $x_{n+1}=x_n$ line shown dotted.

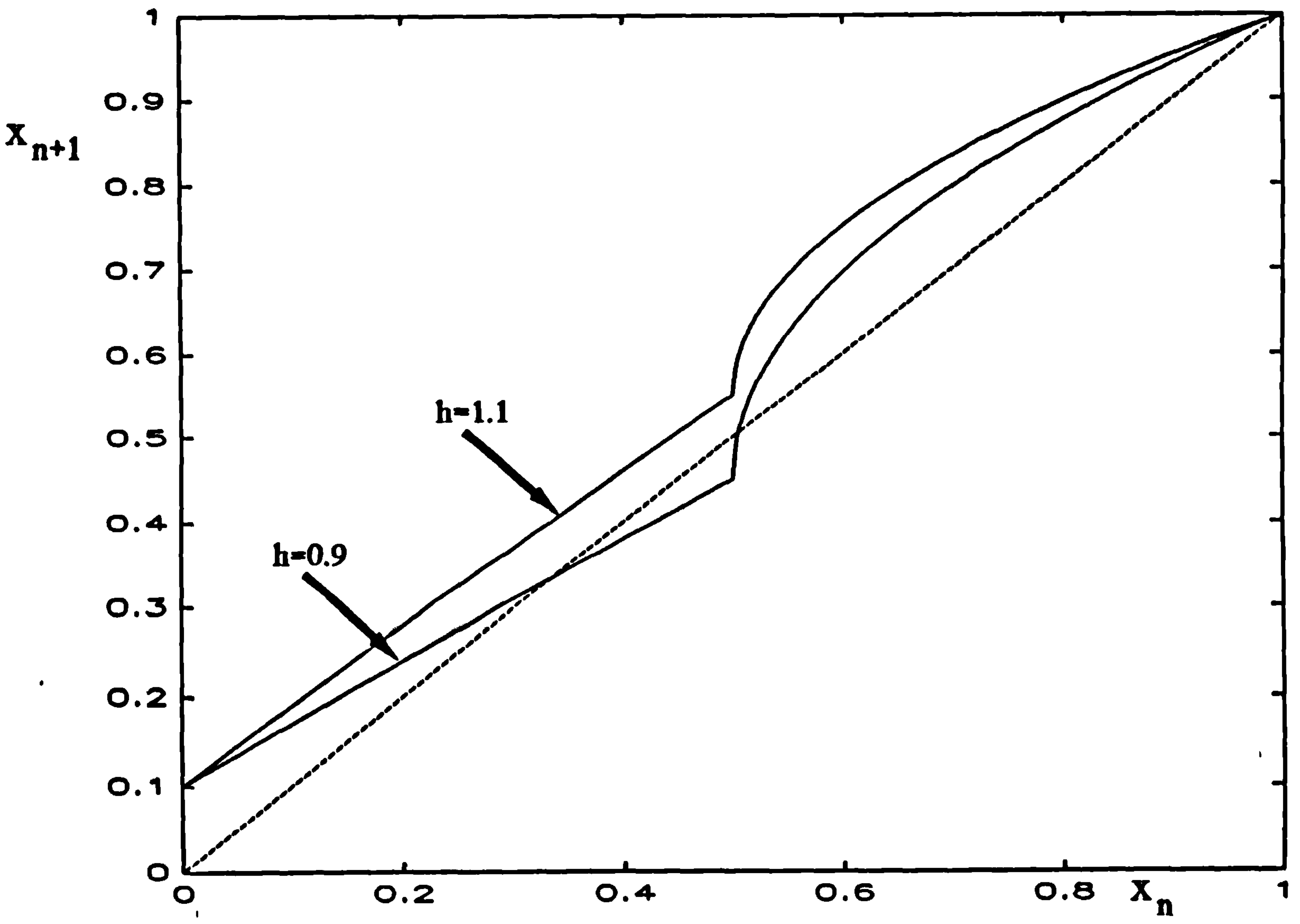

Figure 4.13 The one dimensional mapping given by equation 4.19 with b=0.1, h=0.9 and h=1.1. The 45° $x_{n+1}=x_n$ line shown dotted.

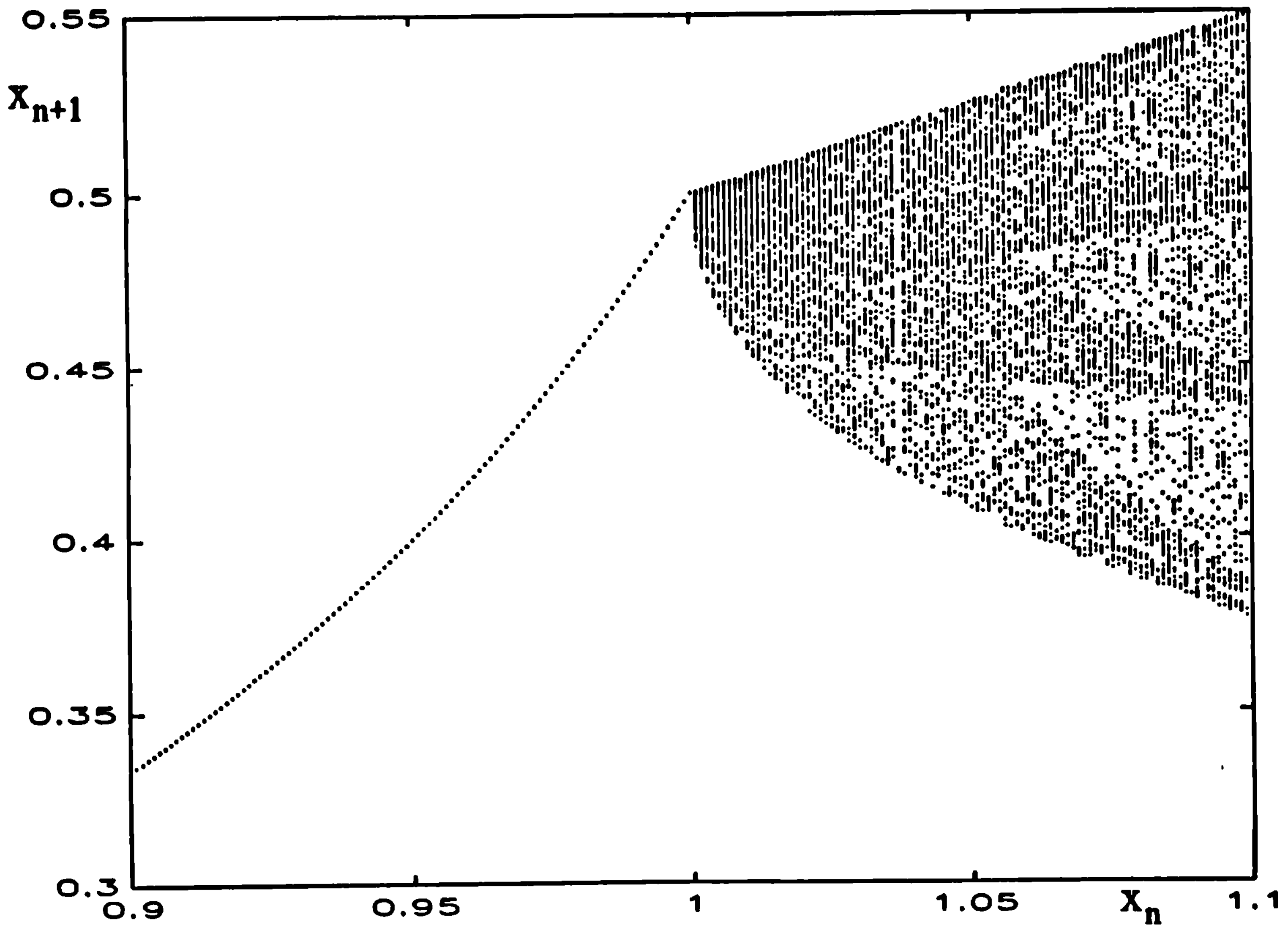

Figure 4.14 Bifurcation diagram resulting from equation 4.18 as *h* is slowly increased. There is chaotic solution immediately created as *h* is increased through 1.

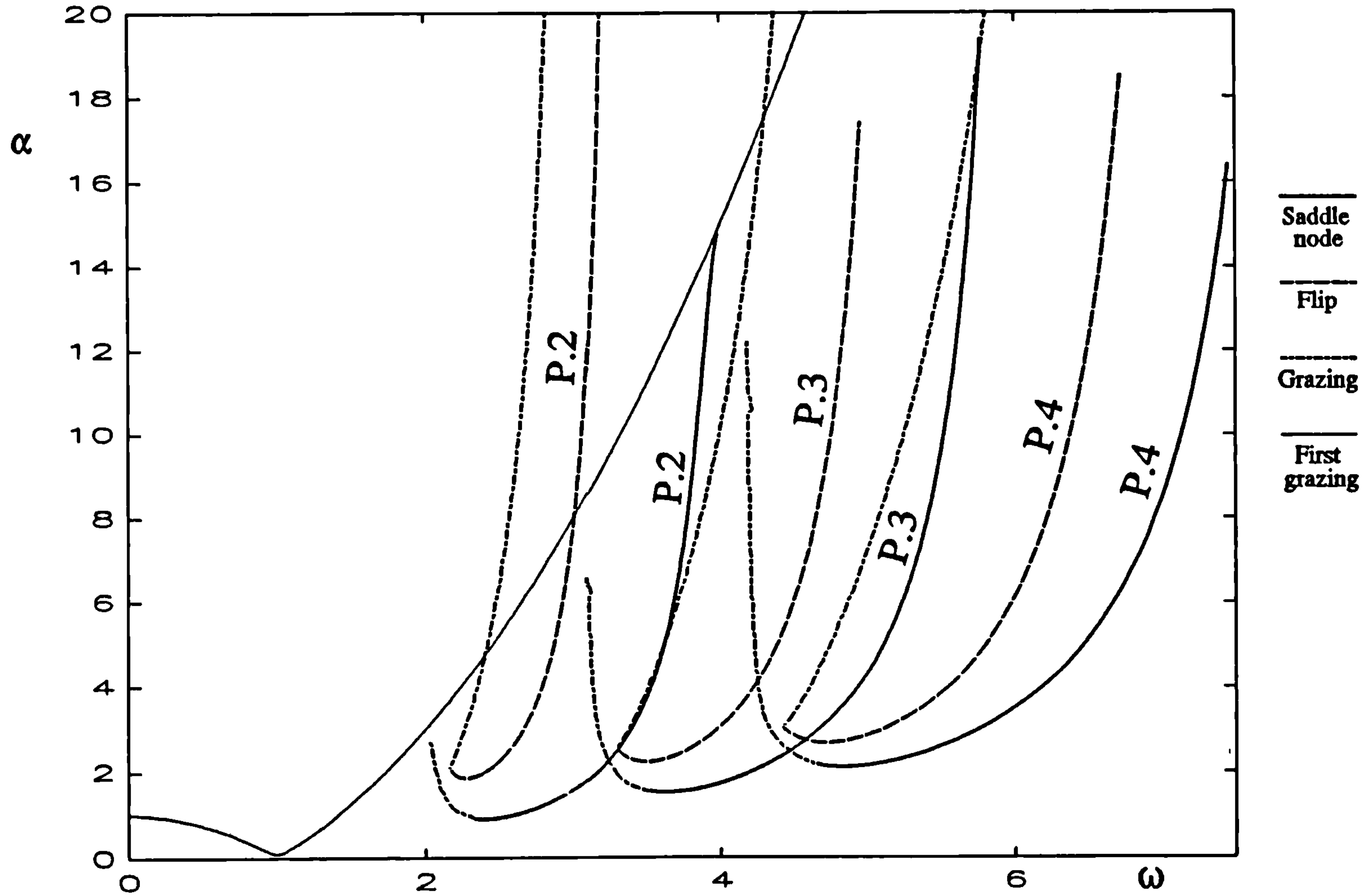

Figure 4.15 Bifurcation loci for period two, three and four one impact solutions of the COR impact oscillator, parameters as section 4.1.4, as α and ω are varied. Shown are lines of saddle-node, flip and grazing bifurcations.

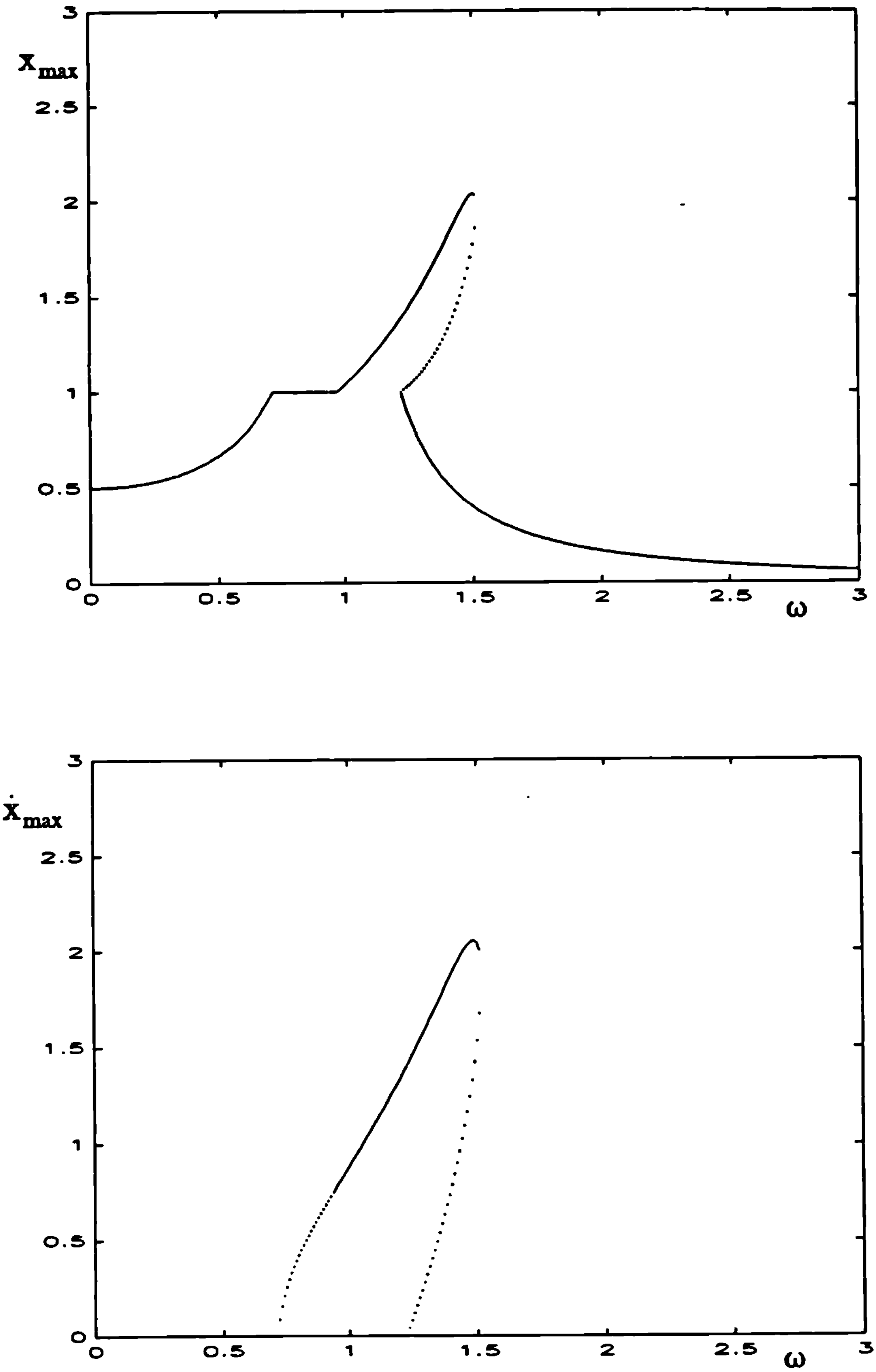

Figure 4.16 Response curves of maximum displacement x_{max} and velocity $\dot{x}_{max}$ for period one solutions against forcing frequency, ω. Parameters as in section 4.1.4, $\alpha=0.5$. Solid lines represent stable solutions, dotted lines unstable.

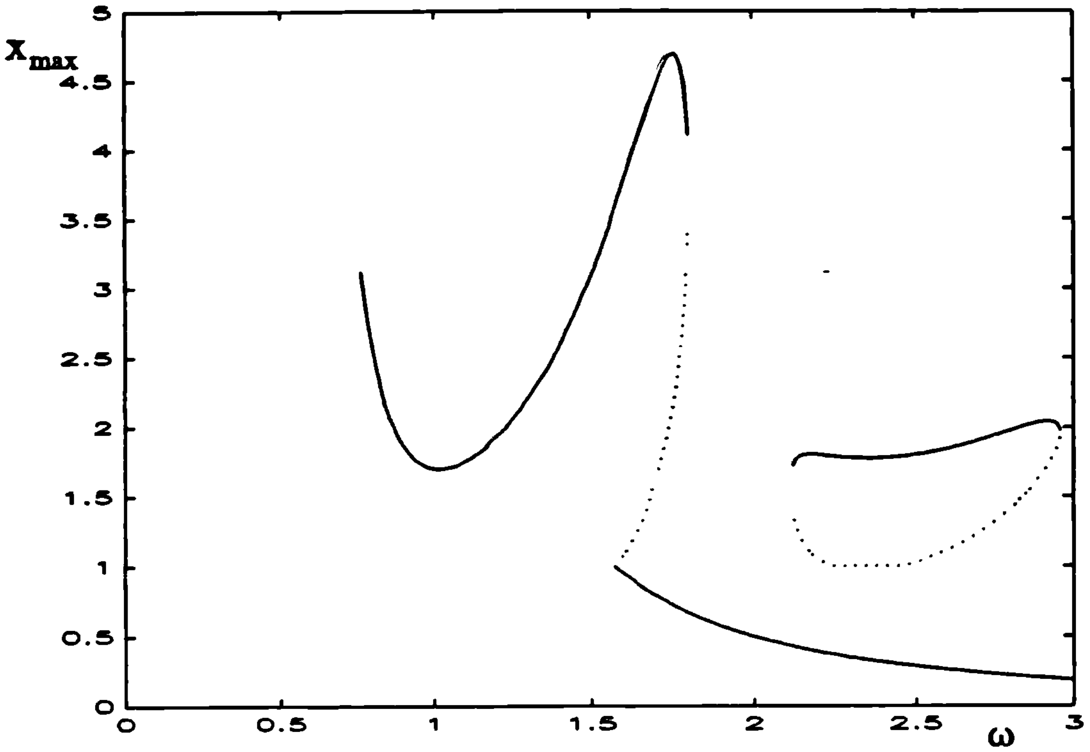

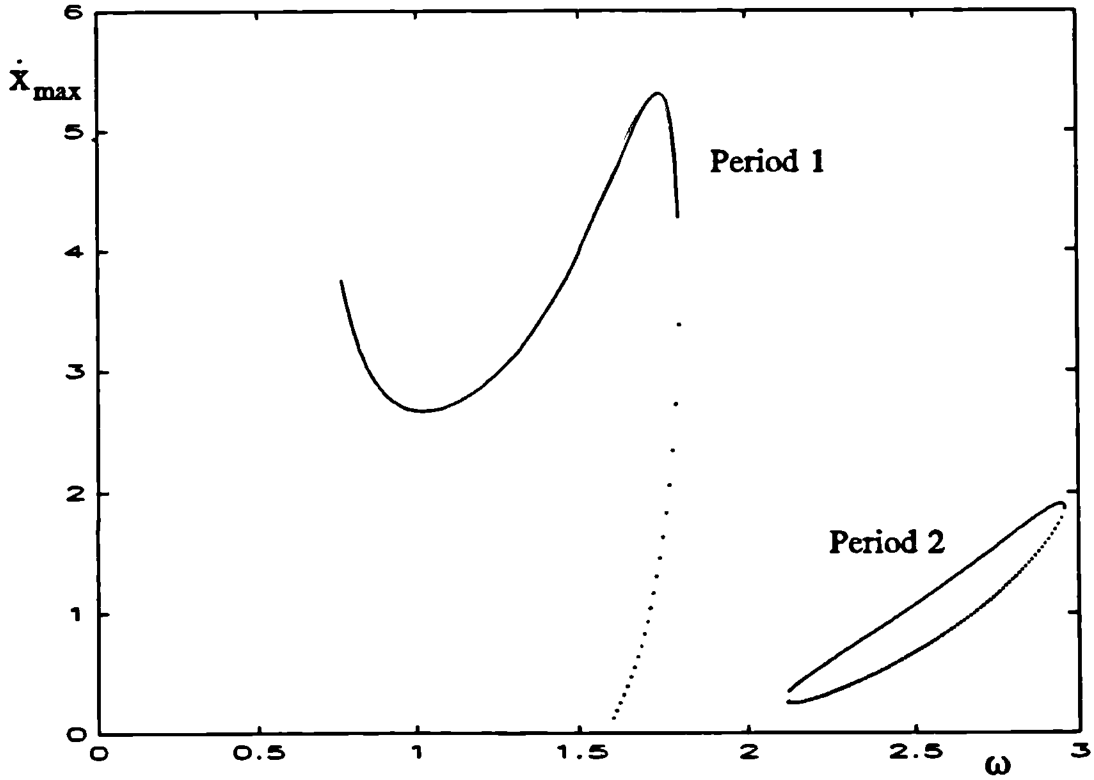

Figure 4.17 Response curves of maximum displacement x_{max} and velocity $\dot{x}_{max}$ for period one and period two, one impact solutions against forcing frequency, ω. Parameters as in section 4.1.4, $\alpha = 1.5$. Solid lines represent stable, dotted lines unstable solutions.

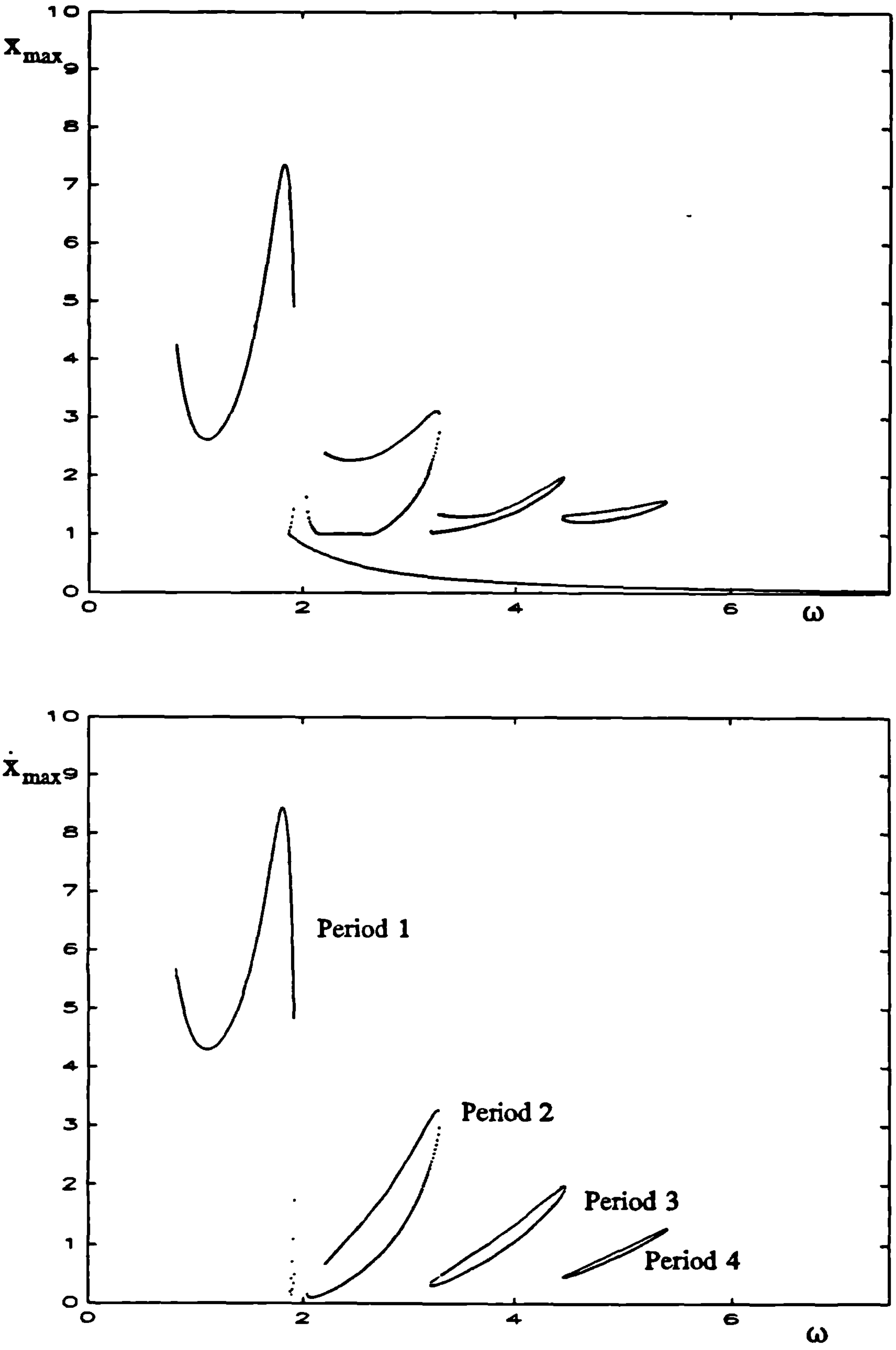

Figure 4.18 Response curves of maximum displacement x_{max} and velocity $\dot{x}_{max}$ for period one to period four, one impact solutions against forcing frequency, ω. Parameters as in section 4.1.4, $\alpha=2.5$. Solid lines represent stable, dotted lines unstable solutions.

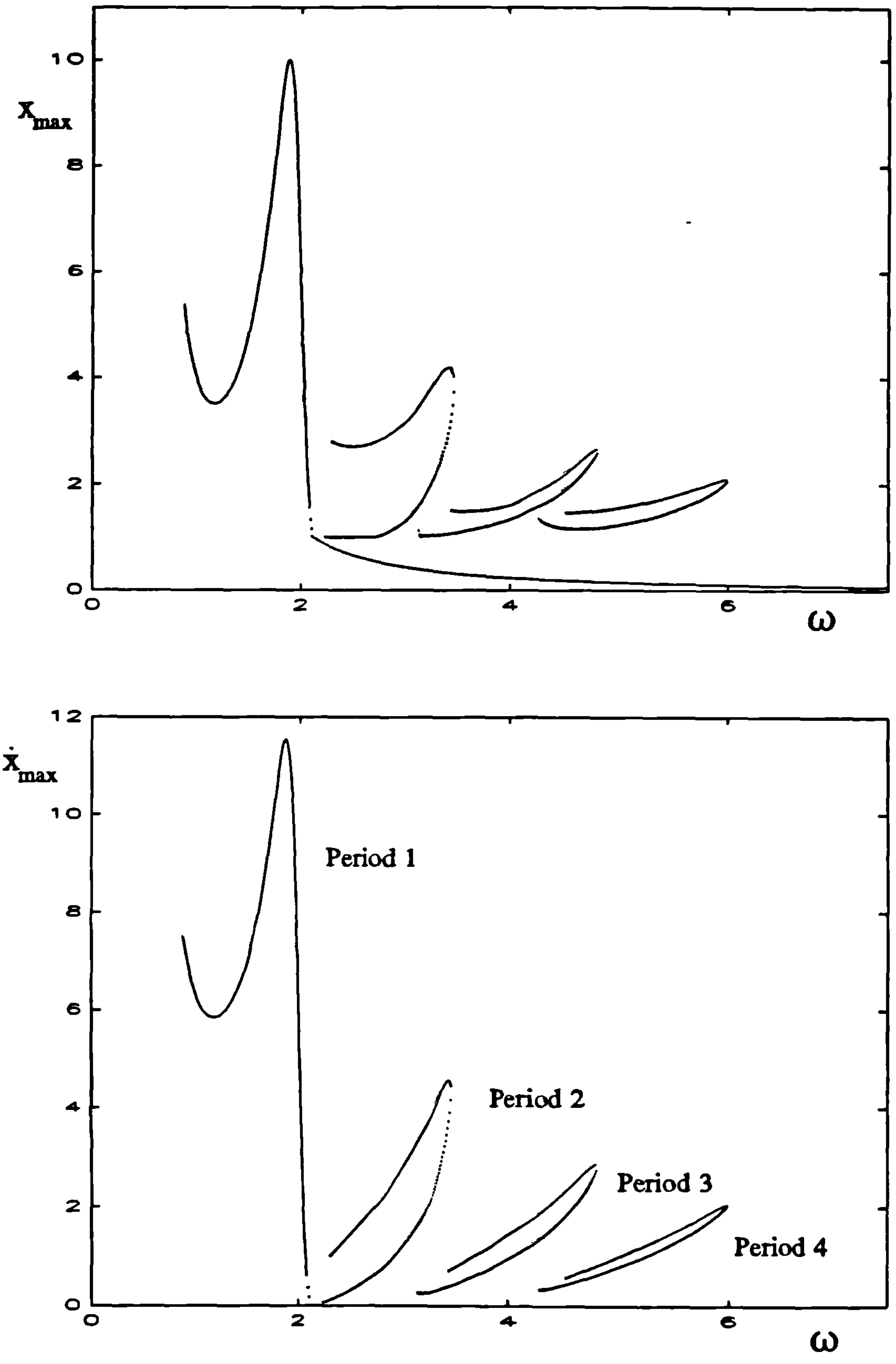

Figure 4.19 Response curves of maximum displacement x_{max} and velocity $\dot{x}_{max}$ for period one to period four, one impact solutions against forcing frequency, ω. Parameters as in section 4.1.4, $\alpha=3.5$. Solid lines represent stable, dotted lines unstable solutions.

5. Impacting offshore systems

5.1 Introduction

The work in this thesis was originally motivated by a particular problem involving impacts which arises in offshore engineering. The problem of dangerous resonant behaviour developing in impacting dynamical systems is not restricted to this problem, or to offshore engineering. In this section we briefly mention some of the areas in which such problems do arise, before concentrating on some of the particular problems which arise in offshore engineering, and finally concentrating on the one which has motivated this study. The theoretical insights into impacting dynamical systems which have been discussed in chapters 3 and 4 have mainly concentrated on the qualitative changes in behaviour which occur when a component just hits a stop with zero velocity. These *grazing bifurcation* events can lead to a sudden jump to a different (possibly "dangerous") solution or to complicated, nonperiodic, chaotic motions, even under simple sinusoidal forcing. A simple model which is developed in this chapter for the pile/sleeve interaction problem which motivated this study is shown to have a very complicated dynamical response, including several grazing bifurcation events, the effect of which must be fully appreciated in order to understand the overall behaviour of the nonlinear dynamical system.

Physical and engineering systems which undergo impacts at motion limiting constraints are encountered in a wide range of situations such as rattling mechanical gears [Pfeiffer & Kunert, 1990], impact printer heads [Tung & Shaw, 1988a,b], the pounding of buildings under earthquake excitation [Davis, 1992] and heat exchanger tubes subject to aerodynamic excitation [Paidoussis & Li, 1992]. Such systems are inherently highly nonlinear since there are two greatly different "regimes". Any model of a system with impacts must include a regular, between impact regime and also the completely different behaviour at an impact. Offshore engineering is a source of several examples of this type of system. A good understanding of the dynamical responses of offshore structures subject to impacts is therefore very important. In mechanical systems with impacts such as gear rattle or impact printers, the main problems are which are caused by repeated impacts at a stop are noise and wear. In the offshore environment, however, a short burst of large impacts could cause great damage or even the complete failure of a structure.

Early studies by Thompson and co-workers [Thompson, 1982, Thompson & Ghaffari, 1982,1983, Thompson & Elvey, 1984, Thompson, Bokaian & Ghaffari, 1983,1984] investigated the dynamical behaviour of an articulated mooring tower with an oil tanker moored to it by a light mooring line. The tanker itself can be regarded as an immovable fixed object, whilst the articulated mooring tower is essentially an inverted pendulum pinned to the sea bed. The tower oscillates under wave forcing causing the mooring lines to repeatedly slacken and then tighten again. This behaviour can be modelled as a bilinear stiffness (one stiffness regime with the line slack, with the restoring moment on the tower solely due to buoyancy and the other, much greater stiffness with the line taut). If the stiffness with the line taut is considerably greater than with it slack then the system can be reasonably modelled as an impact oscillator. Numerical investigations by Thompson showed a complex response of a one degree of freedom model of such a mooring tower, with subharmonic motions of order n at approximately n times the natural frequency of the structure. Aperiodic, chaotic solutions were also found to exist for this simple system. A problem similar to that of the dynamical response of an articulated mooring tower is the response of ships moored either against stiff fenders in a harbour [Lean, 1971], or moored to a fixed offshore platform [Sterndorff et al, 1992]. In the case of a ship moored to a small fixed offshore platform the impact load of the ship can be greater than the expected extreme environmental loads and so the ship impact can govern the design of the platform.

Another example of an offshore dynamical impacting system arises in the installation of platforms over pre-installed templates on the sea bed over pre-drilled wells. Some kind of indexing system is used, as described in the next section, to guide the platform accurately into position over the pre-drilled well with a guiding component on the sea bed and a corresponding component on the platform itself. Although the problem of impacts between the two components that make up the indexing system only occurs in the short time whilst the platform is actually being installed over the template, it is very important that excessive loads are avoided during this time. It is this problem that we now go on to examine in more detail.

5.2 Jacket to template docking problems

The conventional method, until recently, of developing an offshore hydrocarbon field has been to construct and then install the jacket structure prior to drilling the well. The recovery of capital investment can be achieved far more quickly if the drilling operation can be performed in tandem with the construction of the jacket structure. The wells are drilled and capped off, with a template installed over them so that the platform can be accurately located over the well when it is finally installed, possibly two or three years after drilling. Accurate location of the jacket structure over the pre-installed template is essential since the wells are pre-drilled. Different methods for docking the structure have been tried and one of the common limitations of such methods is excessive impacts between the jacket and the guiding template. The dynamical response of the nonlinear system comprising the jacket structure and template needs to be understood if the installation process is to proceed successfully. This is essentially a forced impacting oscillator problem, and in this section one particular docking method is discussed.

Several different methods for locating the jacket structure over the locating template are used in practice. All involve some kind of restraining arrangement on or near the template with which part of the jacket structure is mated. Amoco's Northwest Hutton platform was installed using a bumper-pile system for the mating of the platform and template [Nelson et al, 1983, Stahl et al, 1983]. This technique involves the installation of bumper piles near to the subsea template against which the platform structure is manoeuvred, protecting the template from damage and orienting the structure correctly. The bumper piles must be designed in order to withstand the impact loads inflicted on them by the jacket in the installation procedure. An alternative method is to use a pin/sleeve combination arrangement. Two or three docking piles are installed in the template which act as either the male or female component with either a pin or sleeve mounted in the jacket. The gap between the pin/sleeve combination is designed to taper down from a large distance at initial engagement to a distance small enough to be within the required tolerance for the final position of the structure when fully installed. This method was used in the installation of the Beryl B jacket in the North Sea [Robinson & Ramzan, 1988].

Robinson & Ramzan performed a numerical simulation of the installation of a 7500 tonne jacket in a water depth of 66m using the pin/sleeve docking arrangement described above, illustrated in figure 5.1. The structure was modelled as a 12 degree of freedom system which has a piecewise linear stiffness function, where the stiffness matrix changes on pile contact, forced by a random sea state with specified spectrum type of a given significant wave height. At the closing stages of the installation procedure the pile loads were found to become largest. In particular, the pile loads (the forces at the piles) were found to be highly dependent on the mean period of the forcing function. Figures 5.2 and 5.3 show the results of two runs of these numerical simulations taken from Robinson & Ramzan [1988]. It was found that the jacket sway amplitude increased rapidly at mean wave periods of greater than 5 seconds. The two runs shown are taken at 6 seconds and 7.8 seconds mean wave periods. In the first case, the jacket sway behaviour was such that the structure was impacting mainly at one of the piles, with only occasional occurrences of two sided impacting, which Robinson & Ramzan called "ringing behaviour". In the second case, at mean wave periods of 7.8 seconds there are long bursts of high amplitude, ringing (two sided impacting) behaviour with occasional less severe periods where there are only one sided impacts.

The natural period of free oscillations of the sway mode, the mode associated with the high amplitude ringing events in the numerical simulations described above, is given by Robinson & Ramzan as 7 seconds. The one-sided low amplitude impact events are observed from these simulations to be taking place just above the natural frequency of this mode and the high amplitude two sided ringing events take place at a lower frequency, just below the natural frequency. It appears from the time series in figure 5.3 that neither the surge or heave modes play an important role in the onset of the ringing events which lead to unacceptably high loads at the piles. There is clearly some unexplained nonlinear behaviour taking place here since resonances are occurring away from the natural frequency of oscillation of the sway mode : this is not surprising since, as has already been discussed, a system with impacts has two very differing regimes at and away from impacts and so the system is naturally very nonlinear. We could expect the transition from low amplitude one sided to high amplitude two sided impacting to show up in a simple one degree of freedom model of the sway motion.

In order to see how the behaviour described by Robinson & Ramzan could be explained by a very simple one degree of freedom model of only the sway motions of the jacket we use the simple coefficient of restitution model with a linear stiffness and linear damping, sinusoidally forced. Despite being a possibly over simple model for the impact process, part of the work of this project has been to show that the overall qualitative behaviour which arises from the coefficient of restitution rule is the same as that which arises from more realistic rules. Experimental work with laboratory impact oscillator models also shows that qualitative behaviour is predicted well by the coefficient of restitution impact rule. The one degree of freedom model is given by

$$\begin{gathered} MX'' + \Delta X' + \omega_c^2 X = A\cos(\Omega\tau) \quad , \quad r_s < X < l_s \\ X' \rightarrow -rX' \quad , \quad X = r_s \ \ or \ \ X = l_s \end{gathered} \qquad 5.1$$

where :

M : effective mass

Δ : linear damping coefficient

ω_c : natural frequency of the sway oscillations

Ω : forcing frequency of sway oscillations

A : amplitude of the forcing of sway oscillations

r : coefficient of restitution

r_s : distance from equilibrium position to right hand stop

l_s : distance from equilibrium position to left hand stop

X : displacement from equilibrium position of sway mode

τ : time

' : time derivative

In contrast, the 12 degree of freedom model used a piecewise linear stiffness function to model the impact, a quadratic damping term, and a random forcing function based on a specified spectrum with given significant waveheight and mean period. A sinusoidal forcing function can be looked upon as a worst case scenario since resonances at a particular frequency are given time to build up.

The maximum amplitude of the sway oscillations found when the 12 d.o.f. numerical model, freely suspended, was subjected to 3 hours of random waves at a mean wave period of 7.8 seconds was found to be 0.667m. Given that the natural period of these oscillations is given as 7 seconds then we can assume (using the analytical solution for equation 5.1) an equivalent forcing amplitude value of

$$A = \max(X)\sqrt{\Delta^2\Omega^2 + \left(\Omega^2-\omega_c^2\right)^2} \qquad 5.2$$

where max(X) is the maximum absolute value of the displacement of the sway motions of the jacket, ω_c is the linear natural frequency of the sway oscillations ($2\pi/7$ rad s^{-1}) and ω the mean forcing frequency ($2\pi/7.8$ rad s^{-1}). When the jacket is lowered over the sleeve, at the position where the time series shown in figures 5.2 and 5.3 were taken, the gap between sleeve and pile is given as 0.697m. We could expect that there will be a bias to one side, so put r_s=0.29m, so this gives $l_s=0.407m$. By rescaling the time and displacement variables in equation 5.1 we can obtain a model comparable to the one studied in earlier sections

$$\begin{gathered} \ddot{x} + d\dot{x} + x = \alpha\cos(\omega t) \quad , \quad b < x < 1 \\ \dot{x} \rightarrow -r\dot{x} \qquad x=1 \;\; or \;\; x=b \end{gathered} \qquad 5.3$$

In this equation an overdot represents differentiation with respect to time. Rescaling has been applied to equation 5.1 in such a way that the right hand stop is at x=1, giving b=-1.403. The forcing frequency in this equation is the normalised frequency $\omega=\Omega/\omega_c$, so the first time series is taken at $\omega=7/6\approx1.667$ and the second at $\omega=7/7.8\approx0.897$. Assume a coefficient of restitution r=0.7 and a linear damping coefficient d=0.1 used in earlier sections. Putting $max(X)=0.65$ in equation 5.2, a value just less than the absolute maximum measured in the full jacket model, gives a forcing amplitude of α=0.4803. We have thus defined a simple one degree of freedom model which captures the fundamentals of the important sway oscillations of the jacket at this crucial stage of the deployment over the template.

Using the numerical techniques described in chapter 2, the solution path of the period one non-impacting solution which exists for small frequencies of this system was followed numerically as the frequency varied, and the results are shown in figure 5.4. The maximum absolute values of the velocity and displacement measured over one period are plotted against the forcing frequency which is varied with all other parameters of the system kept constant. Stable solutions are followed until a bifurcation occurs, where there is a qualitative change in the behaviour of the dynamical system: the unstable solution which continues on from a bifurcating stable one is then followed. The response curves are identical to those of the one sided impact oscillator at the same parameters but with only a stop at $x=1$ until the maximum displacement reaches the position of the second stop at x=-1.403. On examining the behaviour of the comparable one sided COR impact oscillator (see section 4.1.5) then for a forcing amplitude $\alpha=0.4803$ we expect the period one non-impacting solution to lose stability at a "flip type" first grazing bifurcation (as the forcing frequency ω is increased from zero). This is followed by a conventional flip bifurcation at which the unstable period one solution created at the first grazing is restabilised. Numerically this grazing bifurcation is found to occur at $\omega\approx0.72$ (G1) followed by a flip at $\omega\approx0.97$ (F1). The consequence of the loss of stability at the grazing bifurcation G1 is that a chaotic solution develops. The period one orbit which becomes stable again at F1 is impacting only on the right hand stop. The amplitude of the response of this period one, one impact solution increases with increasing ω until part of the orbit reaches the left hand stop at $\omega\approx$ 1.2 (G2). Here, as can be seen in figure 5.4, there is a further "flip type" grazing at which the period one, one sided impacting solution again loses its stability in the transition to a period one unstable solution impacting at both stops. Following the path further, we see a conventional flip bifurcation at $\omega\approx1.4$ (F2) leading to a stable period one solution impacting once at either stop, which disappears at a saddle node bifurcation at $\omega\approx1.9$ (SN1). The two sided impacting unstable solution which meets and annihilates the two sided impacting stable solution at SN1 continues back to a further grazing bifurcation, this time at $\omega\approx1.2$ (G3), where the stable, non impacting solution grazes the right hand stop with decreasing ω. In order for this last bifurcation to occur, there must have been a transition from two sided impacting to one sided impacting solutions along the unstable path between SN1 and G3. The "kink" in this solution path at $\omega\approx$ 1.4 in figure 5.4a can be seen to be the place where this transition occurs from figure 5.4b. Here, an unstable orbit just grazes a stop and remains unstable, so the number and type of solutions does not change, so no bifurcation has occurred.

This whole complicated scenario of conventional and grazing bifurcations tells us much about the overall behaviour of the system. The response curves in figure 5.4 show the unstable solutions which follow on when stable solutions disappear at a bifurcation. Further investigation is needed to discover what solution the system restabilises onto after these bifurcations.

The one degree of freedom model, equation 5.3, is modelling the sway mode of the jacket structure under consideration here. The high degree of freedom, randomly forced model of this physical system was observed to undergo one sided impacts when the mean frequency of the wave forcing was just above the natural frequency of the free sway oscillations, at $\omega \approx 1.1667$. This frequency is between the bifurcations F1 and G2 in figure 5.4, and in this region there is a one sided impacting solution, illustrated in figure 5.5. Figure 5.5a shows a time series of the displacement, x, against time t taken over 15 forcing periods after all transients had been allowed to decay, and figure 5.5b shows the phase plane projection of this stable period one orbit (where velocity is plotted against displacement, i.e. time has been "projected out"). Further numerical investigations (e.g. a cell-to-cell mapping in this region to determine basins of attraction) reveal no other solutions.

At a mean wave frequency of $\omega=0.897$, just below the natural frequency of sway oscillations of the jacket structure, the 12 degree of freedom model was observed to be undergoing two sided impacts with much higher loads at the piles. This frequency is in the range between the bifurcations G1 and F1. The stable non-impacting period one orbit loses stability at the flip type grazing bifurcation G1 and then regains stability at the conventional flip bifurcation F1. At $\omega=0.897$ there is no stable period one orbit for the system to fall on to. A cell-to-cell mapping at this parameter set shows that two period two solutions exist, and the basins of attraction of these solutions are shown in figure 5.6. These two period two solutions are illustrated in figures 5.7 and 5.8. As in figure 5.5, figures 5.7 and 5.8 show the steady state time series over 15 forcing periods and the phase plane projections of the stable solutions. Figure 5.7 shows the steady state solution associated with the large, white basin of attraction in figure 5.6. This is seen to be a period two, two sided impacting motion. Figure 5.8 shows the steady state solution associated with the much smaller, black basin of attraction, which again repeats after two periods, but only undergoes impacts on one side. In a random forcing environment centred around these parameters we would expect the two sided solution to dominate since its basin of attraction is much larger. This is indeed the type of behaviour observed in the 12 d.o.f. model of Robinson & Ramzan for the jacket/pile interaction (figure 5.3), i.e. a large amplitude, two sided behaviour dominates with occasional bursts of smaller amplitude one sided impacting behaviour.

In the previous section we described the results obtained from following the unstable solution paths which continue on from stable ones after a bifurcation of the system, equation 5.3. If instead we allow the system to slowly evolve and thus fall onto another stable solution after bifurcation we obtain the bifurcation diagram, figure 5.9. This figure shows the bifurcation diagram obtained by starting with initial conditions on the stable period one, one sided impacting orbit which exists at $\omega=1.2$ (see figure 5.4) and slowly decreasing the frequency. The force at the impact is shown plotted against the forcing frequency, ω, since it is the pile load which is the important limiting quantity in the docking of the jacket structure over the piles. We see that the stable, period one, one sided impacting solution is followed with the response (force at the right stop) fairly constant, until F1 at $\omega \approx 0.97$ where there is a supercritical flip bifurcation. The period two solution which results from this bifurcation grows rapidly in size until it impacts also against the left hand stop. At this point there is a further grazing bifurcation and the amplitude of the forces at the stops becomes around twice as large. An orbit on the path of this large amplitude, two sided impacting motion is illustrated in figure 5.7. Below this, beyond the parameter region of interest for this particular problem, there are many further bifurcations, leading eventually to the final (flip type) grazing bifurcation at which an unstable period one impacting solution bifurcates to leave a period one, stable non-impacting solution at G1.

Above we have described the results of numerical investigations of a simple model of an impact oscillator designed to be comparable to the sway oscillations of a particular jacket/pile interaction problem. It has been shown that the behaviour observed from a much larger model including all of the modes of oscillation, and subject to "realistic" forcing functions can be reproduced and explained in terms of bifurcations of the simple one degree of freedom nonlinear system, equation 5.1. The advances in the understanding of grazing bifurcations described in previous chapters mean that the results obtained above can be interpreted correctly, with the effects of both grazing and conventional bifurcations understood and appreciated. It is not suggested that these ideas can replace the comprehensive modelling of complex engineering systems, but rather, once possible problems have been identified using such large models, then more detailed studies of a simplified dynamical system containing the essential elements can be performed. One advantage of this approach is the ease with which parametric studies can be performed to identify which parameter sets are safe and which unsafe. With the more complicated models, computer power and time limitations mean that often only a few parameter settings can be investigated, and so important jumps to resonant solutions could be missed altogether.

Figure 5.1 Typical pin/sleeve docking arrangement (from Robinson and Ramzan, 1988).

Figure 5.2 Time series of docking pile and jacket motions in a sea state with significant wave height Hs=2m, mean period T=6s (taken from Robinson and Ramzan, 1988).

Figure 5.3 Time series of docking pile and jacket motions in a sea state with significant wave height Hs=2m, mean period T=7.8s (taken from Robinson and Ramzan, 1988).

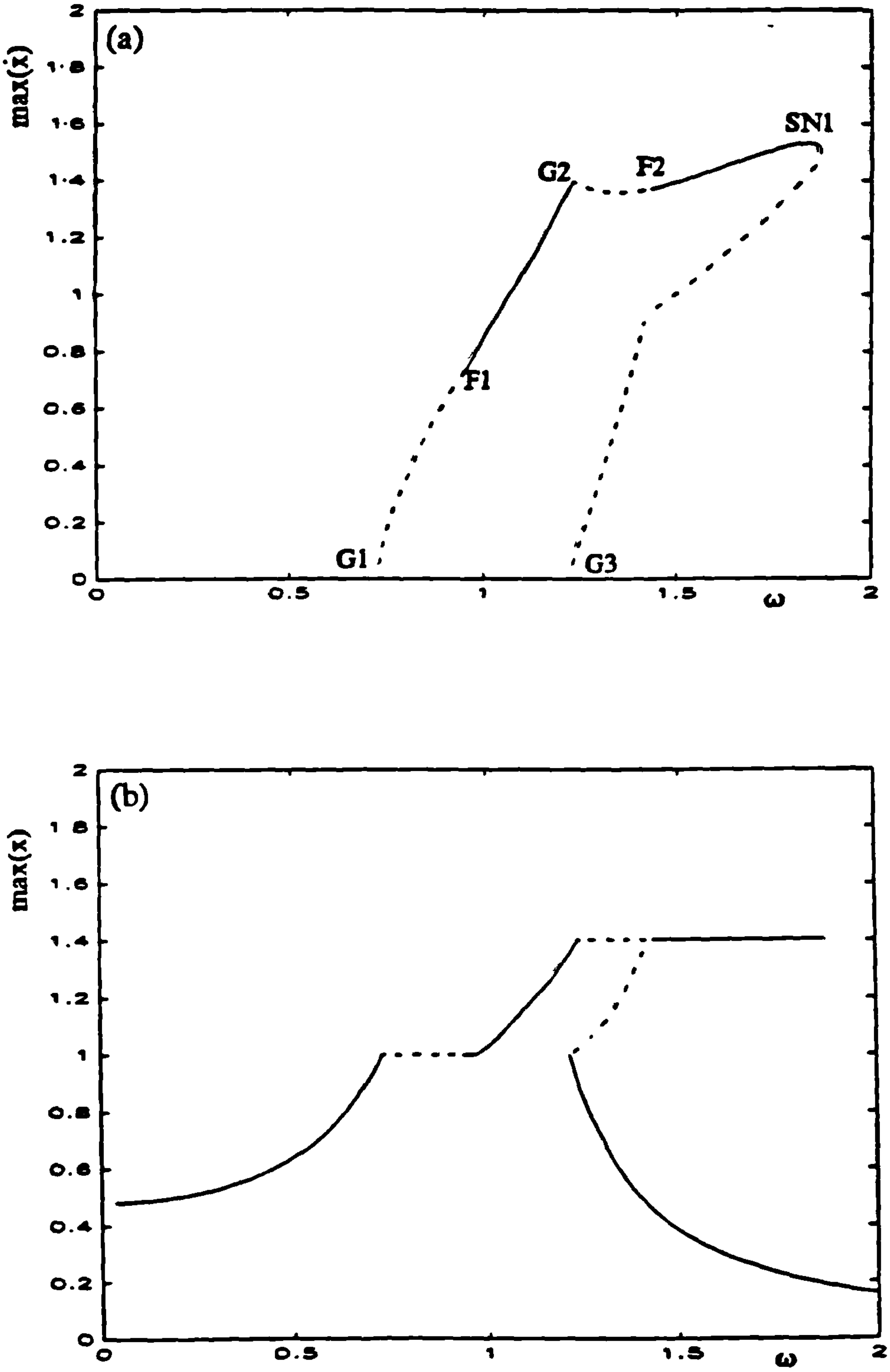

Figure 5.4 Frequency response curves for equation 5.3, $\alpha=0.4803$, $d=0.1$, $r=0.7$, $b=-1.403$. (a) Shows maximum velocity, $\dot{x}$ against forcing frequency, ω, (b) shows maximum displacement x against ω for period one solutions. Solid lines represent stable solutions, dotted lines unstable. G1, G2 and G3 are grazing bifurcation events, F1 and F2 are flip bifurcations and SN1 is a saddle-node.

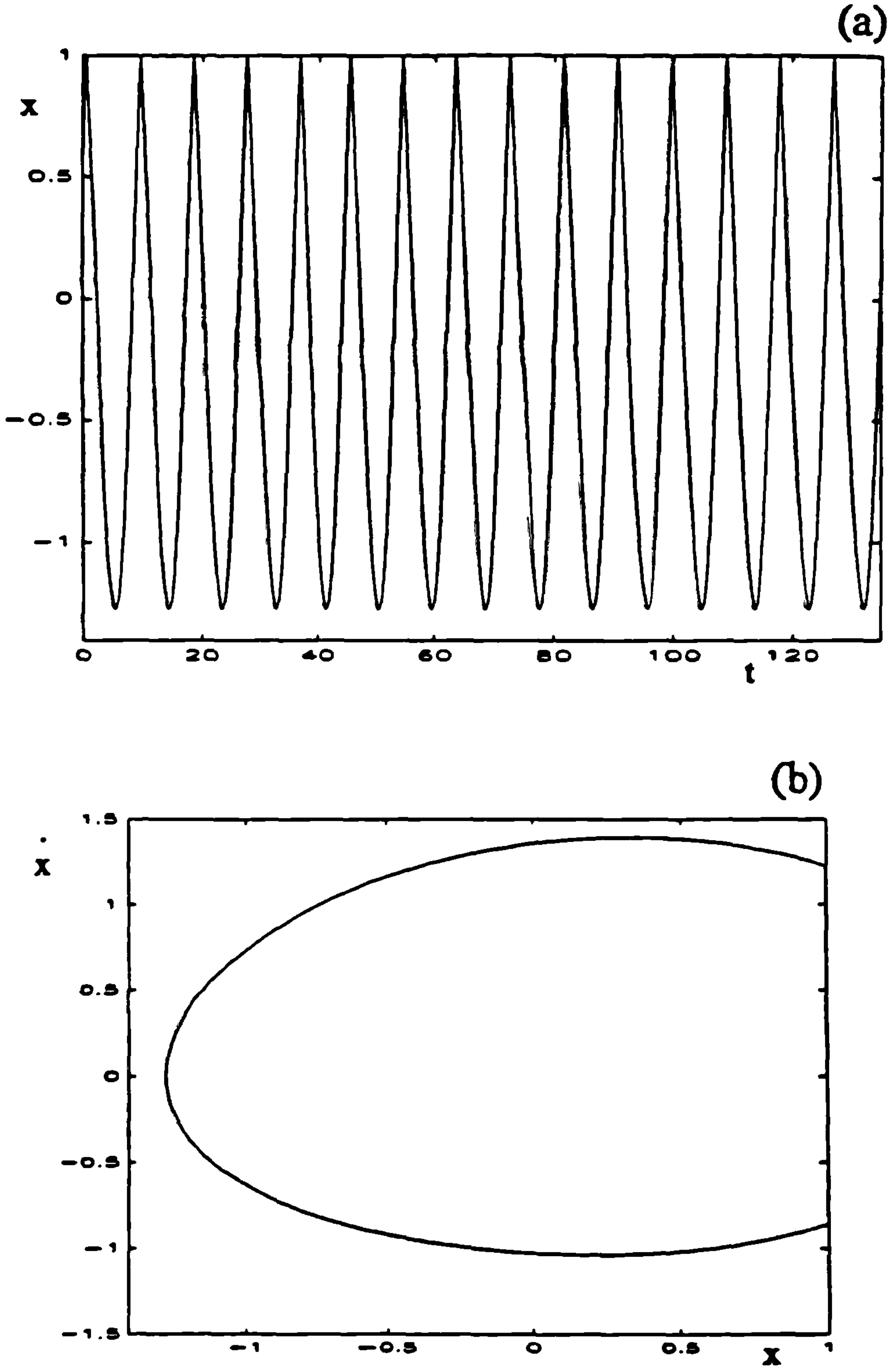

Figure 5.5 Illustrations of (a) 15 periods of the time series x against t and (b) the phase plane projection, ẋ against x, for one sided impacting stable period one orbit of equation 5.3, parameters as figure 5.4, ω=1.667.

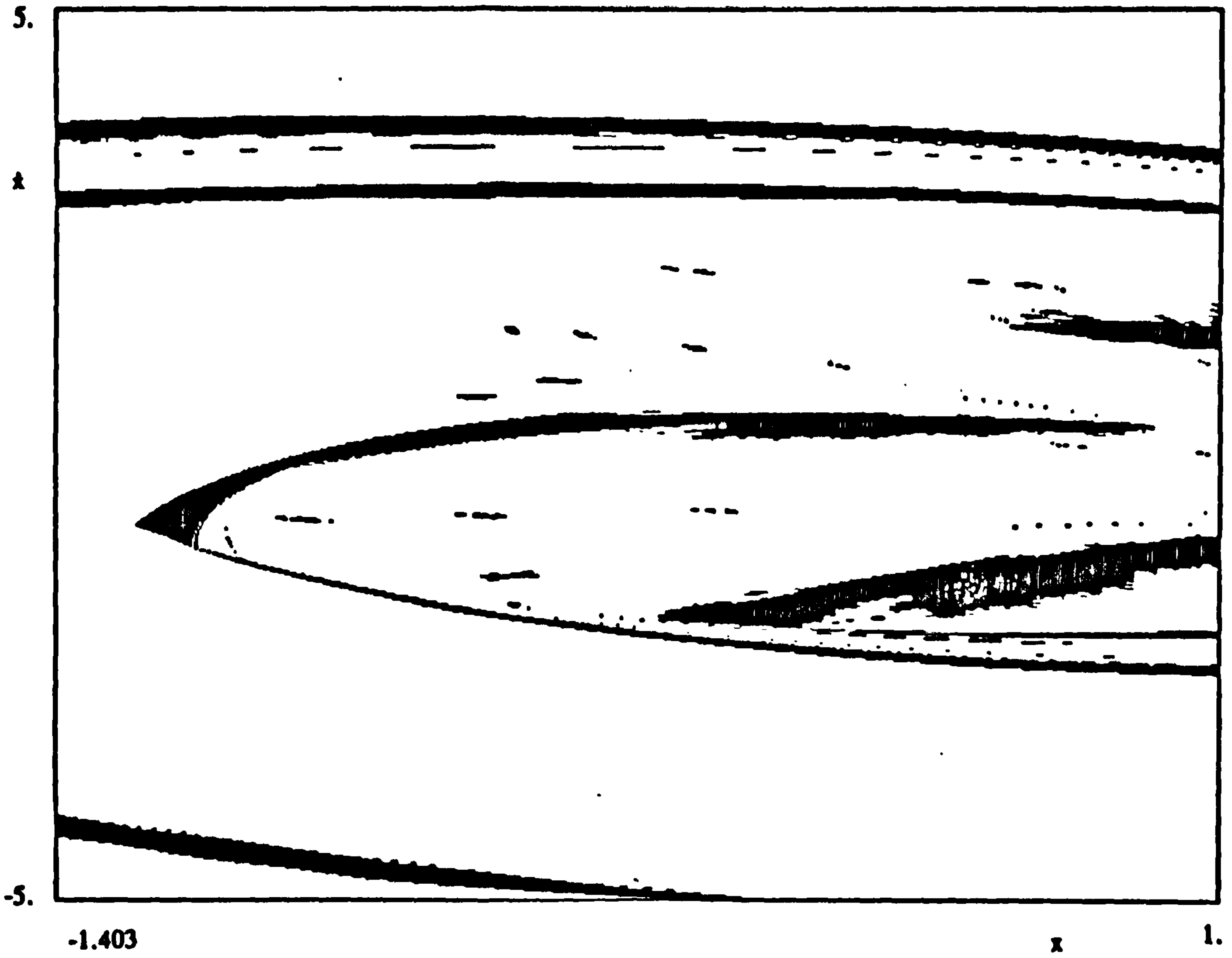

Figure 5.6 Basins of attraction for equation 5.3, parameters as figure 5.4, $\omega=0.897$. The white area corresponds to the orbit shown in figure 5.7, the black area to the orbit shown in figure 5.8.

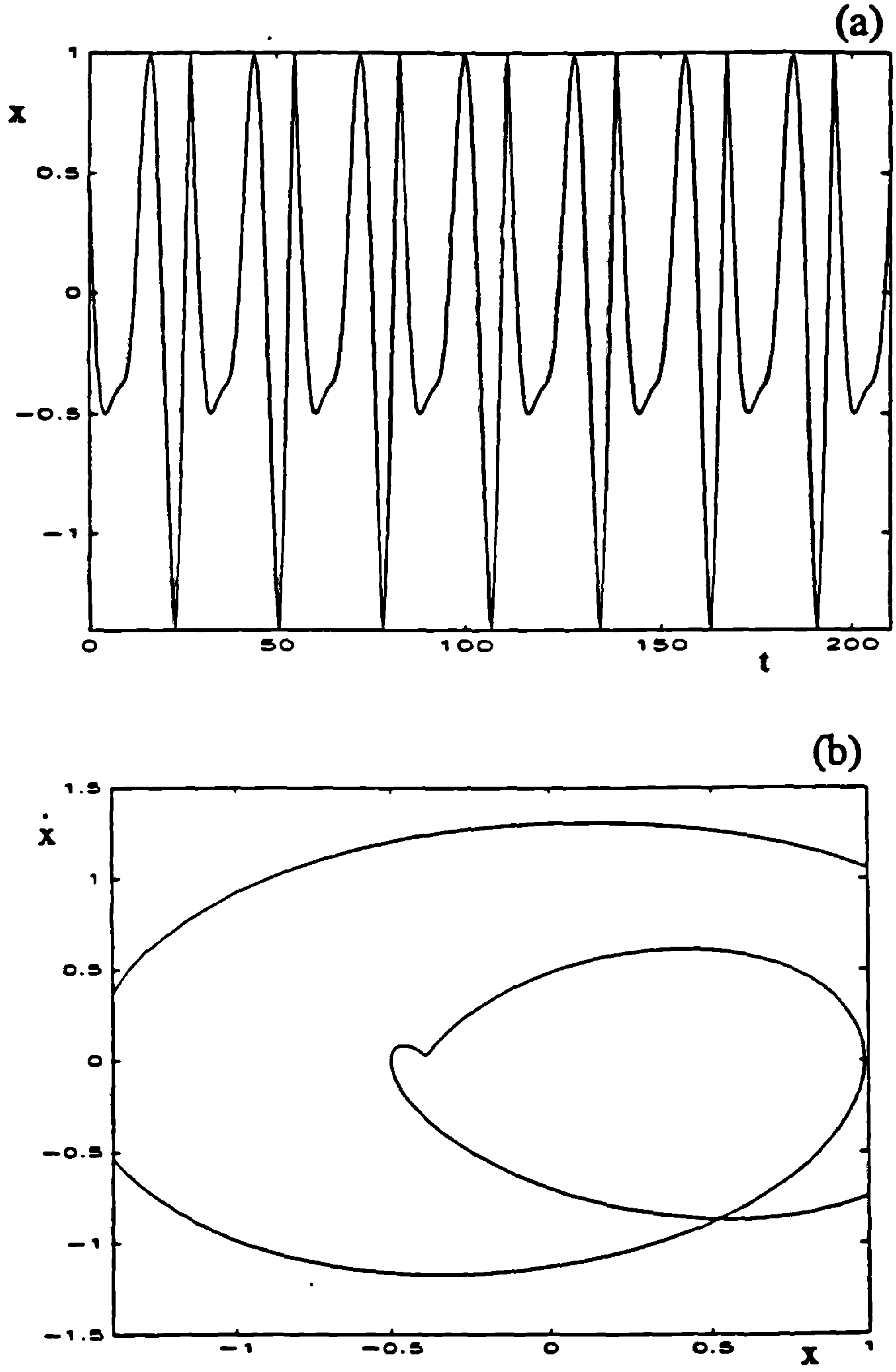

Figure 5.7 Illustrations of (a) 15 periods of the time series x against t and (b) the phase plane projection, $\dot{x}$ against x, for two sided impacting stable period 2 orbit of equation 5.3, parameters as figure 5.4, $\omega=0.897$.

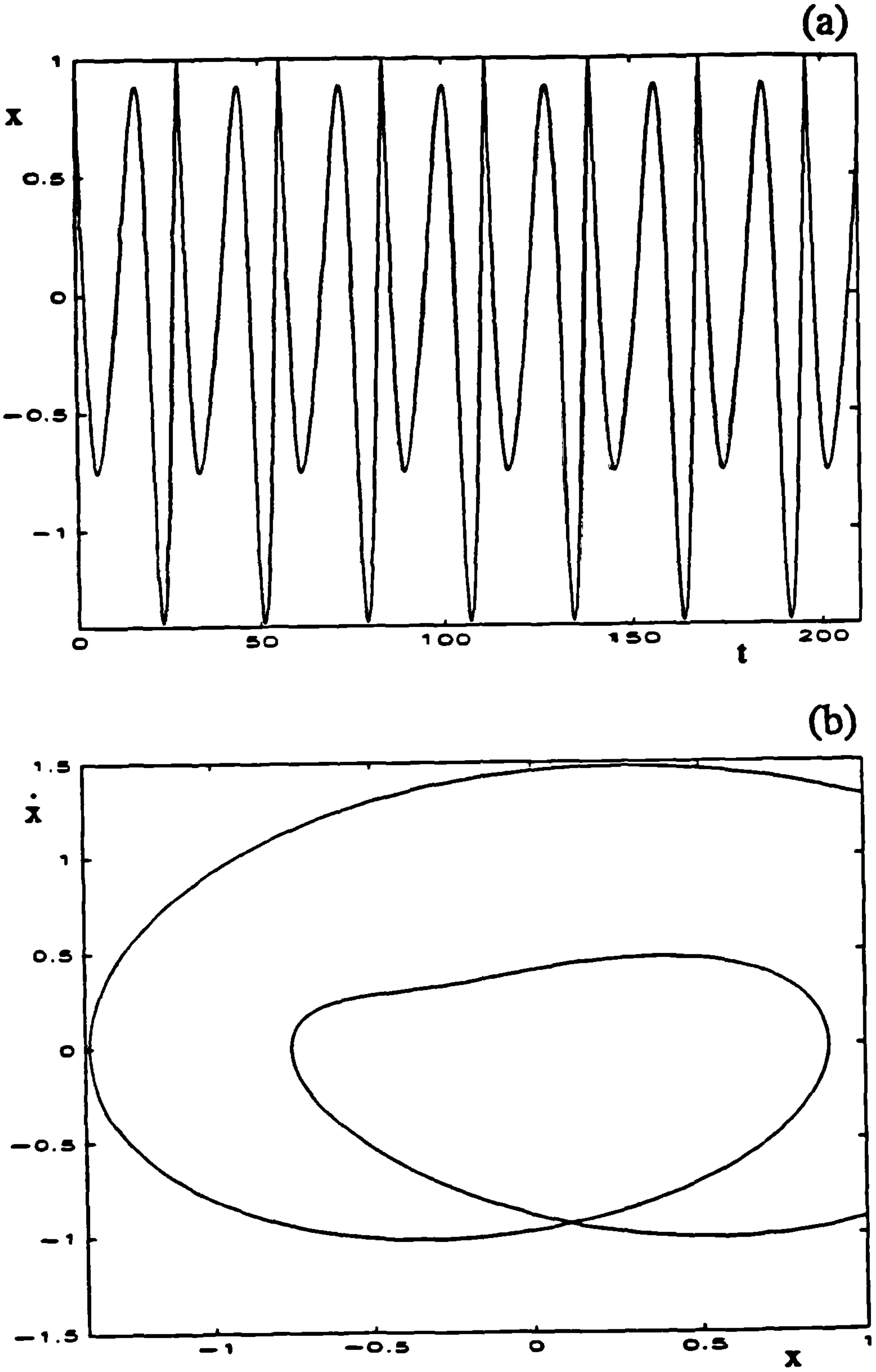

Figure 5.8 Illustrations of (a) 15 periods of the time series x against t and (b) the phase plane projection, $\dot{x}$ against x, for one sided impacting stable period 2 orbit of equation 5.3, parameters as figure 5.4, ω=0.897.

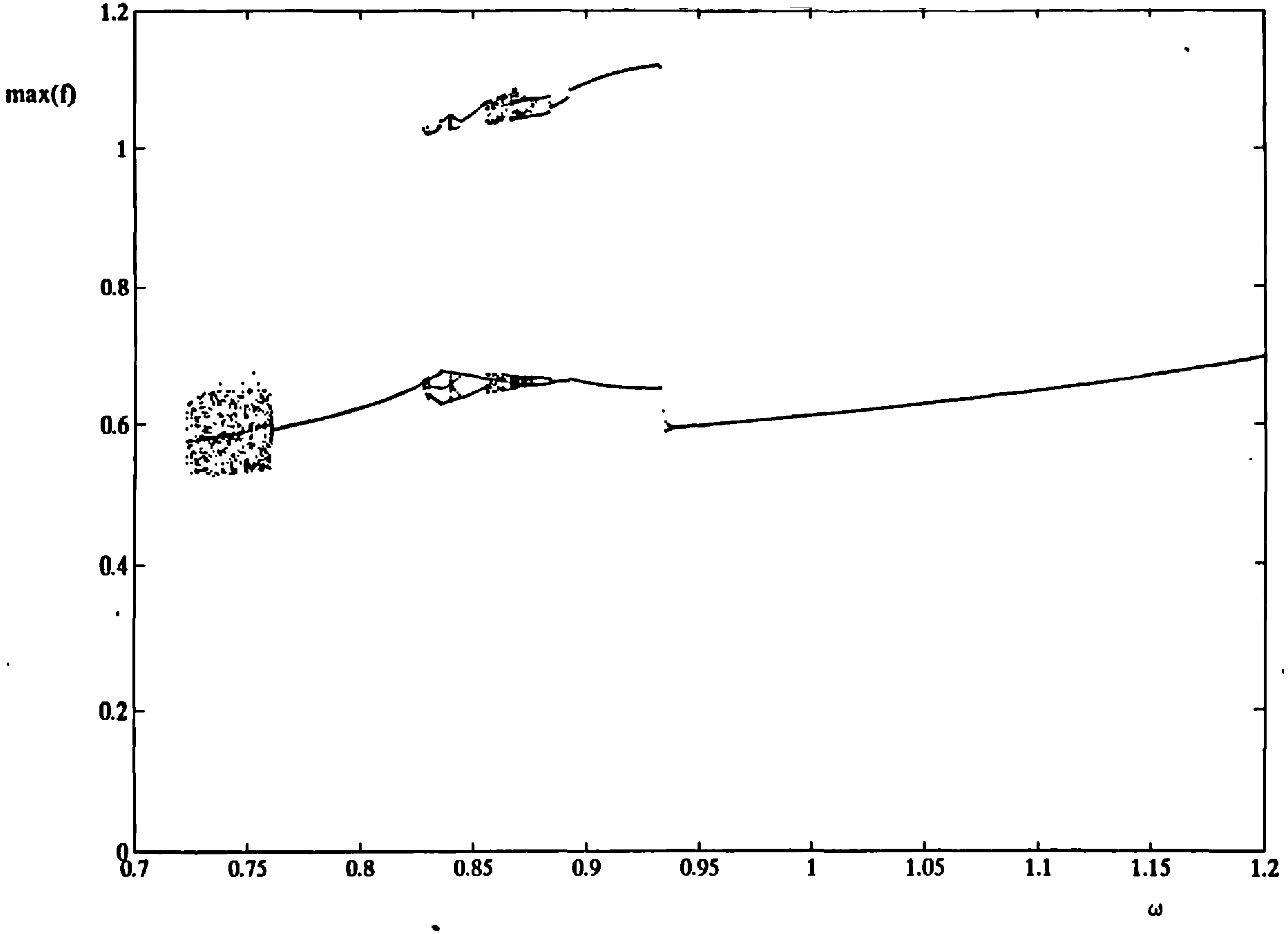

Figure 5.9 Bifurcation diagram showing maximum force exerted by the stop at impact, max(f), against forcing frequency ω for equation 5.3, parameters as figure 5.4, as ω is slowly decreased.

6. Experimental studies of an impact oscillator

6.1 Introduction

Several experimental studies of impact oscillators have been carried out. Moon and Shaw [1983] investigated the chaotic vibrations of a beam with impacts at a stop, and compared the experimental results with a piecewise linear model obtained from a Galerkin approximation using only the first mode. Poincaré maps and fourier transforms of chaotic motions from the experiment and from the theoretical model were compared, and found to agree reasonably well. Stensson and Nordmark [1992] used a vibrating spring/mass system with impacts at a stop and compared this experimental setup with a simple coefficient of restitution theoretical model. Bifurcation diagrams and chaotic attractors in Poincaré maps obtained from numerical simulations of the model and from the experiment were compared. Some of these results showed a remarkable agreement The main concern of the present work has not however been addressed in previous experimental studies. The grazing bifurcations which are found to occur in the COR model when an orbit undergoes an additional low velocity impact seem to be very important to the overall bifurcational behaviour of an impact oscillator. In chapter 4 it was shown that even when the discontinuous coefficient of restitution impact rule is replaced by a continuous and differentiable stiffness function which rises rapidly at impact to oppose the motion (the Hertz law model), the qualitative bifurcational behaviour appears to be the same. In this chapter an experiment is described which is devised in order to test whether the qualitative bifurcational behaviour of the COR model and an experiment with one sided impact are the same.

6.2 Experimental setup

Figure 6.1 shows a diagram of the experimental setup used A long, slender steel beam is attached to a metal base at one end. At the other, free end of the beam there is an electromagnet which is used to force the beam, a proximity probe to measure the displacement of the beam and a steel pin which acts as a stop. The pin is attached to a micrometer and so can be moved towards the beam or away from it, and the distance from the stop to the beam can be measured A microcomputer with an analogue to digital / digital to analogue converter (ADC/DAC) card is used both to drive the electromagnet with some waveform and to read the voltage from he proximity probe. Some of the specifications of the experimental setup are given below.

Beam:

Length : 300mm
Width : 30mm
Thickness : 2mm

ADC/DAC (National Instruments LAB-PC) :

Input voltage range : ±5v
Maximum sampling rate : 62500 Hz
Analogue input resolution : 12 bits (1 in 4096)
Output voltage range : ±5v
Maximum waveform update rate: Approx. 200000 points/sec
Analogue output resolution : 12 bits (1 in 4096)

A piece of software has been custom written to drive the electromagnetic forcer and take readings from the proximity probe. A continuous sine wave function of a given frequency and amplitude is sent to the output channel. A range of frequencies is chosen and the software steps through this range of frequencies, allowing 30 seconds at each step for any transient motions to decay. The ADC is then used to acquire 10000 readings of the voltage at the proximity probe at a rate of 10000 Hz, i.e. one second of data. Since the DAC uses a separate clock on the ADC/DAC card to the ADC, the two functions of waveform generation and data acquisition can take place simultaneously. The maximum absolute voltage in this one second is acquisition period is recorded and the timebase for waveform generation is then altered to start the DAC generating the waveform at the next frequency. After a further 30 seconds another reading is taken, and so on. When the end of this range of frequencies is reached the process is reversed so that a frequency sweep is performed in the opposite direction.

There is a good linear relationship between the voltage measured from the proximity probe and the displacement of the beam as measured by the micrometer which the stop is attached. At each of the locations of the stop at which readings were taken, the amplifier from the proximity probe was adjusted until the voltage recorded with the beam in its equilibrium position was zero : this allowed for the correction of any small drift of the instruments over time. The beam was then held down on to the stop and the resulting steady voltage recorded. In figure 6.2 the recorded voltage v (volts) is plotted against the measured distance to the stop d_s (mm) , along with the best least squares fit given by the model $v=\lambda d_s$, where the fitted parameter $\lambda=2.01$ v mm^{-1}.

6.3 Frequency sweeps with no stop

In order to give a good comparison with the theoretical models investigated in the previous chapters it is required that the beam on its own should have a linear frequency response curve. To achieve this as nearly as possible we excite the beam at a frequency near to the natural frequency of the first mode. The amplitude of the forcing is also chosen so as to be small enough that the beam is not forced into a region with nonlinear response characteristics. With the stop well away from the beam, three frequency sweeps were carried out. In this way it is confirmed that the frequency response curves of the beam alone are very close to linear. Preliminary studies had indicated a natural frequency around 28Hz, so the frequency range chosen was 25.9Hz to 30.3Hz and in each case a sweep up in 56 equal steps and down in 55 equal steps was performed. The parameters of the beam can then be estimated from this experimentally obtained frequency response curve. We are assuming that only the first linear mode is being excited, and further assume that there is linear damping of the beam. The idealised equation describing the motion of a point along the beam (when no stop is present) is then

$$\ddot{x} + \Delta\dot{x} + \omega_0^2 x = A\cos(\omega t) \qquad 6.1$$

where an overdot represents differentiation with respect to time t, Δ is the linear damping coefficient, ω_0 the natural frequency and A the forcing amplitude after the mass has been scaled out, and x is the displacement of the beam from the stop in mm. The asymptotic steady state solution of this equation is $x=(A/\gamma)\cos(\omega t)$, where $\gamma=((\Delta\omega)^2+(\omega^2-\omega_0^2)^2)^{1/2}$. The maximum absolute value of the displacement is therefore A/γ. By performing a nonlinear minimisation on the function

$$S=\sum_{i=1}^{i=N}\left[r_i-\frac{A}{\gamma(\omega_i)}\right]^2 \qquad 6.2$$

with respect to the three parameters Δ, A and ω_c we can estimate the best fit to the model 6.1 for the experimental data set (r_i, ω_i), $i=1,2,..,N$ where N is the total number of data points and r_i is the maximum displacement of the beam (measured in volts from the proximity probe) at the frequency ω_i. The simplex search method of minimisation was used to obtain the results in the table below

Run number	A (mm s^{-2})	ω_c (rad s^{-1})	Δ (s^{-1})	Total number of points
1	1.410	176.19	0.0775	111
2	1.430	176.19	0.0777	111
3	1.489	174.09	0.0992	111

Diagrams 6.3a-c show the data and fitted curves for runs 1 to 3. The assumptions that the beam is governed by the linear stiffness, linear damping model 6.1 are confirmed by the good fit to the data in runs 1 and 2. Run 3 appears to be very noisy at the lower frequencies and so is discarded. Runs 1 and 2 agree well with one another, so we can estimate the parameters of the equivalent linear system as :

Forcing amplitude A : 1.420 mm s^{-2}
Natural frequency ω_c : 176.19 rad s^{-1}
Damping coefficient Δ: 0.0776 s^{-1}

6.4 Frequency sweeps with impact

Since the parameters A, ω_c and Δ have been fitted to the linear model given by equation 6.1, the free parameter which is altered in the experiment is the position of the stop. Six runs were made with the stop at different positions. At the beginning of each run the voltage measured at the proximity probe with no external forcing applied was zeroed and then the beam held down on to the stop and the measured resulting voltage noted. This, along with the distance measured by the micrometer, were used to show the linear relationship between distance and measured voltage shown in figure 6.2. Three frequency sweeps up and down for each position of the stop were then performed, with the maximum displacement at each frequency being recorded as described for the case with no stop. The three runs for each position of the stop were averaged. From these experimental averaged frequency response curves the positions of three bifurcational events were estimated for each position of the stop. These bifurcations are : first grazing where the amplitude of response first reaches the displacement of the stop as frequency is increased and the response curve flattens out; second grazing where the amplitude of response first reaches the displacement of the stop as frequency is decreased ; saddle-node bifurcation where the impacting solution loses its stability as the frequency is increased. The results of the experimental runs with the stop are summarised in the table below.

Run number	Measured displacement of stop (volts)	Measured displacement at stop (mm)	Frequency of first grazing (rad s^{-1})	Frequency of second grazing (rad s^{-1})	Frequency of saddle node (rad s^{-1})
1	0.09	4.65	171.53	179.07	186 42
2	0.17	4.60	173.98	177.81	184.79
3	0.26	4.55	174.99	177.37	182.65
4	0.40	4.50	175.43	176.56	188.43
5	0.49	4.45	175.99	177.06	180.52
6	0.61	4.40	175.87	176.49	180.14

6.5 Comparison of experimental and theoretical results

Figure 6.4 shows a typical response curve for run 4 along with the numerically calculated theoretical response curve assuming a coefficient of restitution model with the parameters calculated from the linear response curves (the runs with no stop). There is still one parameter which remains to be estimated : the coefficient of restitution, *r*. In figure 6.4 we have chosen to have $r=0.2$ which is quite a low value (Goldsmith [1960] gives the coefficient of restitution between steel and steel as somewhere between 0.7 and 0.8). Despite the good fit between the runs with no stop and a linear response curve (figure 6.2), confirming that predominantly only one mode is being excited, once a stop has been imposed there is a possibility of other modes being excited. The coefficient of restitution must be made small in order to account for the energy which is being transferred to these higher modes at each impact. There is a good qualitative agreement between the frequency response curves obtained experimentally and the theoretical response curves. For each position of the stop the response curve flattens out after the first grazing as the frequency is increased from below the ω_c, the natural frequency of the first linear mode. The small increase in maximum absolute displacement after the first grazing belies the greatly increased velocity with which the beam hits the stop. With the simple experimental apparatus used here it was difficult to measure velocities (the direct measurement of displacement was not clean enough to differentiate for the velocity). However, just by ear it was possible to tell that the severity of impacts at the stop was increasing, with the loudest "ringing" of the beam against the stop occurring just prior to the saddle-node bifurcation event which occurs when the impacting state disappears as the frequency is increased, leaving the system to settle on a low amplitude non-impacting state. The frequency response curves for the coefficient of restitution model bear out this observation. Although the maximum displacement of the response increases only very slowly after the first grazing until the final saddle-node bifurcation, the velocity at the stop (the impacting velocity) increases quickly after first grazing. The velocity at impact in the theoretical model increases until just before the final saddle node bifurcation where the period one, one impact per period solution is destroyed.

A more detailed comparison between the bifurcational behaviour of the theoretical and experimental models is made in figure 6.5 where the positions in parameter space (position of stop vs forcing frequency or d vs ω) of the various bifurcations listed in the above table are shown. For a given forcing frequency, a grazing bifurcation will occur if the maximum amplitude of the response with no impacts is equal to the position of the stop, $x=d$. The locus of grazing bifurcations in d vs ω parameter space then is given by

$$d = \frac{A}{\sqrt{(\Delta\omega)^2 + (\omega^2 - \omega_c^2)^2}} \qquad 6.3$$

The location of the saddle-node bifurcations in this parameter space for the theoretical model with the fitted parameters can be calculated for a given coefficient of restitution using the explicit expressions for the eigenvalues of the first differential matrix of the impact map given in section 3.74 (with suitable rescaling). The loci of saddle-node bifurcations for a range of values of the coefficient of restitution r is plotted in figure 6.5. Clearly a very low coefficient of restitution is required for the theoretical curve to lie near to the experimentally observed one.

6.6 Conclusions

The overall qualitative behaviour of a one sided impact oscillator modelled using a simple coefficient of restitution rule to model the impact appears to agree well with the results of the experiments using an electromagnetically excited beam described above. In particular, the bifurcations which are predicted by the theory (including both the conventional, smooth bifurcations and the "new" grazing bifurcations), and which determine the overall shape of the frequency response curve, are found experimentally. It is clear that the grazing bifurcations which have been the subject of study of much of this project play an important part in the overall dynamical response of an impact oscillator.

Figure 5.1 Typical pin/sleeve docking arrangement (from Robinson and Ramzan, 1988).

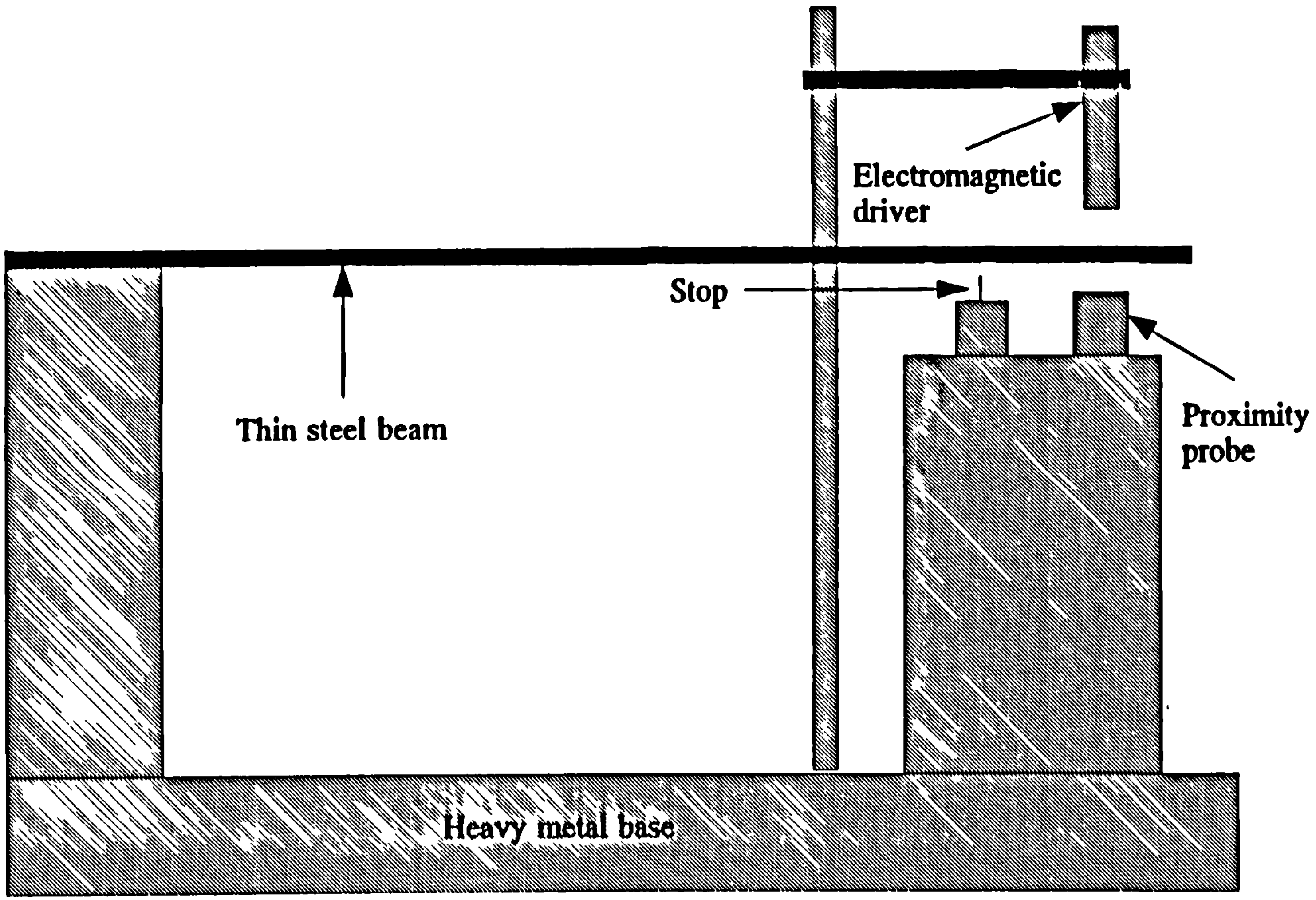

Figure 6.1 Diagram of the experimental apparatus

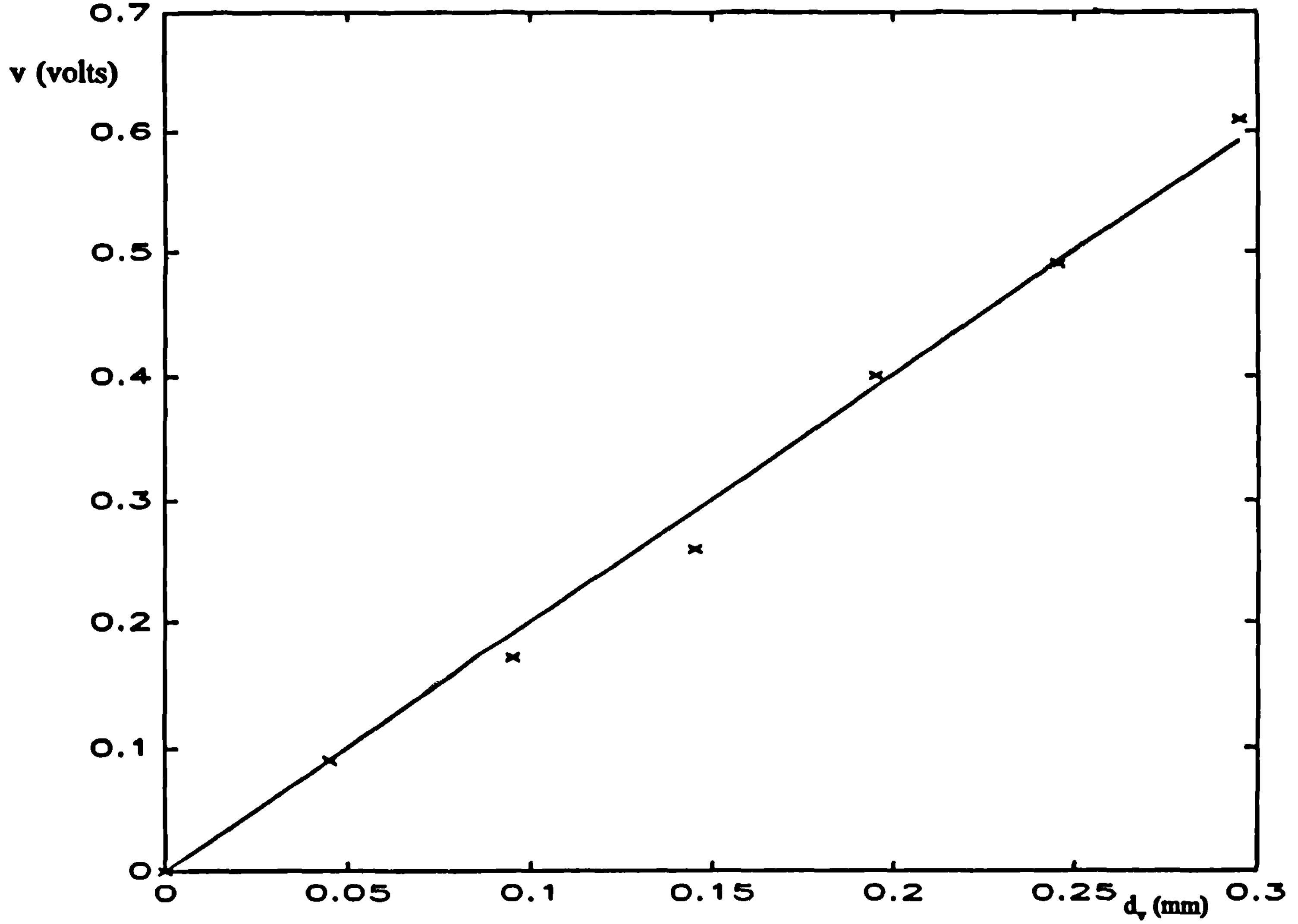

Figure 6.2 Plot of static readings (crosses, x) of measured voltage, v (volts), against measured distance from the stop, d_v (mm). The solid line is the fitted best straight line.

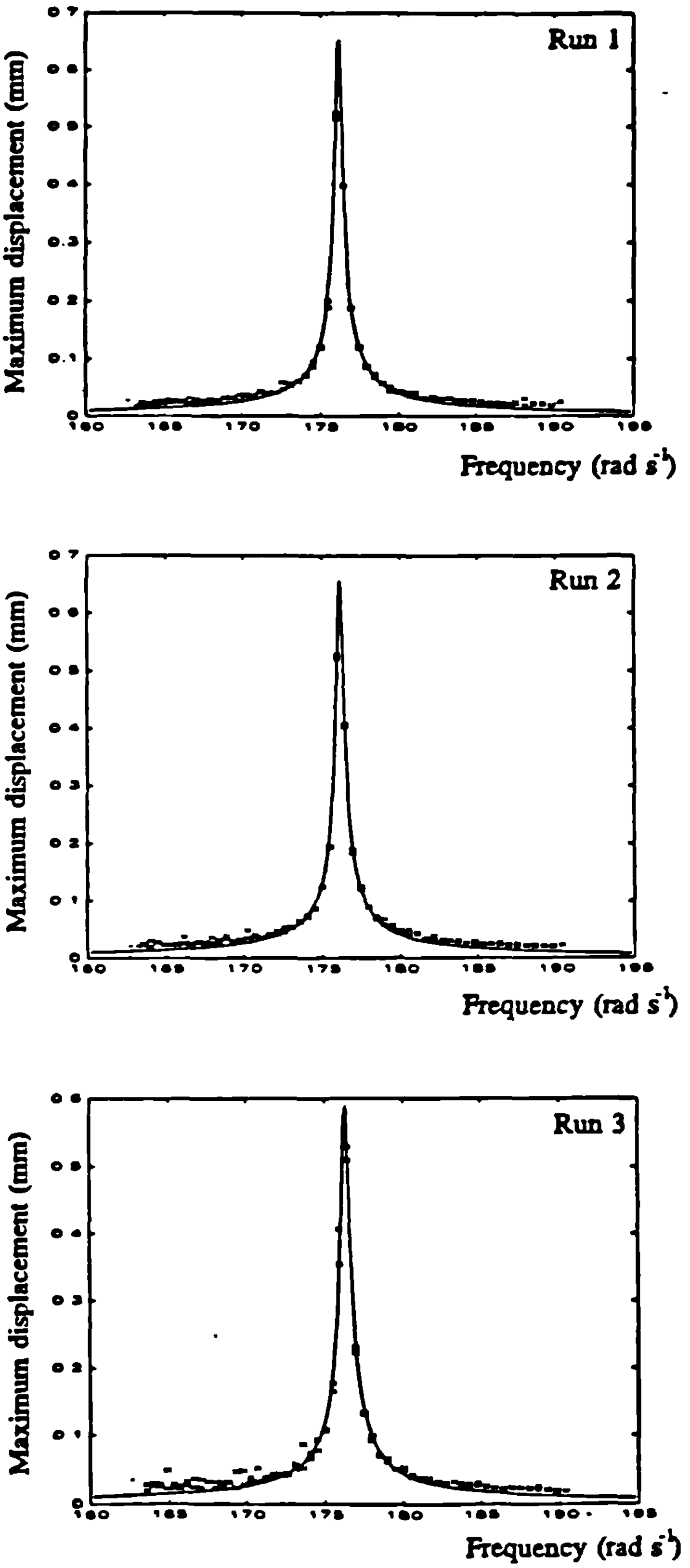

Figure 6.3 Three experimental frequency response curves (crosses , x) and their correspondin fitted "ideal" linear response curves (solid lines).

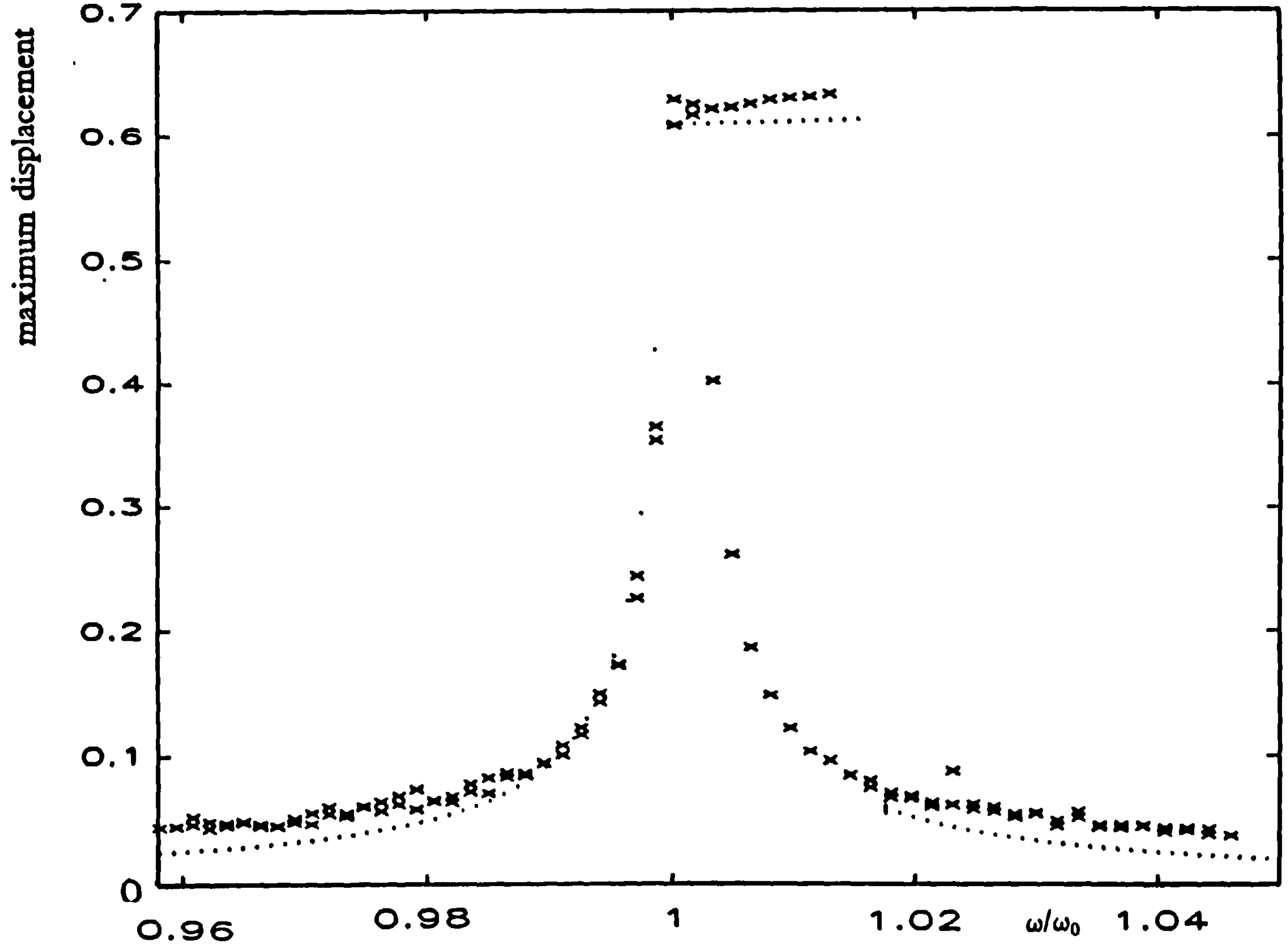

Figure 6.4 Response curves for experimental run 4. Crosses (x) show the averaged experimentally measured responses over three runs, dots (.) show the numerically determined maximum response for the theoretical model, equation 6.1.

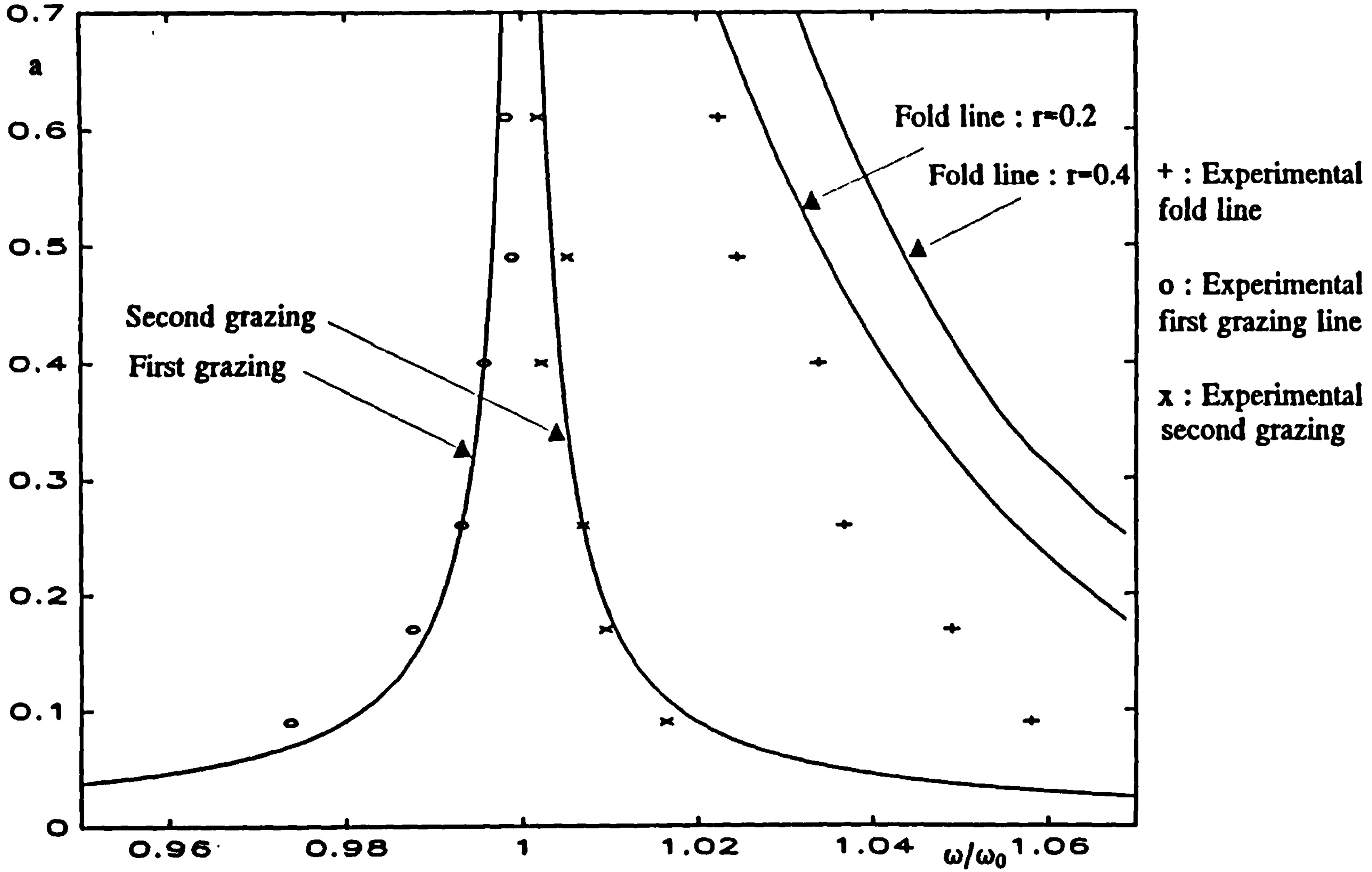

Figure 6.5 Experimental and theoretical bifurcation locus diagram for an impact oscillator. Shown are the theoretically calculated first grazing locus, the second grazing locus and the saddle-node, fold loci for r=0.2 and r=0.4, plus the estimated experimental values.

7. Conclusions

A wide variety of physical systems undergo intermittent contact with motion limiting stops under the influence of some external forcing. These impact oscillators have been frequently studied in the light of a particular physical application, some examples of which are given in the references in section 1.1.2. A common approach taken in these studies is a parametric study, in which the parameters of interest in a mathematical model of the physical system are varied, and in this way parameter regions of "acceptable" behaviour are found. More systematic studies of nonlinear dynamical systems concentrate on the bifurcations at which qualitative changes in the system dynamics occur. In this way, for example, parameter sets at which bifurcations which lead to jumps to "dangerous" types of motion can be located. The classification of bifurcations and the behaviour they lead to in a dynamical system are therefore of great interest. Impact oscillators are often modelled using the simple coefficient of restitution (COR) rule to instantaneously reverse velocity at an impact. Complicated dynamics can arise due to the non-smooth nature of the resulting dynamical system. In particular, types of local co-dimension one bifurcation not found in smooth dynamical systems can occur, called *grazing bifurcations.* In this thesis we have sought to show the types of grazing bifurcation which can occur, and also to answer the important question of how these bifurcations relate to smooth bifurcations. If we model an impact oscillator with a smooth formulation, we would expect that the overall behaviour of the two similar systems would be the same.

It was shown in section 3.5 that the reduction of the flow of a continuous time COR impact oscillator to a discrete Poincaré map can result in that map being discontinuous. Both the stroboscopic map, in which the displacement and velocity of the impact oscillator are sampled once every forcing cycle (at the beginning, say) and the impact map, in which the time and velocity are sampled at an impact, are shown to be discontinuous. The stroboscopic map is discontinuous due to the instantaneous reversal of velocity at the stop imposed by the COR rule, whereas the impact map is discontinuous due to the lack of transversality of the chosen surface of section. More serious to the overall dynamics of the COR impact oscillators are the discontinuities in gradient which are apparent in any Poincaré map. It is demonstrated in section 3.6 that there is a square root singularity in the gradient of a map at any point which, if the flow line through it were followed, would just touch a stop with zero velocity before intersecting again with the surface of section. Since there is a line of points along the stop with zero velocity in a one degree of freedom impact oscillator, then there will in general be a line of discontinuity in gradient in the Poincaré map (we can see this just by following the flow lines through the line of zero velocity at the stop backwards in time to the surface of section). As a system parameter is varied, the position of a stable fixed point of the one parameter family of maps will vary. If at some parameter value the stable fixed point comes to lie on a line of discontinuity in gradient then this parameter value is one at which the map has become structurally unstable. The square root singularity on the impact side of the line ensures that a stable fixed point cannot exist on this impact side, but can exist on the other side of the line. This event we have called a *grazing bifurcation*. It is most useful to think of these grazing bifurcations taking place in any map other than the impact map, since in the impact map a line of discontinuity and of discontinuity in gradient coincide at the line of zero velocity. By choosing for example the stroboscopic map it becomes clear that the grazing bifurcation events occur because of fixed points crossing the line of discontinuity of gradient.

In chapter 4 we studied the grazing bifurcation event in COR impact oscillators by concentrating on the simple case of a sinusoidally forced one degree of freedom system with linear damping and linear stiffness characteristics away from the stops. To further simplify matters we concentrated on the first grazing bifurcations, that is bifurcations between a stable, non impacting limit cycle and a steady state impacting limit cycle with one impact. Both of these steady states can be located analytically using the methods shown in chapter 3, along with their stability characteristics. It is shown that the impacting solution is unstable as the velocity at impact tends to zero, whereas the non-impacting steady state solution is always stable since it is just the asymptotic steady state of a linear oscillator. Further, we have shown that the impacting solution approaches the non-impacting solution (i.e. stable solution meets unstable) as the parameter is moved towards that at which first grazing occurs. Two situations corresponding to two different types of grazing bifurcation are possible. The unstable periodic orbit can approach the stable one either from above or below as a parameter is varied. If both stable and unstable steady states approach one another from below, they then annihilate one another at the critical first grazing parameter. In the other case, the saddle solution "continues on" from the stable solution. We call these bifurcations saddle-node type and flip type grazing bifurcations respectively, since these are similar smooth bifurcations. Following a saddle-node type grazing there is no nearby solution and the system will restabilise onto a distant attracting solution. After a flip type grazing, however, numerical evidence has shown that there is apparently an immediate jump to a chaotic attractor. It is also numerically observed that a different impact oscillator model, the Hertz law model, which does not suffer from the continuity problems of the COR model, does indeed undergo saddle-node bifurcations and flip bifurcations (the start of a period doubling cascade to a chaotic solution) near to their grazing bifurcation counterparts. Analogous one dimensional maps of the interval, with a square root singularity in gradient, are also shown to exhibit similar behaviour, including an immediate jump to a chaotic solution. We also manage to find analytically some co-dimension two bifurcations which occur when the first grazing bifurcation changes at a point from flip type to a saddle-node type grazing. It appears from this work that saddle-node and flip type grazing bifurcations can be seen as discontinuous equivalents to their smooth counterparts. In the case of the flip type grazing bifurcation, a whole period doubling cascade appears to have been compressed to a point. A similar phenomenon is seen in Nordmark [1993] in which the shape of a chaotic attractor in a smooth model of an impact oscillator approaches the shape of the chaotic solution of the COR impact oscillator at the same parameter values as the severity of the impact is increased.

There are many further questions, not addressed in this thesis, which can be asked about grazing bifurcations. For example, given the observation that a chaotic solution arises immediately from a flip type grazing bifurcation then is it possible to show that there must be a homoclinic tangle in the invariant manifolds of the unstable solution created at the bifurcation? It may be possible to locate the invariant manifolds analytically, again due to the simple piecewise linear nature of the impact oscillator model (a similar idea is used in Hogan [1992]). The observation made above that a whole period doubling cascade appears to have been compressed to a point at a flip type grazing bifurcation could be examined in smooth models of impact oscillators. Does the period doubling cascade get compressed to a point as the severity of the impact is increased, and if so at what rate? Further interesting directions for further work may lie in investigating the bifurcations which can occur in other continuous, non-differentiable maps.

The simple experiment which is described in chapter 6 is not sensitive enough to show the detailed events shown in some experimental studies, such as chaotic solutions, or periodic solutions at exactly the predicted parameter settings. We were however able to detect the significant bifurcational events which occur in this physical one sided impact oscillator and show that the overall qualitative behaviour is as predicted by the COR model. This gives a further indication that the COR model, although simple, does capture the essential characteristics of true impacting systems. Although grazing bifurcations only occur in the idealised mathematical model, they approximate the true behaviour of impact oscillators undergoing low velocity impacts.

References and bibliography

Allgower, E.L. and Georg, K. *Numerical Continuation Methods*, Springer-Verlag, Berlin, 1990.

Arrowsmith, D.K. & Place, C.M. *An Introduction to Dynamical Systems*, Cambridge University Press, 1990.

Bayly, P.V. & Virgin, L.N. An experimental study into an impacting oscillator, *Preprint*, 1992.

Budd, C., Dux, F. & Cliffe, A. The effect of frequency and clearance on single degree of freedom impact oscillators, *Internal Report AM-93-02*, Bristol University, 1993.

Chillingworth, D. Vibro-Impact Systems : Singularity Structure, *Unpublished notes*.

Davis, R.O. Pounding of buildings modelled by an impact oscillator, *Earthquake Engineering and Structural Dynamics*, **Vol. 21**, 1992, pp.253-274.

Foale, S. & Bishop, S.R. Bifurcations in impact oscillators, *To appear in Nonlinear Dynamics*.

Foale, S. & Bishop, S.R. Dynamical complexities of forced impacting systems, *Philosophical Transactions of the Royal Society of London A*, **Vol. 338**, 1992, 547-556.

Foale, S. & Thompson, J.M.T. Geometrical concepts and computational techniques of nonlinear dynamics, *Computer Methods for Applications in Mechanical Engineering*, **Vol 89**, 1991, pp.381-394.

Goldsmith, W. *Impact*, Edward Arnold, London, 1960.

Golub, G.H. & Van Loan, C.F. *Matrix Computations*, Johns Hopkins University Press, 1989.

Guckenheimer, J. & Holmes, P.J. *Nonlinear oscillations, dynamical systems and bifurcations of vector fields*, Springer Verlag, New York, 1990.

Henon, M. On the numerical computation of Poincaré maps, *Physica D*, Vol. 5, 1982, pp.412-414.

Hindmarsh, M.B. & Jeffries, D.J. On the motions of the offset impact oscillator, *Journal of Physics A: Mathematical and General*, Vol. 17, 1984, pp.1791-1803.

Hogan, S.J. On the dynamics of rigid-block motion under harmonic forcing, *Proceedings of the Royal Society of London A*, Vol. 425, 1989, pp.441-476.

Hogan, S.J. The effect of damping on rigid block motion under harmonic forcing, *Proceedings of the Royal Society of London A*, Vol. 437, 1992a, pp.97-108.

Hogan, S.J. Heteroclinic bifurcations in damped rigid block motion, *Proceedings of the Royal Society of London A* , Vol. 439, 1992b, pp.155-162.

Holmes, P.J. The dynamics of repeated impacts with a sinusoidally vibrating table, *Journal of Sound and Vibration*, Vol. 84(2), 1982, pp.173-189.

Hsu, C.S. *Cell-to-cell mapping : a method of global analysis of nonlinear systems*, Springer-Verlag, New York.

Isomaki, H.M., Von Boehmm, J. and Raty, R. Devil's attractors and chaos of a driven impact oscillator, *Physics Letters*, Vol. 107A(8), pp.343-346.

Jing, H.S. & Young, M. Random response of a single degree of freedom vibro impact system with clearance, *Earthquake Engineering and Structural Dynamics*, Vol. 19, 1990, pp.789-798.

Jing, H.S. & Young, M. Impact interactions between two vibration systems under random excitation, *Earthquake Engineering and Structural Dynamics*, **Vol. 20**, 1991, 667-681.

Kahraman, A. and Singh, R. Nonlinear dynamics of a spur gear pair, *Journal of Sound and Vibration*, **Vol. 142(1)**, 1990, pp.49-75.

Karagiannis, K. & Pfeiffer, F. Theoretical & experimental investigations of gear rattling, *Nonlinear Dynamics*, **Vol. 2**, 1991, pp.367-387.

Kim, Y.B. & Noah, S.T. Stability and bifurcation analysis of oscillators with piecewise-linear characteristics: a general approach., *Journal of Applied Mechanics*, **Vol. 58**, 1991, pp.545-553.

Kleczka, M., Kreuzer, E. & Schiehlen, W. Local and global stability of a piecewise linear oscillator, *Philosophical Transactions of the Royal Society of London A*, **Vol. 338**, 1992, pp.533-546.

Knudsen, C., Feldberg, R. & True, H. Bifurcations and chaos in a model of a rolling railway wheelset, *Philosophical Transactions of the Royal Society of London A*, **Vol. 338**, 1992, pp. 455-469.

Lean, G.H. Subharmonic motions of moored ships subjected to wave action, *Transactions of the Royal Institute of Naval Architects*, **Vol. 113**, 1971, pp. 387-399

Liu, Z., Xie, H., Zhu, Z. and Lu. Q. The strange attractor of the lozi mapping, *International Journal of Bifurcation and Chaos*, **Vol. 2**, No. 4, 1992, pp.831-840.

Mahfouz, I.A. & Badrakhan, F. Chaotic behaviour of some piecewise-linear systems parts I & ii : systems with set-up spring or with unsymmetric elasticity, *Journal of Sound and Vibration*, **Vol. 143(2)**, 1990, 255-328.

Moon, F.C. & Shaw, S.W. Chaotic vibrations of a beam with nonlinear boundary conditions, *International Journal of Nonlinear Mechanics*, **Vol. 18**, No. 6, 1983, pp.465-477.

Moore, D.B. & Shaw, S.W. The experimental response of an impacting pendulum system, *International Journal of Nonlinear Mechanics*, **Vol. 25**, 1990, pp.1-16.

Natsiavas, S. Stability and bifurcation analysis for oscillators with motion limiting constraints, *Journal of Sound and Vibration*, **Vol. 141(1)**, 1990, pp.97-102.

Nelson, W.E., Benton, S.M. & Bernhard, S. Bumper pile design for mating platform and subsea drilling template, *Presented Offshore Technology Conference*, 1983, Houston.

Nguyen, D.T., Noah, S.T. & Kettleborough C.F. Impact behaviour of an oscillator with limiting stops (parts I and II), *Journal of Sound and Vibration*, **Vol. 109**, 1987, pp.293-325.

Nordmark, A.B. Non-periodic motion caused by grazing incidence in an impact oscillator, *Journal of Sound and Vibration*, **Vol. 145(2)**, 1991, pp. 279-297.

Nordmark, A.B. Grazing conditions and chaos in impacting systems, *Doctoral Thesis*, Royal Institute of Technology, Stockholm, 1992a.

Nordmark, A.B. Effects due to low velocity impact in oscillators, *International Journal of Bifurcation and Chaos*, Vol. 2, No. 3, 1992b, pp.597-606

Nusse, H.E. and Yorke, J.A. Border collision bifurcations including "period two to period three" for piecewise smooth systems, *Physica D*, **Vol. 57**, 1992, pp.39-57.

Paidousis, M.P. & Li, G.X. Cross-flow-induced chaotic vibrations of heat exchanger tubes impacting on loose supports, *Journal of Sound and Vibration*, **Vol. 152(2)**, 1992, pp.305-326.

Parker, T.S. & Chua, L.O. *Practical Numerical Algorithms for Chaotic Systems*, Springer-Verlag, New York, 1989.

Peterka, F. and Vacik, J. Transition to chaotic motion in mechanical systems with impacts, *Journal of Sound and Vibration*, Vol. 154(1), 1992, pp.95-115.

Pfeiffer, F & Kunert, A. Rattling models from deterministic to stochastic processes, *Nonlinear Dynamics*, Vol.1 , 1990, pp.63-74.

Press, W.H., Flannery, B.P., Teukolsky, S.A. & Vetterling, W.T. *Numerical Recipes in C : The Art of Scientific Computing*, Cambridge University Press, 1991.

Reithmeier, E. Periodic solutions of nonlinear dynamical systems with discontinuities, *Proceedings IUTAM Symposium Nonlinear Dynamics in Engineering Systems, Stuttgart 1989*, Springer-Verlag, Berlin, 1990.

Robinson, R.W. & Ramzan, F.A. Prediction of jacket to template docking forces during installation, *Preprint*, 1989.

Sharif-Bakhtiar, M. & Shaw, S.W. The dynamic response of a centrifugal pendulum vibration absorber with motion limiting stops, *Journal of Sound and Vibration*, Vol. 126(2), 1988, pp.221-235.

Shaw, J. & Shaw, S.W. The onset of chaos in a two-degree of freedom impacting system, *Journal of Applied Mechanics*, Vol. 56, 1989, pp.168-174.

Shaw, S.W. Dynamics of harmonically excited systems having rigid amplitude constraints, part 1 - subharmonic motions and local bifurcations, *Journal of Applied Mechanics*, Vol. 52, 1985a, pp.453-458

Shaw, S.W. Dynamics of harmonically excited systems having rigid amplitude constraints, part 2 - chaotic motions and global bifurcations, *Journal of Applied Mechanics*, Vol.52, 1985b, pp.459-464.

Shaw, S.W. Forced vibrations of a beam with one sided amplitude constraint - theory and experiment, *Journal of Sound and Vibration*, Vol. 99, 1985c, pp.199-212.

Shaw, S.W. & Holmes, P.J. Periodically forced linear oscillator with impacts : chaos and long period motions, *Physical Review Letters*, Vol. 51(8), 1983a, pp.623-626.

Shaw, S.W. & Holmes, P.J. A periodically forced impact oscillator with large dissipation, *Journal of Applied Mechanics*, Vol. 50, 1983b, pp. 849-857

Shaw, S.W. & Holmes, P.J. A periodically forced piecewise linear oscillator, *Journal of Sound and Vibration*, Vol. 90, No. 1, 1983c, pp.122-155.

Shaw, S.W. & Rand, R.H. The transition to chaos in a simple mechanical system, *International Journal of Nonlinear Mechanics*, Vol. 24(1), 1989, pp.41-56.

Stahl, B., Nelson, W.E. & Baur, M.P. Motion monitoring of a moored floating platform during installation over a subsea template, *Journal of Petroleum Technology*, 1983, pp.1239-1248.

Stennson, A. & Nordmark, A.B. Chaotic vibrations of a spring/mass system with a unilateral displacement limitation - theory and experiments, *Preprint*, 1992, Lulea University of Technology, Sweden.

Stennson, A., Asplund, C. & Karlsson, L. The nonlinear behaviour of a MacPherson strut wheel suspension, *Preprint*, 1992.

Sterndorff, M.J., Waegter, J. & Eilersen, C. Design of fixed offshore platforms to dynamic ship impact loads, *Journal of Offshore Mechanics and Arctic Engineering*, Vol.114, 1992, pp.146-153.

Thompson, J.M.T. Complex dynamics of compliant offshore structures, *Proceedings of the Royal Society of London*, Vol. 387, No. 1793, 1983, pp.407-427.

Thompson, J.M.T. & Elvey, J.S.N. Elimination of subharmonic resonances of compliant marine structures, *International Journal of Mechanical Sciences*, **Vol. 26**, 1984, pp.419-425.

Thompson, J.M.T. & Ghaffari, R. Chaos after period doubling bifurcations in the resonance of an impact oscillator, *Physics Letters A*, **Vol. 91**, 1982, pp.5-8.

Thompson, J.M.T. & Ghaffari, R. Chaotic dynamics of an impact oscillator, *Physical Review*, **Vol. 27A**, 1983, pp.1741-1743.

Thompson, J.M.T. & Stewart, H.B. *Nonlinear Dynamics and Chaos*, Wiley, London, 1986.

Thompson, J.M.T., Bokaian, A.R. & Ghaffari, R. Subharmonic resonances and chaotic motions of a bilinear oscillator, *Journal of Applied Mathematics*, **Vol. 31**, 1983, pp.207-234

Thompson, J.M.T., Bokaian, A.R. & Ghaffari, R. Subharmonic and chaotic motions of compliant offshore structures and articulated mooring towers, *Journal of Energy Resources Technology*, **Vol. 106**, 1984, pp. 191-198.

Tso, W.K. & Wong, C.M. Steady state rocking response of rigid blocks part 1 : analysis, *Earthquake Engineering and Structural Dynamics*, **Vol. 18**, 1989, pp.89-106.

Tung, P.C. & Shaw, S.W. The dynamics of an impact print hammer, *Journal of Vibration, Acoustics, Stress and Reliability in Design*, **Vol. 110**, 1988a, pp.193-200.

Tung, P.C. & Shaw, S.W. A method for the improvement of impact printer performance, *Journal of Vibration, Acoustics, Stress and Reliability in Design*, **Vol. 110**, 1988b, pp.528-532.

Whiston, G.S. Impacting under harmonic excitation, *Journal of Sound and Vibration*, **Vol. 67(2)**, 1979, pp.179-186

Whiston, G.S. The vibro-impact response of a harmonically excited and preloaded one-dimensional linear oscillator, *Journal of Sound and Vibration*, **Vol. 115**, 1987a, pp.303-319.

Whiston, G.S. Global dynamics of a vibro-impacting linear oscillator, *Journal of Sound and Vibration*, **Vol. 118**, 1987b, pp.495-429.

Whiston, G.S. Singularities in vibro-impact dynamics, *Journal of Sound and Vibration*, **Vol. 152(3)**, 1992, 427-460.

Wood, L.A. & Byrne, K.P. Analysis of a random repeated impact process, *Journal of Sound and Vibration*, **Vol. 78**, 1981, pp.329-345.

Block, L.S. and Coppel, W.A., Dynamics in One Dimension. *Lecture Notes in Mathematics*, **1513**, Springer-Verlag , Berlin, 1991.